Design of a Variable Pitch, Energy-Harvesting Propeller for In-Flight Power Recuperation on Electric Aircraft

J.M.F. van Neerven

Technische Universiteit Delft

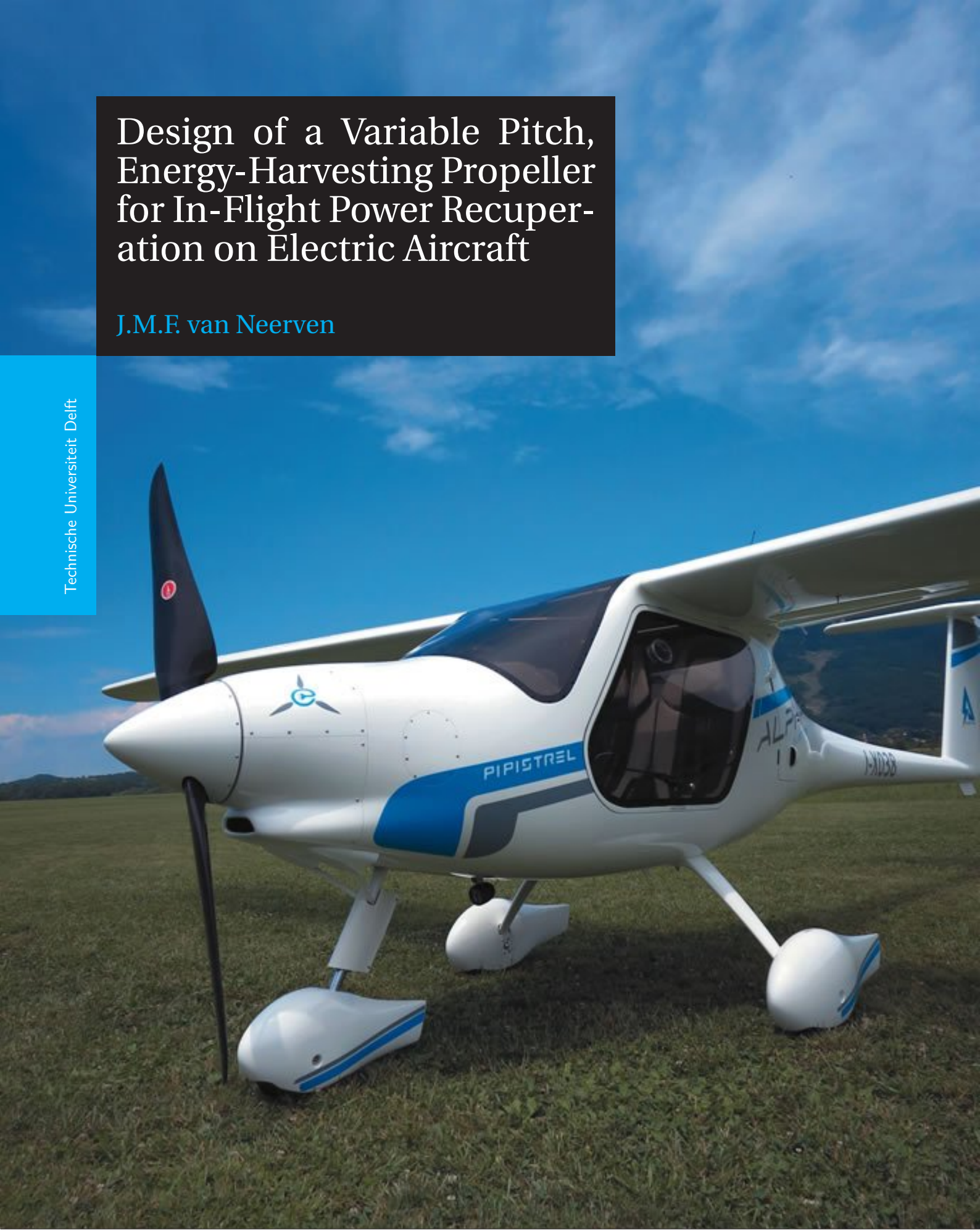

TU Delft Delft University of Technology

Challenge the future

Design of a Variable Pitch, Energy-Harvesting Propeller for In-Flight Power Recuperation on Electric Aircraft

by

J.M.F. van Neerven

in partial fulfillment of the requirements for the degree of

Master of Science
in Aerospace Engineering

at Delft University of Technology,
to be defended publicly on Monday November 30, 2020 at 14:00 PM.

Student nr.:	4231899	
Supervisor:	Dr. ir. T. Sinnige	
Thesis committee:	Dr. ir. T. Sinnige,	TU Delft
	Prof. dr. ir. G. Eitelberg,	TU Delft
	Prof. dr. ir. Simao Ferreira,	TU Delft

An electronic version of this thesis is available at http://repository.tudelft.nl/.

TU Delft Delft University of Technology

PREFACE

This research project about energy recuperation technology on electric aircraft concludes my Master of Science in Aerospace Engineering at Delft University of Technology. Energy harvesting on electric aircraft is a relatively new research area which is under rapid development, with the main aim to improve the energy performance of these aircraft. This report presents the findings regarding the influence a constant/variable pitch and/or RPM propeller on an electric aircraft on the overall energy consumption over a complete mission.

I would like to thank several people who contributed to this achievement. First of all, I would like to thank Tomas Sinnige and Leo Veldhuis, who supervised me during the project, for providing excellent feedback and being very attentive and supportive at all times. Furthermore, I would like to thank all the basement students in the HSL for always ensuring a motivational and social study environment. I have developed some great friendships with in particular Lucas, Maria, Ventsislav and Pedro who always studied there as well. They have always been very supportive and a great time is always guaranteed with them. I would also like to thank all my other friends who made my time at TU Delft enjoyable for their company and good times. Lastly, I would like to thank my parents, my sister and the rest of my family for always showing great care and support towards me.

J.M.F. van Neerven
Delft, November 2020

ABSTRACT

In the field of electric aviation, a promising method for reducing energy consumption is the addition of energy recuperation during the descent phase, where the propeller operates in windmilling mode, converting the gravitational and kinetic energy of the aircraft into useful energy that can be used for an extension of the current mission range or for the subsequent mission. The state of the art propellers designed for energy harvesting missions operate at a constant pitch setting. The main objective of this thesis is to investigate to what extent the energy performance of the aircraft can be improved by applying variable pitch and RPM to the propeller operation during the mission with respect to the application of a ground-adjustable pitch propeller.

A propeller analysis model is selected that is based on an accurate representation of the Goldstein circulation function, under the assumption of helicoidal vortex sheet formation for evaluating the bound circulation on the propeller. Iterating the theoretical results of this analysis model with experimental results for the blade loading as generated using the aerodynamic analysis program XFOIL, the blade loading of a given propeller geometry and operational conditions is obtained.

The propeller analysis model is subsequently used by a propeller optimisation algorithm in order to optimise the propeller geometry and operational conditions for minimum energy consumption during a mission including energy harvesting. The differential evolution genetic algorithm is used as the optimisation algorithm, since it turns out to be the most suitable one for application to the propeller design space under consideration. The selection of this algorithm is mainly based on its simplicity, good convergence characteristics and robustness as compared to other genetic algorithms.

After a careful formulation of the optimisation problem including the objective function, constraints, design variables and their upper and lower bounds, optimisations are performed to three cases with respect to the variation of blade pitch and RPM; constant pitch, variable RPM (CPVR), variable pitch, constant RPM (VPCR) and variable pitch, variable RPM (VPVR). Both single-point and multi-point optimisations are performed for each case. The former implies that the propeller is optimised for a single point in the flight mission and subsequently it is operationally optimised for minimum energy consumption over the whole mission. For the single-point optimisations, it turns out that for the VPVR case the overall energy consumption of the propellers optimised for climb, cruise and descent are all lowest as compared to the CPVR and VPCR cases. During the multi-point optimisation, the propeller is optimised for minimum energy consumption over the whole mission. Compared to the other cases, it turns out that the percentage of energy that is saved in the VPVR case is a function of the cruise distance. The largest percentage of total mission energy saved using the VPVR propeller with respect to the CPVR propeller is about 4.1% for a cruise distance of 5 km when using two blades and about 3.0% for three blades. This percentage reduces to approximately 0.7%, both for two and three blades, for a mission where the cruise distance is d_{cr} = 200 km. Compared to the VPCR case, the VPVR propeller is capable of saving a larger percentage of the total energy than compared to the CPVR case for larger cruise distances, and a smaller percentage for shorter cruise distances. The percentage of energy saved during the climb phase for the VPVR propeller with respect to the CPVR propeller decreases with the cruise distance and becomes negative for cruise distances larger than approximately d_{cr} = 50 km. On the other hand, the climb energy saved using the VPVR propeller with respect to the VPCR propeller increases with the cruise distance and is mostly positive for all cruise distances. Regarding the fraction of energy recuperated, the VPVR propeller is capable of recuperating more energy at all cruise distances as compared to the CPVR and VPCR propellers. The rate of descent is also higher for the VPVR propeller as compared to the CPVR and VPCR propellers.

Initially, only the NACA 4415 airfoil is considered for all the optimisations in this project as a result of its relatively good compromise between propulsive and regenerative performance. It therefore becomes interesting to study the effects of airfoil camber and thickness as well in order to investigate the effect the variation of airfoil geometry has on the overall energy performance of the aircraft over the whole mission. It turns out that the airfoil selection based on minimum energy consumption depends on the cruise distance. For small cruise distances, the symmetrical NACA 0015 airfoil performs best, while for long cruise distances, the NACA 2415 airfoil is the one that results in minimum energy consumption. Considering the effect of thickness variation with respect to the NACA 4415 airfoil, the application of the NACA 4412 airfoil along the blades results

in increased energy consumption as compared to the NACA 4415 airfoil in all the mission cases considered. This could be a result of a significant section efficiency decrease when a thin cambered airfoil is exposed at negative angles of attack during the descent phase.

CONTENTS

List of Figures

List of Tables

NOMENCLATURE

GREEK SYMBOLS

Symbol	Definition	Unit
α	Angle of attack	rad
β	Blade angle	rad
γ	Flight path angle	rad
Γ	Circulation	m^2/s
η_p	Propulsive propeller efficiency	-
η_{cl}	Propeller efficiency in climb	-
η_{cr}	Propeller efficiency in cruise	-
η_w	Propeller efficiency in descent	-
μ	Dynamic viscosity of air at 20 deg $^\circ C$	kg/ms
μ	Mean of values to calculate the standard deviation	-
Ω	Propeller rotational velocity	rad/s
Ω_{cl}	Propeller rotational velocity in climb	rad/s
Ω_{cr}	Propeller rotational velocity in cruise	rad/s
Ω_w	Propeller rotational velocity in descent	rad/s
κ	Airfoil technology factor	-
λ	Wing taper ratio	-
λ	Advance ratio	-
λ_1	Trailing vortex advance ratio	-
λ_2	Trailing vortex advance ratio depending on axial wake displacement velocity	-
ϕ	Inflow angle	rad
ρ	Air density	kg/m^3
σ	Solidity factor	-
σ	Speed ratio	-
σ	Rate of energy consumption per unit of thrust	J/Ns
σ	Standard deviation	-

ROMAN SYMBOLS

Symbol	Description	Unit
A	Wing aspect ratio	-
a	Asymptotic radius of the source body	m
a	Speed of sound	m/s
B	Number of propeller blades	-
b	Wingspan	m
b	Distance of the plane of the propeller ahead of the nose of the nacelle	m
CR	Crossover constant for differential evolution optimisation	-
C_l	Lift coefficient	-
$C_{l,th}$	Theoretical lift coefficient	-
$C_{l,exp}$	Experimental lift coefficient	-
C_{l_p}	Propulsive lift coefficient	-
C_{l_w}	Regenerative lift coefficient	-
C_d	Drag coefficient	-
C_{D_0}	Zero-lift drag coefficient	-
c	Propeller blade chord	m
c_r	Wing root chord	m
D	Drag	N
D_{ac}	Aircraft drag	N
D_p	Propeller drag	N
D	Propeller diameter	m
d	Flight distance	m
d_{cl}	Climb flight distance	m
d_{cr}	Cruise flight distance	m
d_F	Fuselage width	m
E	Energy	J
E_{cl}	Propeller climb energy	J
E_{cr}	Propeller cruise energy	J
E_w	Propeller descent energy	J
E_{sh}	Shaft energy	J
E_{tot}	Total propeller energy	J
E_{rec}	Fraction of energy recuperated	-
e	Oswald factor	-
F	Mutation constant for differential evolution optimisation	-
F	Vortex sheet tip correction factor	-
F_{res}	Resultant aerodynamic force	N
G	Generation of vectors within the differential evolution optimisation	-
$G(x, \lambda_2, B)$	Goldstein circulation function	-
h	Ratio between the linear vortex sheet pitch and the number of blades	m
h_{cr}	Cruise altitude	m
J	Propeller advance ratio	-
K_T	Thrust coefficient	-
K_Q	Torque coefficient	-
K_P	Power coefficient	-
L	Lift	N
M	Mach number	-
M_{DD}	Drag divergence Mach number	-
N	Number of blade elements	-
N	Number of runs to calculate the standard deviation	-
NP	Population size for differential evolution optimisation	-
n	Revolutions per second	rev/s

P	Propeller power	W
P	Linear vortex sheet pitch	m
P_{sh}	Shaft power	W
P_{max}	Maximum motor power	W
P_w	Regenerative propeller power	W
R	Propeller radius	m
R_1	Trailing vortex radius	m
Re	Reynolds number	-
r	General propeller radial coordinate	m
r_h	Hub radius	m
S	Wing surface area	m^2
T	Propeller thrust	N
T_{cl}	Propeller climb thrust	N
T_{cr}	Propeller cruise thrust	N
T_w	Propeller descent thrust	N
t	Flight time	s
t	Airfoil thickness	m
t_w	Time to descent	s
Q	Propeller torque	N
$\vec{u}_i$	Trial vector	-
u_θ	Tangential induced velocity	m/s
$\bar{u}_\theta$	Normilised tangential induced velocity	-
u_z	Axial induced velocity	m/s
$\bar{u}_z$	Normilised axial induced velocity	-
u_{zN}	Axial velocity contribution of the nacelle	m/s
$\bar{u}_{zN}$	Normilised axial velocity contribution of the nacelle	-
U_0	Resultant velocity at a blade element	m/s
V	Aircraft flight velocity	m/s
V_{cl}	Aircraft climb velocity	m/s
V_{cr}	Aircraft cruise velocity	m/s
V_w	Aircraft descent velocity	m/s
$\vec{v}_i$	Mutation vector	-
w	Axial wake displacement velocity	-
$\bar{w}$	Normilised axial wake displacement velocity	-
W	Aircraft weight	N
x	Normilised radial coordinate at the propeller	-
x_h	Normilised hub radius	-
x_i	Design variable from design vector	-
x_1	Normilised radial coordinate on the trailing vortex system	-
$\vec{x}$	Design vector	-
$\vec{x}_{opt}$	Optimised design vector	-

SUBSCRIPTS

Subscript	Description
0	At the propeller plane
0	Without energy recuperation
1	At the trailing vortex system
cl	Climb condition
cr	Cruise condition
h	At the hub
p	Propulsive mode
req	Required
sh	Shaft
tot	Total
w	Regenerative mode

ACRONYMS

Abbreviation	Description
RC	Rate of climb
ROD	Rate of descent
RPM	Revolutions per minute
CPVR	Constant pitch, variable RPM
VPCR	Variable pitch, constant RPM
VPVR	Variable pitch, variable RPM

1

INTRODUCTION

Depletion of fossil fuels imposes a challenge for contemporary researchers in encountering alternative energy sources. Nowadays, aeronautical research is primarily focussing on achieving a more sustainable generation of aircraft in the future, whereby the rapid development of battery and (hybrid) electric engine technology are promising; it is believed that electric and hybrid electric aircraft have great future potential. A promising concept within electric aviation technology is called regenerative electric flight, whereby energy is recuperated by the use of one or more propellers in an energy-extracting, windmilling mode. The gravitational potential energy and kinetic energy during the descent phase is used and converted, enabling the regeneration of the energy stored in the battery of the electric engine. The use of propellers as airborne wind turbines on the aircraft could therefore be a useful added feature for achieving a reduction in the aircraft energy consumption, motivating several researchers to introduce the concept for future applications [3]. Although currently the focus lies mostly on sustainable engine technology development and novel propulsive propeller design concepts, designing propellers capable of operating both in propulsive and regenerative energy extraction modes is a relatively new research area.

In section 1.1, the historical development and challenges within regenerative electric flight are discussed. The previously performed research in the area of propeller aerodynamics and design is discussed in section 1.2, after which an overview of the state of the art within regenerative electric flight is presented in section 1.3. The common practice of aircraft propeller operation is the subject of section 1.4. The objective of this research project is introduced in section 1.5. The scope and outline of the project are discussed in sections 1.6 and 1.7 respectively.

1.1. HISTORICAL DEVELOPMENT AND CHALLENGES WITHIN REGENERATIVE ELECTRIC FLIGHT

In this section, the historical development of regenerative electric flight and the main challenges within the research area are discussed.

The first person to mention the case of considering a windmilling propeller on an aircraft was the British aerodynamicist Hermann Glauert [6]. He analysed it, believing in the prospect of the windmilling propeller having potential for future research and application. At the time, however, no practical application of the concept was offered by Glauert [3]. Subsequently, the American engineer Paul MacCready introduced the regeneration of energy in electric flight [7], based on Glauert's findings, whereby he discussed an application of the concept [3]. The feasibility of MacCready's concept was verified by J. Philip Barnes [2]. Barnes extended his research by investigating in more detail the factors that play a role in the integration of an electric engine with a dual-role propeller that is desired to operate as a power generating as well as a power extraction source during the flight mission. MacCready could be seen as the pioneer in the field of regenerative electric flight, since besides the potential of the concept, he took the initiative to discuss examples of its practical applications [7]. It is claimed that the technology enables a reduction in energy consumption as well as an extension of the options and flexibility the pilot obtains with the 'extra energy' that would not be there without in-flight energy recuperation. The flight time can be increased if necessary, or storage of energy for the subsequent flight becomes possible. Also, it is known that electric propulsion is relatively clean and quiet with respect to piston engines [7]. Comparing the regenerative propeller technology potential to current technology de-

velopments, interesting conclusions can be drawn as well. For example, despite the rapid advances in solar cell technologies, these provide relatively low power and their performance highly depend on weather conditions. Furthermore, extra weight is added to the aircraft [7]. What's more, regenerative braking technology is already widely being developed and applied thanks to the electric automotive industry and its adaptations to electric aviation are expected to take place, as nowadays the technology is generally well advanced and still improving considerably fast [7].

The main mechanism driving regenerative flight technology is an innovative propeller design that can accomplish a dual function of delivering sufficient power in the most energy-demanding climbing flight phase, while simultaneously regenerating as much energy as possible by windmilling during the descent flight phase. There are several considerations and constraints for the designer to keep in mind when designing propellers for energy harvesting. First of all, as might sound obvious, a propeller design that is optimised for an efficient propulsive purpose will not achieve optimum performance in the windmilling condition and vice versa. Therefore, it is clear that the main challenge for this design case is that a compromise needs to be achieved between propulsive and regenerative propeller performance. However, it is also suggested by MacCready that two separate propellers could be used on the aircraft, one for power delivery and one for energy regeneration, and fold back the one not needed at the particular moment [7]. Alternatively, only one four-bladed propeller with two blades optimised for energy regeneration and two for power delivery could be used. In this case, the propeller would then be operated using only the pair of two blades necessary at the moment and fold back the other two. Although these concepts sound elegant, the folding mechanisms would be complex and expensive and the purpose of this project is to attempt the development of a propeller design by finding the best possible compromise between the efficiencies in the climb, cruise and windmilling operating modes for minimum total energy consumption over the entire mission.

As is clear from the discussion above, the regenerative system designer deals with a large amount of variables and compromises to be decided upon. Furthermore, battery technology is constantly being improved and for their selection, one has to consider that each type of battery system has its advantages and disadvantages in terms of energy, weight, cost and lifetime for example. The battery, motor and propeller need to work together as a power delivery and extraction source on the aircraft. Also, it is important to consider the fact that the motor, generator, windmill and propeller each have their own efficiencies. It is predicted that the overall efficiency of a reasonable regenerative system design can be in the order of 33 - 50% [7]. This means that for every measure in altitude descended and used for energy regeneration, 33 - 50% of that distance can be climbed later using the regenerated energy. This is considered to be a good achievement, however, a challenging one to realise. The energy generated can also be used for different purposes, for example in aircraft systems for heating or boundary layer control [7].

1.2. PREVIOUS RESEARCH ON PROPELLER AERODYNAMICS AND DESIGN

The research field of propeller aerodynamics and design is extremely broad and there exist many approaches towards the analysis of the complex flow field in the proximity of an operational propeller. A wide variety of simplifications and assumptions are often applied in aerodynamic models attempting to predict the propeller performance given a number of input parameters. This leaves the propeller aerodynamic designer with a large amount of possible approaches in the phase of selecting an appropriate aerodynamic model or CFD software for solving a particular problem. Each proposed existing model contains different assumptions and approximations, some of which could possibly lead to an unacceptable prediction of the propeller performance. This implies that the designer should always maintain a critical approach towards designing for and predicting sufficiently accurate propeller performance characteristics.

There are a number of influential researchers that took the effort in attempting to describe the complex aerodynamics of propellers, developing knowledge by building upon each others ideas and theories [4]. Back in the 19th century, Rankine [8] and Froude [9] initialised the understanding of marine propellers by developing a momentum theory of a propeller operating in water. Obviously, the fundamental principles of their theory will also apply to the operation of a propeller in air. Wilbur and Orville Wright [10] were the first two researchers that combined blade element theory and momentum theory. The lifting line theory developed by Prandtl led to a more profound insight and interpretation of propeller aerodynamics, while Betz investigated loading characteristics on lightly loaded propellers for minimum energy loss [11]. On the other hand, Goldstein presented the characteristics of the distribution of circulation over propeller blades, this work also only being limited to lightly loaded propellers [12]. Theodorsen proceeded the development of propeller aerodynamics by introducing a method of determining the ideal load distribution along propeller blades without

incorporating the previous assumption of lightly loaded propellers [13]. His work is of major importance and well appreciated in the research field of propeller aerodynamics, however, its content needed some further development at some points [4]. The contribution of Wald [4] combines the several approaches towards propeller aerodynamics that used to be incomplete in previous studies at some points, and attempts to find the missing pieces with the aim to achieve a solid and consistent understanding of propeller aerodynamics.

1.3. STATE OF THE ART OF REGENERATIVE ELECTRIC FLIGHT TECHNOLOGY

In this section, the state of the art research on the design of airborne energy-harvesting propellers is discussed. The currently used multidisciplinary research approach is outlined after which the basic powertrain characteristics of a state of the art electric aircraft are given.

1.3.1. MULTIDISCIPLINARY RESEARCH APPROACH

The relatively recent study performed by the company Pipistrel Vertical Solutions d.o.o. discusses an approach for designing a propeller for in-flight energy recuperation [1]. The propeller design optimisation approach used by Pipistrel comprises three main disciplines that are optimised simultaneously. Distinction is made between aerodynamic, electric and strategic approaches in the propeller design process. This ensures that the propulsion system is optimised as a whole. The aerodynamic approach focusses on the optimisation of the blade geometry using computer programs for aerodynamic analysis and design, and verifying the results with more advanced CFD simulations. On the other hand, the electrical approach focusses on the design and optimisation of the components of the powertrain with the main aim of maximising the energy recuperation. Finally, the strategic part of the research approach includes optimisation on mission level, designing the mission profile with the aim of optimising for energy consumption and recuperation.

In this thesis research project, the focus lies on the aerodynamic design and optimisation of a dual-role propeller, complying with given thrust and power requirements and maximising the energy recuperation during descent. However, some knowledge about the working principles of the electric engine and a typical mission profile of the type of aircraft under consideration are useful for determining the input parameters for the aerodynamic optimisation of the propeller. In [14], [15] and [16], more details are given about the essentials of the electric powertrain and flight mission profile characteristics.

Regenerative electric flight technology is generally believed to be promising for future application, as positive outcomes are presented in most cases. As mentioned before, Pipistrel Vertical Solutions d.o.o. is an example of a company that has actually developed an airborne energy-harvesting propeller and applied it to their existing electric aircraft. In this section, their results are presented briefly in order to give an idea of the current state of the art technology of regenerative flight.

The performance of in total three propeller configurations designed by Pipistrel Vertical Solutions d.o.o. were compared to each other and validated by performing various flight tests [1]. In figure 1.1, the three propeller designs are illustrated. The geometry of the left one was optimised for operating in combination with a piston engine, while the middle and the right ones were designed for the electric version of the aircraft. The middle one was optimised for climb and cruise, while the right one was optimised for climb and energy-recuperation. It is clear from figure 1.1 that the geometries of the three propellers are quite different, as they are designed for different operation purposes [1].

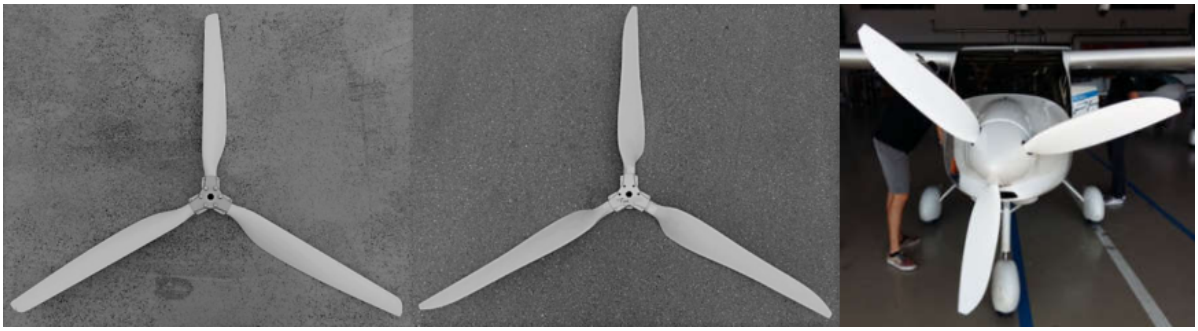

Figure 1.1: Pipistrel's propeller design concepts [1]

The most important outcome from the research performed by the company was that the total energy consumption of the regenerative propeller reduced by 19% with respect to the piston engine propeller over

the entire flight mission. Furthermore, the performance of the left and middle propellers is comparable in the climb and recuperation flight phases. Finally, it was concluded that for the climbing flight phase, the energy consumption of the regenerative propeller decreases with 6% with respect to the piston engine propeller. This is interesting to note since generally, propellers designed to operate in propulsive mode would be expected to be more efficient in propulsive flight phases than propellers designed to achieve a compromise between both propulsive and regenerative operating modes.

1.3.2. ENERGY HARVESTING POWERTRAIN ARCHITECTURE

In figure 1.2, the main powertrain components of an aircraft designed for regenerative flight are illustrated. It shows the main driving components and their interconnections that allow, besides propulsion, in-flight energy recuperation [2].

The ESU unit stands for energy storage unit, which could be a battery for example to be used for energy storage. Energy is exchanged between the ESU and the electrical-power conditioner (EPC) used to control speed with an electric motor-generator (EMG). The shaft power generated is exchanged with the energy-harvesting propeller by the electric motor-generator using a speed-torque converter between the energy-harvesting propeller and the electric motor-generator, which ensures the required transmission for optimal functioning of the system. The energy-harvesting propeller in turn exchanges energy with the freestream airflow. The latter occurs either in the energy consuming (propelling) or energy extraction (windmilling) mode. The transition from propulsive to energy-harvesting operating mode could be achieved by changing the blade pitch angle and/or the RPM. In case of a constant-speed propeller, this would mean that the constant-speed control unit automatically adjusts the blade pitch angle in order to achieve the desired RPM.

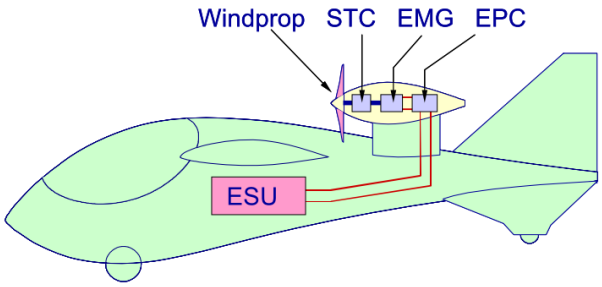

Figure 1.2: Main components of a regenerative powertrain [2]

In figure 1.3, the architecture of the powertrain of the Pipistrel Alpha Electro aircraft is illustrated [2]. Using this configuration design, the torque and RPM can be regulated for power management optimisation. Therefore, since the working principle of the constant-speed unit in the considered case of a constant-speed propeller is similar, this powertrain design is considered suitable for operation in combination with a variable-pitch propeller as well. As shown in figure 1.3, the powertrain architecture contains a battery for energy storage and a power control unit (PCU) that controls the energy transmission between the battery and the electric motor and the main computer. The latter is connected to the cockpit instruments and ensures communication of data with the pilot. Also, in cooperation with the PCU, no action is required by the pilot between the energy consumption and regeneration flight phases.

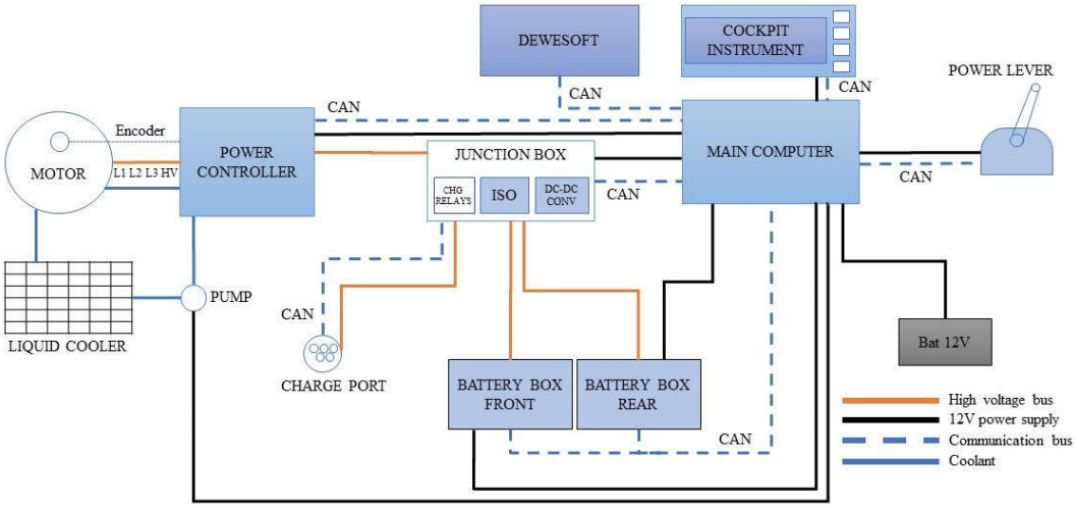

Figure 1.3: Pipistrel's alpha electro powertrain architecture [2]

1.4. AIRCRAFT PROPELLER OPERATION

As will be mentioned later, a gap in the state of the art of regenerative electric flight technology lies in exploring the possibilities of recuperating energy on electric aircraft using a variable pitch propeller, which can also operate as a constant-speed propeller. In this section, the operational characteristics of three types of propeller will be treated based on the manner in which blade pitch and RPM are used throughout the mission.

1.4.1. CLASSIFICATION OF PROPELLER TYPES BASED ON THE USE OF BLADE PITCH AND RPM

Based on how the propeller pitch and RPM vary during flight, aircraft propellers can be classified into three main types. These are the constant pitch propeller, variable pitch propeller and constant-speed propeller. Pipistrel's Alpha Electro aircraft already demonstrated good energy recuperating performance using a ground-adjustable, constant pitch propeller, which can be installed to a selected pitch angle when the aircraft is on the ground, after which that angle remains fixed for the entire flight mission [1]. However, many modern propeller aircraft nowadays make use of variable pitch propellers, since these are designed with the aim of operating at maximum efficiency when variations in engine power and/or airspeed occur during flight, as described in [17]. The RPM generally also varies during the flight mission for variable pitch propellers. Constant-speed propellers are also variable pitch propellers, however, they operate by adjusting the pitch angle of the blades in order to keep them operating at the most efficient angle of attack and at a desired constant RPM. Fixed pitch propellers, on the other hand, do not have this capability and their power output can only be controlled by controlling the throttle and thereby varying only the RPM. A variable pitch propeller converts the engine power more efficiently into thrust with respect to a fixed-pitch propeller, since for a variable pitch propeller it is possible to select the most efficient blade pitch setting at any given flight velocity, while a constant pitch propeller attains only a single blade pitch setting over the entire flight mission. It must be stated though, that despite the advantage of the varying pitch capability, variable pitch propellers are generally heavier with respect to fixed-pitch propellers due to the added complexity of the required pitching mechanisms. However, the focus of this thesis research project lies only on aerodynamic regenerative propeller design and the implications of these weight and complexity considerations on aircraft level are outside the scope of this research project. Instead, the latter would be interesting to consider during follow-up aircraft design studies.

This project aims to compare the mission energy consumption, including energy harvesting, of the three propeller types discussed above. The remainder of this section provides some insight into the common operation practice of these propeller types throughout the flight mission. This includes the selection of throttle setting for power supply, RPM setting and the required variation of the pitch angle for the different flight phases. Besides the throttle control on fixed pitch propeller aircraft, variable pitch propeller aircraft also contain a prop lever that can be used to set the desired RPM. Obtaining some insight into how the power supply, RPM and pitch angle vary in magnitude for take-off, climb, cruise, descent and landing with respect to each other is an important initial step in the design process of the constant speed energy-harvesting propeller, since an understanding of the relative operational characteristics of the energy-harvesting propeller for all

flight phases is gained. The challenge lies in using these properties of variable pitch propellers and apply them to the optimisation towards an efficient dual-role propulsive and energy-harvesting propeller.

The selection of throttle setting, desired engine RPM and the constant-speed unit that is designed to adjust the pitch angle of the propeller to provide the desired RPM, together determine the operational state of the constant-speed propeller at any moment. For constant-speed propellers, the governor in the constant-speed control unit constantly senses the current RPM of the propeller and adjusts the blade pitch angle that can control the RPM by controlling the loading on the blade. For example, if the RPM is too high, the control system increases the loading by increasing the blade pitch for the blades to operate at a higher angle of attack, which lowers the RPM back down. This occurs since increased blade loading implies an increased amount of drag and therefore the blades experience an increased rotational resistance, lowering the RPM to its desired value. In this way, the pilot can set the desired throttle setting and RPM value for any given point in flight and the control system uses the provided power from the throttle setting and the airspeed of the aircraft as inputs to maintain the blades at their optimum angle of attack by adjusting their pitch angle.

At take-off condition, maximum power, maximum RPM and a fine pitch angle are desired. Since the airspeed is initially zero and the optimum blade angle of attack is typically low, a fine pitch is required to ensure efficient blade operation and good alignment of the total resultant force produced by the blades with the direction of take-off. When the aircraft begins to move forwards at take-off, the increasing airspeed vector would decrease the angle of attack and the loading of the blades. In order to prevent the RPM from increasing and the angle of attack of the blades to fall below its optimum value, the constant speed unit therefore increases the pitch angle of the blades in the case of a constant-speed propeller. As soon as the aircraft is established in its climb, the engine power is reduced, the blade angle is increased to maintain the optimum angle of attack and the climb is continued to the chosen cruise altitude. During the regenerative descent, the RPM is lower [3] and the blade pitch angle is adjusted such that an optimum L/D, resulting from a weighted compromise between the climb and descent phases, is achieved.

As a regenerative flight mission is under consideration, the energy-harvesting propeller will operate under a windmilling condition during the descent of the aircraft, attempting to recuperate as much energy as possible. For windmilling, the thrust and power become negative. The energy-harvesting propeller therefore effectively generates additional drag and the torque keeps the propeller rotating by the incoming wind from the forward motion of the aircraft. While the RPM is initially set to a relatively high value during climb and cruise, the constant-speed unit will make sure that the pitch angle is reduced so that the requested RPM during the descent can be maintained.

1.4.2. POSSIBLE OPERATIONAL REGIMES OF A PROPELLER BLADE SECTION

This section discusses the basic aerodynamic working principles of a dual-role rotor that acts both as a propeller and a wind turbine on an aircraft. The effects of the wake-induced velocities are neglected for the moment. In figure 1.4, the velocity diagrams representing the three possible modes of local rotor blade operation are shown for a symmetrical blade section as a propeller, pinwheel and turbine. As suggested in [3] as a rule of thumb in finding an acceptable compromise between propeller and wind turbine performance of a rotor, symmetrical blade sections are generally recommended to be used in order to prevent a cambered section to operate at negative angles of attack in the wind turbine mode, since this would be very inefficient. However, for missions with relatively long cruise distances, likely the propulsive mode would mostly be beneficial to optimise for by using positively cambered airfoils. The use of symmetrical sections at all radial positions will result in a decrease in rotor efficiency of about 2%, while increasing the range and/or endurance of the aircraft by about 10% [3]. However, as it will later be clear from the research proposal of this project, the design of an energy-harvesting propeller with the possibility of attaining variable pitch angles during flight will be considered, instead of a propeller with a ground-adjustable constant pitch angle. This change in operational conditions regarding the blade pitch angle motivates the investigation of the influence of the use of cambered sections as well for the case of a variable pitch energy-harvesting propeller, leading to a possible improvement in overall propeller performance. After all, the overall propeller performance does not only depend on the selection of airfoils used along the blade span, but also on the operational conditions, the relative duration of the flight mission phases, the remaining rotor geometry parameters and the flow conditions.

Considering a simple aerodynamic approximation, there are three parameters that determine the local operational mode of a rotor blade section by their relative magnitudes. These are the freestream velocity V, the local rotor rotational velocity ωr and the local blade angle β. Induced velocities are not considered in this approximation. The freestream velocity vector is defined perpendicular to the rotor rotational plane, the rotational velocity vector is defined parallel to the rotational plane and the blade angle is the angle between

the rotational plane and the airfoil chord. In equation 1.1 [3], the so called speed ratio σ is defined as the ratio between the freestream velocity V and the product of the rotational velocity component experienced at a particular blade section of the propeller ωr and the tangent of the local blade angle β. In case the speed ratio is smaller than unity the rotor locally operates as a propeller, a unity speed ratio implies pinwheeling operation and in case the speed ratio is above unity, the rotor locally operates as a wind turbine. This can be verified by observing equation 1.1 in combination with the diagrams in figure 1.4. For propeller operation illustrated on the left hand side of figure 1.4, the product of the rotational velocity component experienced at a particular blade section of the propeller ωr and the tangent of the local blade angle β is larger than the freestream velocity V. From equation 1.1, this implies that the speed ratio σ is smaller than unity. This ensures that the orientation of the resultant velocity vector W, being a sum of the freestream velocity vector V and the local rotational velocity vector ωr, with respect to the section chord is such that the resultant thrust vector points towards the direction of flight, so that the rotor is locally functioning as a propulsive propeller. In the pinwheeling condition represented in the centre velocity diagram in figure 1.4, the magnitudes of the freestream velocity V and the product of local rotational velocity ωr and $\tan\beta$ are equal. In this situation, the resultant velocity vector W is parallel to the airfoil chord and for the considered symmetrical airfoil, this means that the section is unloaded. If all blade sections from root to tip are unloaded, the propeller is feathered and therefore not rotating. This operational mode will most likely not be applied during the regenerative mission, as it is mostly used on multi-engine aircraft to minimise drag on a propeller in case its corresponding engine fails. For turbine operation on the right hand side of figure 1.4, the product of the local rotational velocity component experienced at a particular blade section of the propeller ωr and the tangent of the local blade angle β is smaller than the freestream velocity V. Therefore, in this case σ is larger than unity and consequently, the orientation of the vector W with respect to the section chord is such that the resultant thrust vector points opposite to the flight direction, so that the rotor is locally functioning as a regenerative turbine.

$$\sigma = \frac{V}{\omega r \tan\beta} \tag{1.1}$$

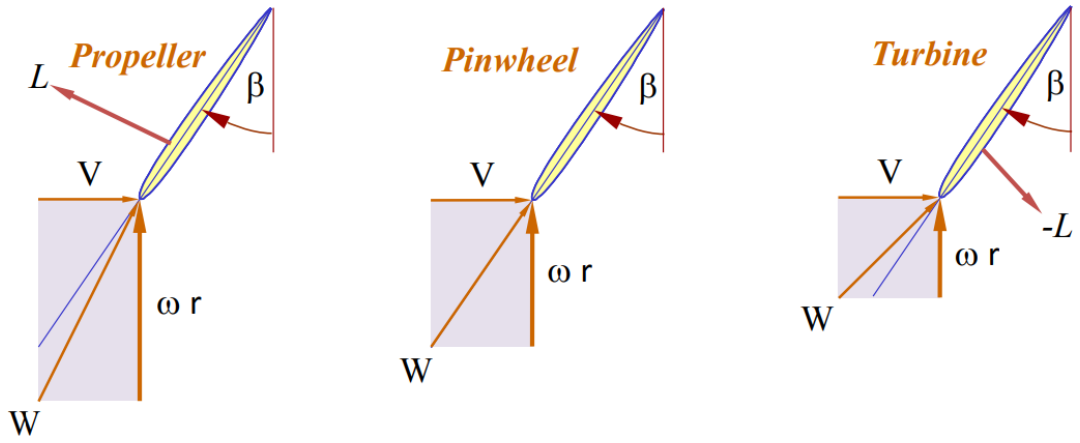

Figure 1.4: Rotor section velocity diagrams [3]

In figure 1.5 [3], a trend showing the efficiency of a rotor is presented as a function of the speed ratio σ. Starting from a low speed ratio below unity in propeller operation, the efficiency is relatively low, since the velocity vector is low with respect to the denominator in equation 1.1. This implies that the section is operating at a relatively large angle of attack that lies well beyond the optimum angle of attack for maximum aerodynamic efficiency. The latter is typically a low angle of attack that lies below the angle of attack for maximum lift coefficient for the particular airfoil. As the speed ratio increases towards unity, the efficiency increases until the relative magnitudes of the freestream velocity vector and rotational velocity are such that the section operates at its optimum angle of attack, after which it decreases again as unity is approached and the angle of attack is further reduced. Since a symmetrical section is considered, the turbine operation shows the same efficiency behaviour. For turbine operation, the angle of attack increases with the speed ratio and the optimum efficiency is found at a speed ratio above unity, at the same difference from unity as for the propeller due to symmetry. Since the section is unloaded in the pinwheeling condition, the efficiency falls to zero as unity is approached.

The efficiency behaviour as illustrated in figure 1.5 is congruent with the variable pitch propeller operation as discussed in section 1.4.1. At a given flight velocity, the combination of RPM and blade angle is generally selected such that the rotor as a whole operates at maximum efficiency.

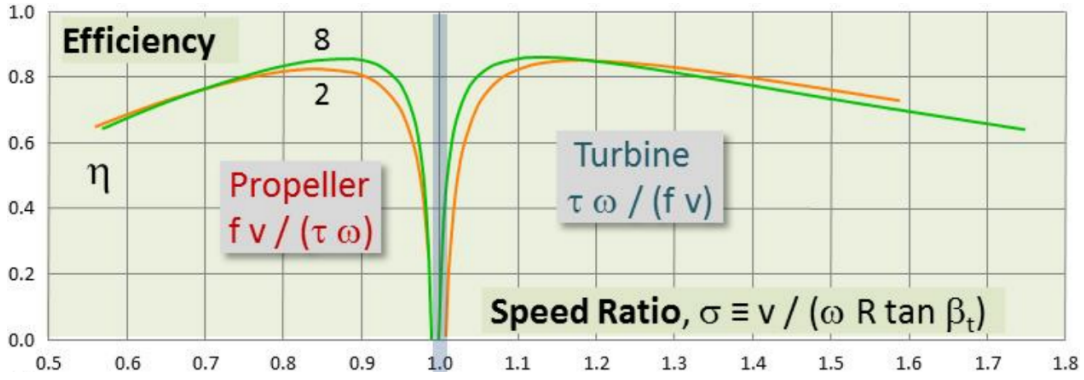

Figure 1.5: Rotor efficiency vs. speed ratio [3]

The basic principles of energy-harvesting propellers regarding the local operational conditions of blade sections discussed above are important to keep in mind during the energy-harvesting propeller design process. When designing a certain propeller blade geometry for application in multiple operational conditions, for every blade section it is desired to attain a compromise in its performance at these different conditions. Eventually, this is expected to lead to an overall propeller performance optimisation.

1.5. RESEARCH OBJECTIVE

In the current state of the art technology of regenerative propellers, it has been demonstrated already that energy consumption can significantly be reduced by replacing a conventional propulsive propeller by a dual-role propulsive and energy-harvesting propeller on an electric aircraft that complies with the remaining thrust and power requirements throughout the remaining flight mission profile. However, in order to further improve the optimisation of dual-role propeller designs, future research will focus on an investigation into the design of a variable pitch and RPM propeller for in-flight energy recuperation. These variables were both considered constant for the state of the art propeller designs so far [1]. The design optimisation of a dual-role propeller for an electric aircraft using variable pitch and RPM is the subject of this thesis research project. The research objective of this project is therefore formulated as follows:

"*The objective of the research project is to study the influence of varying the propeller blade pitch and/or RPM on the total propeller energy consumption of an electric aircraft for a given flight mission profile by performing an aerodynamic optimisation of an innovative dual-role propeller geometry and operating it in a windmilling, energy-harvesting mode during the descent, while simultaneously meeting the desired performance characteristics with respect to thrust and power delivery by the propeller in the remaining flight phases.*"

The energy consumption and energy harvesting performance of this variable pitch and RPM propeller is then compared to the performance of an optimised constant pitch and constant speed propeller for the same mission. It is expected that the energy performance of the variable pitch and RPM propeller will improve with respect to the constant pitch and constant speed propeller cases. For the constant pitch propeller, the pitch is kept constant during the entire flight mission, while the RPM is allowed to vary. For the constant speed propeller case, the propeller pitch is variable for the entire flight mission and the RPM is kept constant during climb and cruise, but variable during the descent.

1.6. THESIS SCOPE

When designing a complete propeller propulsion system, ideally it should be optimised from an aerodynamic, electric as well as a strategic mission design point of view. Furthermore, structural and propeller noise constraints are important to consider throughout the design process as well. In this project however, only the aerodynamic design optimisation of the propeller geometry is considered. In addition, the aerodynamic influence of the propeller hub and the propeller-nacelle interference are considered in the optimisation as well,

although viscous effects are not considered in these interference analyses. Considering the design of the propeller blade geometry, this is performed within the capabilities of the airfoil aerodynamic analysis program XFOIL and the limits of the selected propeller analysis model. In order to perform the propeller optimisation, knowledge about the airfoil aerodynamic coefficients is crucial. These are calculated using XFOIL, which has its limitations regarding the reliability of the aerodynamic data it calculates. In this project, XFOIL is used to perform compressible, viscous aerodynamic analysis on the airfoil sections. The results from these analyses can become less accurate for thick airfoils and/or the larger encountered (negative) angles of attack. Besides the limitations of XFOIL, the propeller analysis model also contains some assumptions that limit its accuracy. The main assumption made by the model is that the blades can be represented as lifting lines. This means that it is assumed that the induced velocity does not vary along the chord. However, this can be justified since relatively small chords are generally seen in aircraft propellers. For calculating the resultant blade section velocities, the induced velocities are therefore added as constants to the rotational and forward flight velocities.

1.7. THESIS OUTLINE

Including this introduction, this thesis contains seven chapters. Chapter 2 starts with a detailed explanation of propeller aerodynamics theory from which a propeller analysis model is then derived. This model then serves as an input to the propeller optimisation algorithm. In chapter 3, the propeller analysis model is validated by comparing the aerodynamic performance results of a propeller geometry to the results obtained from a windtunnel test, that was carried out by staff at Delft University of Technology, on the same propeller with the same performance output parameters. The validated propeller analysis model then serves as an input to the propeller optimisation algorithm, the latter being explained in detail in chapter 4. Chapter 5 discusses the results obtained from the single-point optimisations, where the propeller geometry is initially separately optimised for each flight phase, that is, for climb, cruise and descent. The overall mission energy performance for each separate optimisation case is then analysed, compared and discussed. In chapter 6, the results from the multi-point optimisations are discussed. Here, the propeller geometry is optimised for the whole flight mission at once. This is done for three operational cases: the constant pitch propeller, constant speed propeller and variable pitch propeller. The energy performances of each case are analysed, compared and discussed. Conclusions and recommendations that follow from this research project are finally subject of chapter 7.

2

PROPELLER ANALYSIS MODEL

In this chapter, a propeller analysis model is constructed. This model, based on the analysis procedure outlined in [4], is capable of calculating the propeller thrust, power and efficiency using a given input geometry and operational conditions in both propulsive and regenerative modes. The input geometry parameters are the propeller chord and blade angle distributions, airfoil distribution, propeller radius, hub radius and number of blades. The operational parameters are the propeller RPM and the flight velocity. In figure 2.1, the flowchart of the propeller analysis procedure is shown.

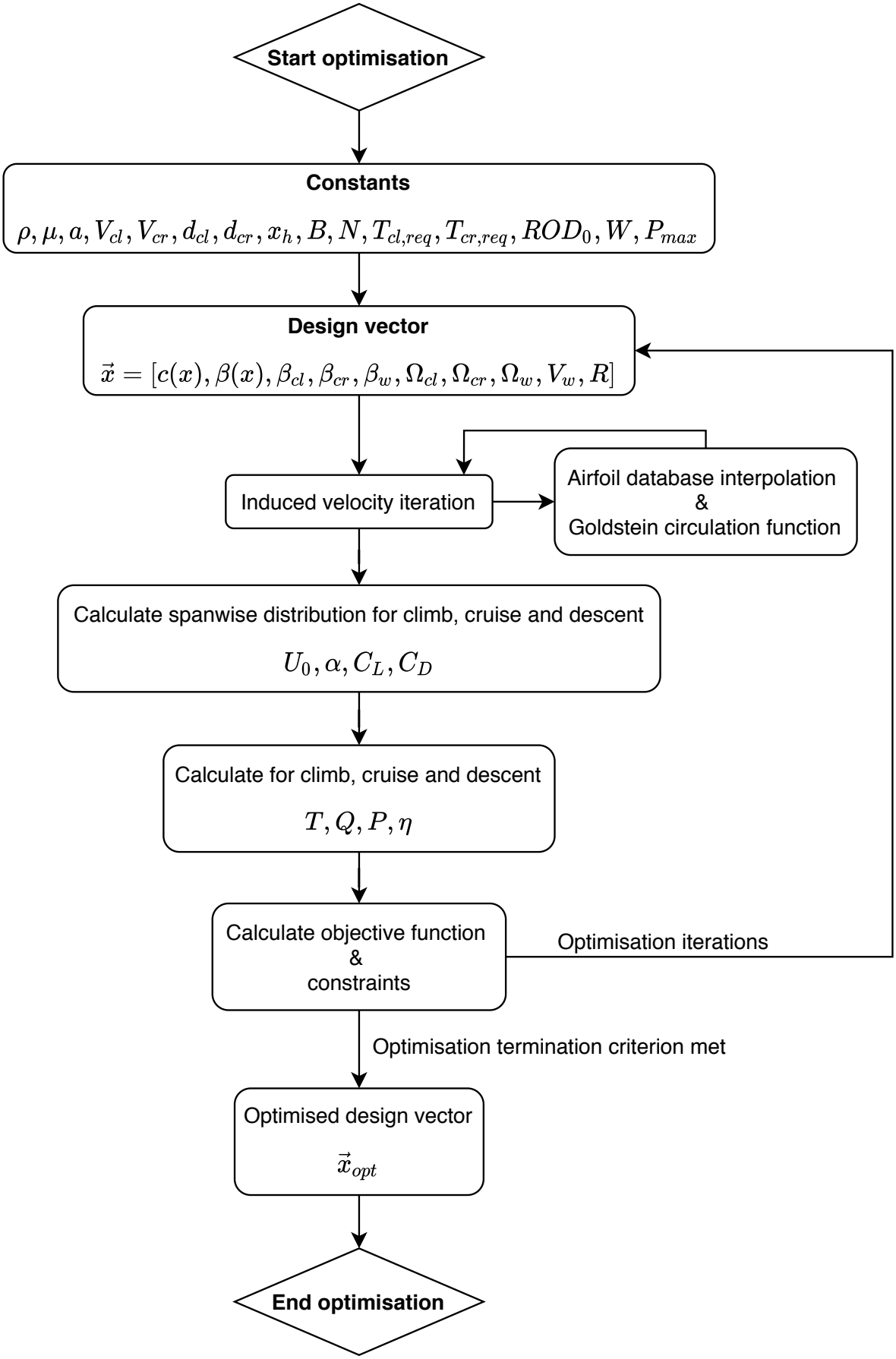

Figure 2.1: Propeller analysis flowchart

In the following sections, the propeller analysis procedure illustrated by the flowchart in figure 2.1 is explained in detail. In section 2.1, the definitions of essential propeller wake parameters are given and subsequently used in section 2.2 to derive expressions for the induced velocities at a propeller blade section. In section 2.3, the required Goldstein circulation function within the propeller analysis is introduced. Section 2.4 outlines a propeller-nacelle interference model and finally, the blade loading is calculated using the knowledge from the preceding sections in section 2.6.

2.1. PROPELLER WAKE PARAMETERS

In figure 2.2, the propeller trailing vortex system is illustrated, including the definitions of various radii the propeller analysis model uses. The propeller hub radius is denoted by x_h, r_0 represents the radial position of a propeller blade section and R_0 is the propeller radius. The subscript '1' is used to denote the trailing vortex radial distances as r_1 and R_1, as shown in figure 2.2.

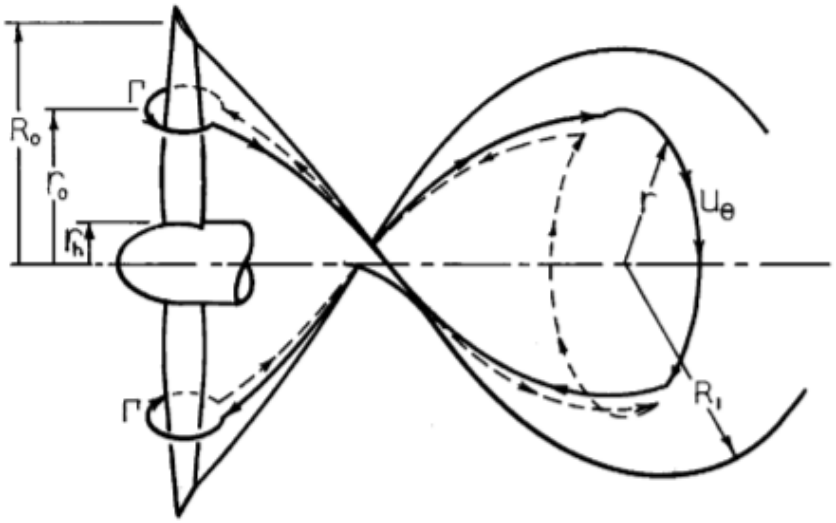

Figure 2.2: Propeller trailing vortex system [4]

Equation 2.1 represents the continuity relation between the flow through the propeller plane and the propeller wake. The velocity terms represent the sum of the airspeed V and the local axial induced velocity u_z.

$$\left(V + u_{z_0}\right) 2\pi r_0 \mathrm{d}r_0 = \left(V + u_{z_1}\right) 2\pi r_1 \mathrm{d}r_1 \tag{2.1}$$

A relation between the trailing vortex radius R_1 and the propeller radius R is required to be found for proceeding with the propeller analysis model. For this, it is assumed that the ratio between the velocity terms in equation 2.1 is a constant m, equation 2.2 results. Defining the normalised radial coordinate x by $x = r/R$, equation 2.2 can be written as in equation 2.3. Solving the integrals in equation 2.3, equation 2.4 results.

$$m \int_{r_h}^{r_0} r_0 \mathrm{d}r_0 = \int_0^{r_1} r_1 \mathrm{d}r_1 \tag{2.2}$$

$$m \left(R_0/R_1\right)^2 \int_{x_h}^{x_0} x_0 \mathrm{d}x_0 = \int_0^{x_1} x_1 \mathrm{d}x_1 \tag{2.3}$$

$$x_0^2 = x_h^2 + x_1^2 \left(R_1/R_0\right)^2 / m \tag{2.4}$$

The boundaries x_0 and x_1 are equal to 1 and therefore, equation 2.5 results. From equations 2.4 and 2.5, equation 2.6 can be derived. Equation 2.6 relates the trailing vortex radial coordinate x_1 to the normalised radial coordinate x_0 of a propeller blade section.

$$\left(R_1/R_0\right)^2 / m = 1 - x_h^2 \tag{2.5}$$

$$x_0^2 = x_h^2 + x_1^2\left(1 - x_h^2\right) \rightarrow x_1 = \sqrt{\frac{x_0^2 - x_h^2}{1 - x_h^2}} \tag{2.6}$$

Using equation 2.6 and omitting the subscript '0' from now on for parameters at the propeller plane, equation 2.7 can be derived, relating the trailing vortex radius R_1 is related to the propeller radius R.

$$R_1 = \frac{r}{x_1} = \frac{x}{x_1}R = xR\sqrt{\frac{1 - x_h^2}{x^2 - x_h^2}} \tag{2.7}$$

Three advance ratios used in the propeller analysis model, λ, λ_1 and λ_2, are defined in equations 2.8 - 2.10 respectively, where R_1 in equation 2.9 is calculated using equation 2.7. The value of the normalised wake velocity $\bar{w}$ required to compute λ_2 is obtained together with the section lift coefficient C_l by iteration as explained in section 2.5.

$$\lambda = \frac{V}{\Omega R} \tag{2.8}$$

$$\lambda_1 = \frac{V}{\Omega R_1} \tag{2.9}$$

$$\lambda_2 = \frac{V + w}{\Omega R_1} = \lambda_1(1 + \bar{w}) \tag{2.10}$$

2.2. BLADE INDUCED VELOCITIES

In this section, expressions for the blade induced velocities are derived using the defined propeller wake parameters from section 2.1. In figure 2.3, the axial and tangential vortex induced velocities u_{z_1} and u_{θ_1} are defined. The aim is to relate these to the actual propeller blade induced velocities u_{z_0} and u_{θ_0}, which contribute to the resultant velocities seen at the blade sections.

The induced axial and tangential velocities in the trailing vortex system, u_{z_1} and u_{θ_1} respectively, as a function of the wake velocity w and the pitch angle of the vortex sheet ϕ are given by equations 2.11 and 2.12 and follow from the geometry in figure 2.3. Using equation 2.13, which can be derived from equations 2.10 and equation 2.7, the induced velocities can alternatively be written as a function of λ_2 and the non-dimensional radial coordinate in the trailing vortex system x_1. This results in equations 2.14 and 2.15.

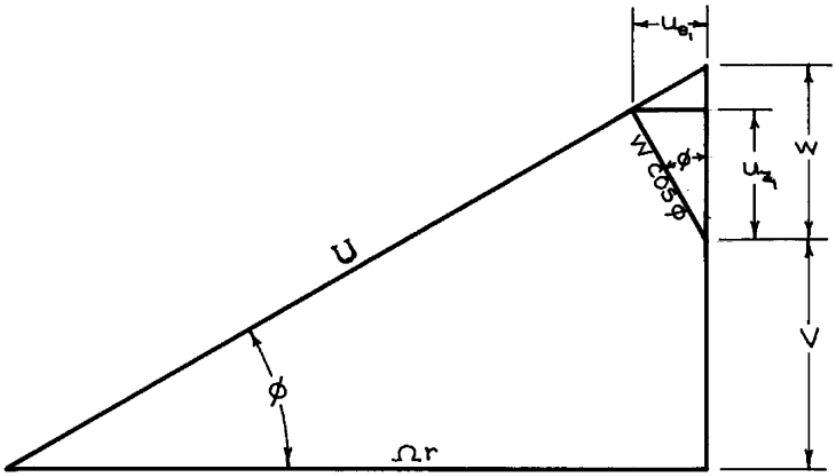

Figure 2.3: Propeller helicoidal vortex sheet velocity components [4]

$$u_{z_1} = w\cos^2\phi \tag{2.11}$$

$$u_{\theta_1} = w\cos\phi\sin\phi \tag{2.12}$$

$$\tan\phi = \frac{\lambda_2}{x_1} \tag{2.13}$$

$$u_{z_1} = \frac{w}{1 + \lambda_2^2/x_1^2} \tag{2.14}$$

$$u_{\theta_1} = \frac{w(\lambda_2/x_1)}{1 + \lambda_2^2/x_1^2} \tag{2.15}$$

An important concept that plays a role in relating the vortex wake induced velocities to the induced velocities at the propeller blades is the relation between the bound circulation on a propeller blade and the shed vorticity. This relation is given by equation 2.16 and states that the total bound circulation of a propeller blade at a particular radial position r equals the vorticity shed within a radius r_1 in the vortex wake, originating from the vortex filament shed by the propeller blade element at r.

$$B\Gamma(r) = \int_0^{2\pi} u_\theta(r_1) r_1 \mathrm{d}\theta = B\Gamma(r_1) \tag{2.16}$$

From the Biot-Savart law, it can be derived that the induced velocities at the propeller plane are half the magnitude of the ones at a point in the vortex sheet corresponding to the point at the propeller plane where the vortex was shed. From equation 2.16, it is also known that $r u_\theta$ is constant. Therefore, the expression given by equation 2.17 can be written, from which equation 2.18 is derived by substitution of equations 2.15 and 2.8 - 2.10. Equation 2.18 is used to calculate the tangential induced velocity as seen at the propeller blade sections. Similarly, equation 2.19 is derived and used to calculate the axial induced velocity at the propeller blade sections. In equations 2.17 - 2.19, use is made of $\bar{u} = u/V$, $\bar{w} = w/V$ and $x = r/R$.

$$u_{\theta_0} r_0 = \frac{1}{2} u_{\theta_1} r_1 \rightarrow \bar{u}_{\theta_0} x R_0 = \frac{1}{2} \bar{u}_{\theta_1} x_1 R_1 \tag{2.17}$$

$$\bar{u}_{\theta_0} = \frac{1}{2} \bar{u}_{\theta_1} (x_1/x)(R_1/R_0) = \frac{1}{2} \bar{w}(1+\bar{w})(\lambda/x)/(1+\lambda_2^2/x_1^2) \tag{2.18}$$

$$\bar{u}_{z_0} = \frac{1}{2} \bar{u}_{z_1} = \frac{1}{2} \bar{w}/(1+\lambda_2^2/x_1^2) \tag{2.19}$$

2.3. THE GOLDSTEIN CIRCULATION FUNCTION

The Goldstein circulation function is a function that contributes to relating the propeller wake properties to the desired distribution of circulation on the propeller for optimum performance, and hence it is required for the calculation of the final propeller blade loading. Therefore, before proceeding with the calculation of the aerodynamic coefficients and the propeller performance parameters in sections 2.5 and 2.6 respectively, the Goldstein circulation function is discussed here first.

For the trailing vortex sheet, the Goldstein circulation function can be expressed as a dimensionless factor as in equation 2.20, wherein the trailing vortex circulation $\Gamma(r_1)$ is made non-dimensional by the multiplication of the distance between the vortex sheets h and the backward vortex wake velocity w. The distance h is defined in equation 2.21 as the ratio between the linear vortex sheet pitch and the number of blades. Substituting equation 2.21 into equation 2.20 and using the definition of λ_2 from equation 2.10, equation 2.20 is written as in equation 2.22.

$$G(r_1) = \frac{\Gamma(r_1)}{hw} \tag{2.20}$$

$$h = \frac{P}{B} = \frac{2\pi(V+w)}{\Omega B} \tag{2.21}$$

$$G(r_1) = \frac{B\Gamma\Omega}{2\pi w(V+w)} = \frac{B\Gamma}{2\pi R_1 w \lambda_2} \tag{2.22}$$

The circulation is defined by equation 2.23, in which the tangential vortex induced velocity u_{θ_1} is calculated using equation 2.15. Consequently, the basic Goldstein circulation function can be written as a function of only the non-dimensional radial coordinate at the propeller plane x and λ_2 as in equation 2.24.

$$\Gamma = \frac{2\pi r u_{\theta_1}}{B} \tag{2.23}$$

$$\frac{B\Gamma\Omega}{2\pi(V+w)w} = \frac{x^2}{x^2+\lambda_2^2} \tag{2.24}$$

Including a vortex sheet tip correction factor F given by equation 2.25, an approximation to the Goldstein circulation function is given by equation 2.27. In equation 2.25, the parameter f is given by equation 2.26.

$$F = \frac{2}{\pi} \cos^{-1} \mathrm{e}^{-f} \tag{2.25}$$

$$f = \frac{B}{2}(1-x)\frac{\sqrt{1+\lambda_2^2}}{\lambda_2} \tag{2.26}$$

$$G(x, \lambda_2, B) \cong \frac{Fx^2}{x^2 + \lambda_2^2} \tag{2.27}$$

The exact formulation of the Goldstein circulation function corresponds to significantly more complicated mathematics which are out of the scope of this project and instead, tabulated numerical values representing exact solutions to the function at certain combinations of x, λ_2 and the number of blades B are used. These Goldstein circulation function tables can be found in [4]. By numerically interpolating the tabulated function data, the function value $G(x, \lambda_2, B)$ can be obtained for any combination of x, λ_2 and B. In figures 2.4 and 2.5, the Goldstein circulation function distributions for multiple values of λ_2 are plotted for two and three blades respectively using the tabulated function data as provided in [4].

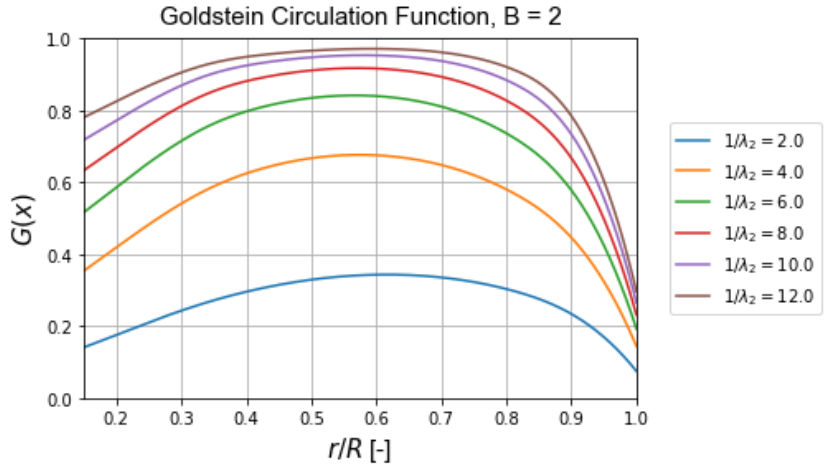

Figure 2.4: Goldstein circulation function for 2 blades

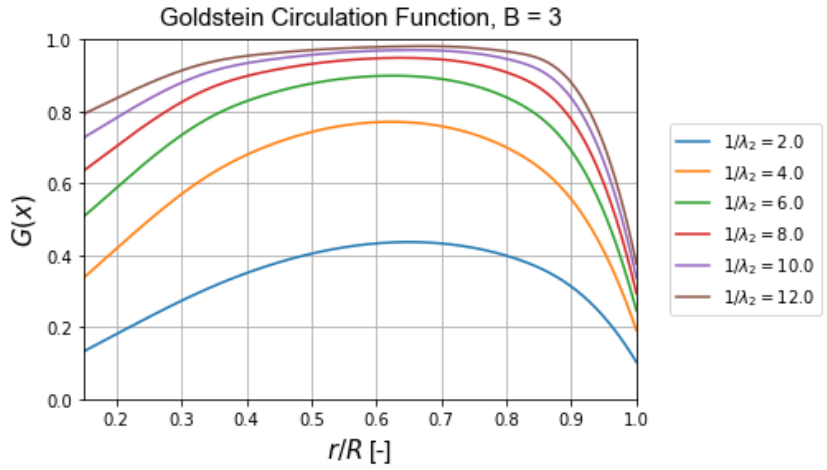

Figure 2.5: Goldstein circulation function for 3 blades

2.4. PROPELLER-NACELLE INTERFERENCE

In this section, a model for analysing the influence of the nacelle on the aerodynamics and design of a propeller is investigated based on the findings in [4]. The nacelle influences the local resultant velocities seen at the propeller blade sections and therefore, before proceeding to the calculation of the blade loading in section 2.6, the propeller-nacelle interference model is discussed here first.

On the right in figure 2.6, the influence of a nacelle behind a propeller on the flow field is illustrated with respect to a free-running propeller on the left. In order to know how the nacelle influences the aerodynamic propeller design, the radial coordinates of the free-running and nacelle-influenced propellers need to be

related. The nacelle-influenced propeller will have to be designed with a slightly adjusted distribution of circulation over a larger radius and will lead to a higher thrust if it would be free-running, however, the nacelle drag reduces the net thrust so that in the end the design thrust requirement is still met [4].

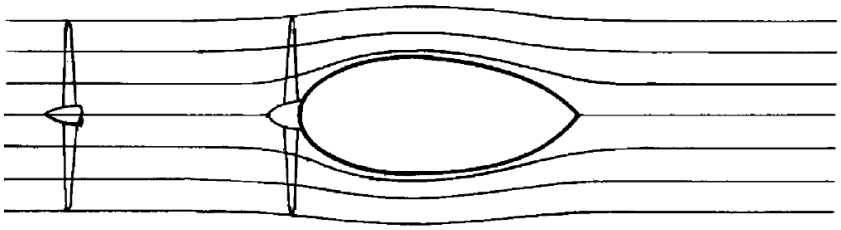

Figure 2.6: Influence of the nacelle on the flow field [4]

A new variable Ψ in equation 2.28 is introduced that relates the radii of the free-running and nacelle-influenced propellers to each other. The radial coordinates of the free-running and nacelle-influenced propellers are given by r and r_0 respectively. The velocity u_{zN} accounts for the disturbance in the flowfield as a result of the presence of the nacelle and represents the velocity component in the axial direction in the propeller plane. Making the assumption that the flow velocity through the propeller plane $(V + u_{z_0})$ is constant, equation 2.29 is obtained.

$$\Psi = \int_0^r (V + u_{z_0}) r \mathrm{d}r = \int_0^{r_0} (V + u_{z_0} + u_{zN}) r_0 \mathrm{d}r_0 \tag{2.28}$$

$$(V + u_{z_0})(r^2 - r_0^2)/2 = \int_0^{r_0} u_{zN} r_0 \mathrm{d}r_0 \tag{2.29}$$

Figure 2.7 represents a nacelle with a flowfield around it modelled as the addition of a freestream flow with a source Q at a distance of $a/2$ from the nose, where a is the distance from the asymptotic point of curvature of the nacelle to its symmetrical centreline. The distance b represents the distance between the nose of the nacelle and the propeller plane. The axial velocity due to the presence of the nacelle points in the negative direction and is given by the expression in equation 2.30 where k is given by equation 2.31.

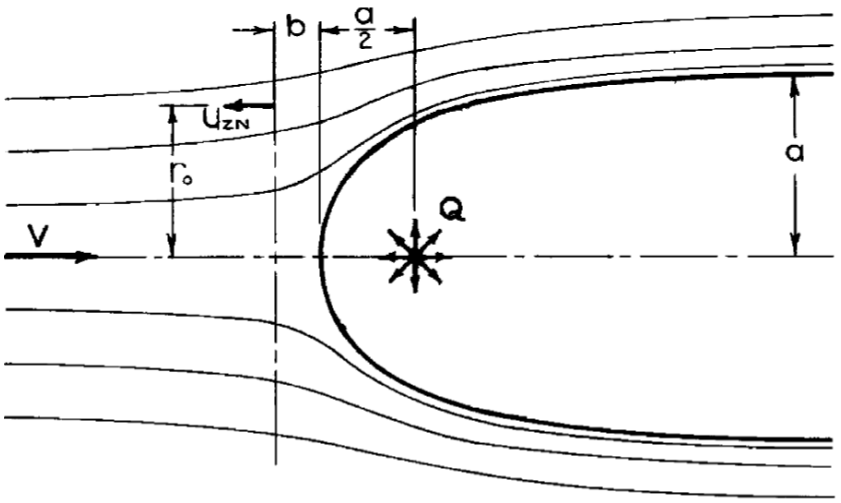

Figure 2.7: Flowfield around the nacelle nose [4]

$$\bar{u}_{zN} = \frac{u_{zN}}{V} = -\frac{k/4}{[(r_0/a)^2 + k^2]^{3/2}} \tag{2.30}$$

$$k = \frac{b}{a} + \frac{1}{2} \tag{2.31}$$

Substituting equation 2.30 into equation 2.29 and integrating results in an expression relating the radii of the free-running and nacelle-influenced propellers given by equation 2.32.

$$(1+\bar{u}_{z_0})(r^2-r_0^2)=\frac{1}{2}a^2\left[\frac{ka}{\sqrt{r_0^2+k^2a^2}}-1\right] \tag{2.32}$$

Therefore, for each radial value r of the initially designed free-running propeller, the corresponding radial value for the nacelle-influenced propeller r_0 is calculated using equation 2.32 and then u_{zN} follows from equation 2.30.

The contribution to the axial blade element velocity by the propeller-nacelle interference from equation 2.30 must be added to the axial velocity calculated without interference, as will become clear in section 2.5.

2.5. DISTRIBUTION OF BLADE LIFT AND DRAG COEFFICIENTS

In this section, the procedure for obtaining the lift and drag coefficient distributions along the blade span is presented. Use is made of the induced velocity results, the Goldstein circulation function and the contribution of the nacelle to the local velocities at the blade elements as discussed previously in sections 2.2, 2.3 and 2.4 respectively.

The lift d$\mathbf{L}$ of a propeller blade element of radial dimension dr in vector form is given by the Kutta–Joukowsky theorem in equation 2.33, where $\mathbf{U}_0$ is the resultant velocity seen by the blade element and Γ is the circulation.

$$\mathrm{d}\mathbf{L}=\rho\mathbf{U}_0\times\Gamma\mathrm{d}r \tag{2.33}$$

The section lift can also be written as a function of the section lift coefficient C_l, the air density ρ, the resultant blade element velocity U_0 and the local chord length c as in equation 2.34. This is then related to the circulation using equation 2.33.

$$\mathrm{d}L=C_l\frac{\rho}{2}U_0^2c\mathrm{d}r=\rho\Gamma U_0\mathrm{d}r \tag{2.34}$$

Multiplying equation 2.34 by the number of blades B and rearranging terms, equation 2.35 results. Rewriting equation 2.22, the product of B and Γ can also be written as in equation 2.36.

$$B\Gamma=\frac{1}{2}C_lBcU_0=C_l\sigma\pi RU_0 \tag{2.35}$$

$$B\Gamma=2\pi R_1w\lambda_2G(x,\lambda_2,B)=2\pi R\lambda w(1+\bar{w})G(x,\lambda_2,B) \tag{2.36}$$

By setting equations 2.35 and 2.36 equal to each other, the theoretical lift coefficient can be written as in equation 2.37.

$$C_{l,th}=\frac{2\lambda\bar{w}(1+\bar{w})G(x,\lambda_2,B)}{\sigma U_0/V} \tag{2.37}$$

In equation 2.37, the resultant local velocity U_0 a blade element at radial position x is exposed to is a function of the flight velocity V, the rotational velocity Ωr and the induced velocities u_{θ_0} and u_{z_0} at the blade element. Figure 2.8 represents a propeller blade element including all the velocities and angles it is exposed to. The blade angle β is the angle between the section chord and the rotational plane. The inflow angle ϕ_0 is the angle between the resultant velocity seen by the blade element U_0 and the rotational plane. The angle of attack α is the angle between the section chord and the resultant velocity vector. From geometry in figure 2.8 and including the contribution of the nacelle-interference from section 2.4 to the axial velocity, it follows that the resultant velocity can be written as in equation 2.38. Normalising the resultant velocity with the flight velocity V results in equation 2.39.

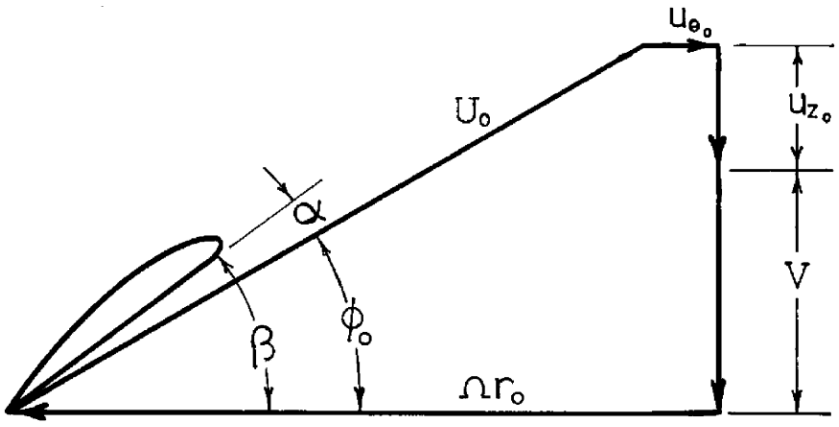

Figure 2.8: (Induced) velocities on a propeller blade element [4]

$$U_0 = \sqrt{(V + u_{z_0} + u_{zN})^2 + (\Omega r - u_{\theta_0})^2} \tag{2.38}$$

$$U_0/V = \sqrt{(1 + \bar{u}_{z_0} + \bar{u}_{zN})^2 + (x/\lambda - \bar{u}_{\theta_0})^2} \tag{2.39}$$

Equation 2.39 is used to calculate the normalised resultant velocity U_0/V in equation 2.37. Equation 2.37 relates the section lift coefficient to several wake parameters, which are all known as a function of the propeller operational conditions and propeller geometry input parameters at this point, as derived in section 2.2. It remains to determine the distribution of the normalised wake velocity $\bar{w}$ along the propeller blade sections. For this, another function that relates C_l to $\bar{w}$ is required in order to have two equations with two unknowns. The section lift coefficient can also experimentally be determined, in this project using XFOIL as discussed later in section 4.6, as a function of the local angle of attack, Mach number and Reynolds number. This representation of the lift coefficient is given by equation 2.40. In equation 2.40, the lift coefficient is obtained from an aerodynamic database of the airfoil under consideration, by interpolating tabulated data of C_l at various combinations of α, M and Re as explained later in more detail in section 4.6.

$$C_{l,exp} = f(\alpha, M, Re) \tag{2.40}$$

From geometry in figure 2.8, the angle of attack α as an input to equation 2.40 is given by equation 2.41, in which β is the blade angle and ϕ is the inflow angle. The blade angle is known from the input propeller geometry and the inflow angle follows from geometry in figure 2.8 and is given by equation 2.42, where again the contribution of the nacelle-interference to the axial velocity is included.

$$\alpha = \beta - \phi \tag{2.41}$$

$$\tan\phi = \frac{V + u_{z_0} + u_{zN}}{\Omega r - u_{\theta_0}} = \frac{1 + \bar{u}_{z_0} + \bar{u}_{zN}}{x/\lambda - \bar{u}_{\theta_0}} \tag{2.42}$$

The section Mach and Reynolds numbers are calculated using equations 2.43 and 2.44 respectively, with the section resultant velocity U_0 given by equation 2.38.

$$M = \frac{U_0}{a} \tag{2.43}$$

$$Re = \frac{\rho U_0 c}{\mu} \tag{2.44}$$

At this point, two equations for the lift coefficient are obtained and given by equations 2.37 and 2.40. These equations can be solved using an iterative procedure where at each radial position of the blade, the value for $\bar{w}$ is determined such that they result, within a certain predefined accuracy, in the same value for C_l. In order to carry out the iteration, the function given by equation 2.45 should be minimised up the given tolerance. The iterations stop when the function reaches a value below the tolerance.

$$f(\bar{w}) = \mid C_{l,th} - C_{l,exp} \mid \tag{2.45}$$

Using the obtained distribution of the normalised wake velocity $\bar{w}$ along the blade, the radial distributions of the lift and drag coefficients $C_l(x)$ and $C_d(x)$ along the blade follow from equations 2.46 and 2.47 respectively and by interpolation within the airfoil aerodynamic database for the lift and drag coefficients at given α, M and Re.

$$C_l(x,\bar{w}) = f\big(\alpha(x,\bar{w}), M(x,\bar{w}), Re(x,\bar{w})\big) \tag{2.46}$$

$$C_d(x,\bar{w}) = f\big(\alpha(x,\bar{w}), M(x,\bar{w}), Re(x,\bar{w})\big) \tag{2.47}$$

2.6. PROPELLER THRUST, POWER AND EFFICIENCY

As will become clear later, ultimately it is of interest to obtain the propeller energy consumption which is a function of the propeller thrust and efficiency. The propeller power is also required for verifying whether the set power constraint is met.

In order to derive expressions for the propeller thrust, power and efficiency, consider figure 2.9 where the forces acting on a propeller blade section are defined. The lift L and drag D forces, resulting from the lift and drag coefficient distributions found in section 2.5, acting on the section are directed perpendicular and parallel to the incoming resultant flow velocity vector U_0 respectively. The sum of the lift and drag forces results in an aerodynamic resultant force F_{res}. The horizontal component of this resultant force along the propeller rotational plane represents the torque Q generated by the blade section and the vertical component perpendicular to the rotational plane represents the thrust T.

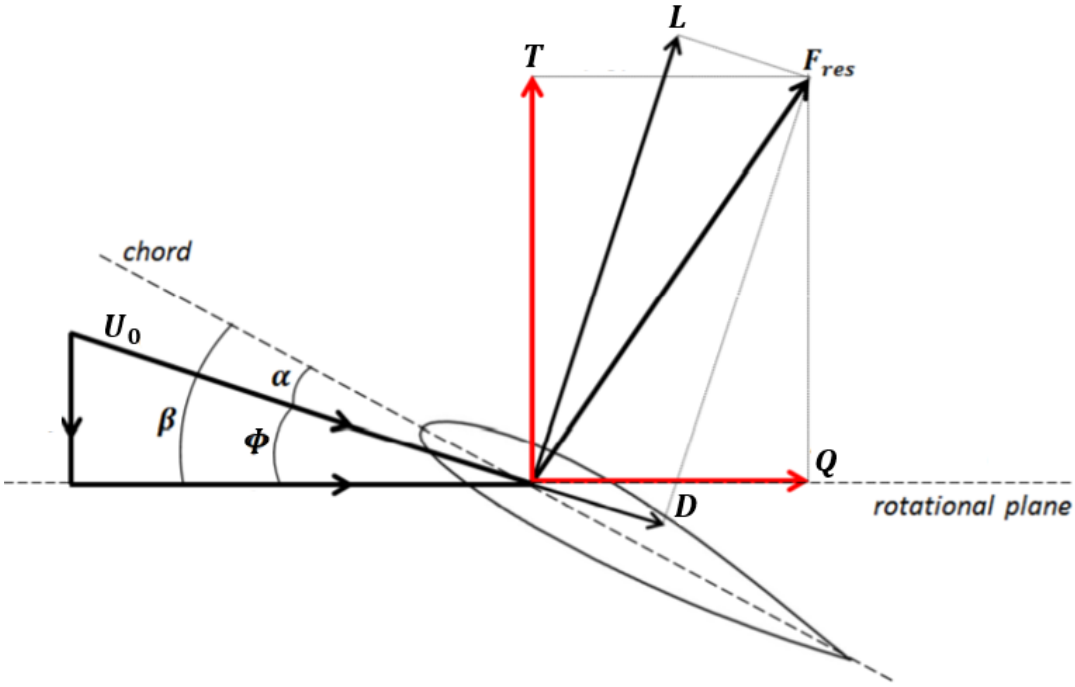

Figure 2.9: Forces on a propeller blade element

For a blade element of area cdr, where $dr = Rdx$, the blade section thrust follows from geometry in figure 2.9 and is given by equation 2.48. Similarly, the blade section torque is given by equation 2.49.

$$dT = B(dL\cos\phi - dD\sin\phi) = \frac{1}{2}\rho B U_0^2 (C_l\cos\phi - C_d\sin\phi)cRdx \tag{2.48}$$

$$dQ = B(dL\sin\phi + dD\cos\phi) = \frac{1}{2}\rho B U_0^2 (C_l\sin\phi + C_d\cos\phi)cRdx \tag{2.49}$$

The section thrust and torque coefficients are defined in equations 2.50 and 2.51 respectively [4]. Substituting equations 2.48 and 2.49 into equations 2.50 and 2.51, the propeller thrust and torque coefficients are then calculated using equations 2.52 and 2.53 by summing the sectional coefficient values at all blade elements dx from root to tip. In equations 2.52 and 2.53, the solidity factor σ is defined in equation 2.54. By definition, the propeller power coefficient and efficiency then follow from equations 2.55 and 2.58.

$$dK_T = \frac{dT}{\frac{1}{2}\rho\pi R^2 V^2} \tag{2.50}$$

$$dK_Q = \frac{dQ}{\frac{1}{2}\rho\pi R^3 V^2} \tag{2.51}$$

$$K_T = 2\int_{x_h}^{1} (C_l \cos\phi - C_d \sin\phi)\sigma(U_0/V)^2 \mathrm{d}x \tag{2.52}$$

$$K_Q = 2\int_{x_h}^{1} (C_l \sin\phi + C_d \cos\phi)\sigma(U_0/V)^2 x\mathrm{d}x \tag{2.53}$$

$$\sigma = \frac{Bc}{2\pi R} \tag{2.54}$$

$$K_P = \frac{K_Q}{\lambda} \tag{2.55}$$

The total propeller thrust, power and efficiency can finally be calculated using equations 2.56 - 2.58.

$$T = K_T \frac{1}{2}\rho\pi R^2 V^2 \tag{2.56}$$

$$P = K_P \frac{1}{2}\rho\pi R^2 V^3 \tag{2.57}$$

$$\eta_p = \frac{K_T}{K_P} \tag{2.58}$$

In the case of a windmilling propeller, the air is decelerated rather than accelerated through the rotor disk and as a result, the directions of the axial and tangential velocities are opposite as compared to the blade velocity diagram of a propeller as was seen in figure 2.8. The blade velocity diagram in the windmill case is shown in figure 2.10.

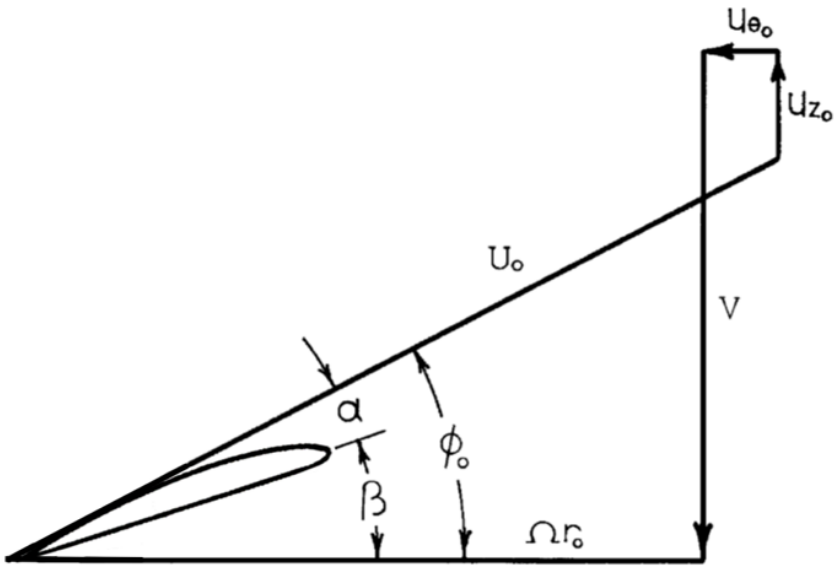

Figure 2.10: (Induced) velocities on a windmilling propeller blade element [4]

The aerodynamic performance analysis of a windmilling propeller of given geometry can be carried out using the same procedure as for the propulsive propeller, with a minor adjustment. For a windmilling propeller, the power coefficient represents its aerodynamic efficiency. Therefore, instead of equation 2.58 that holds for the propulsive propeller, equation 2.59 is used for a windmilling propeller. What's more, the normalised wake velocity $\bar{w}$ attains a negative value for a windmilling propeller, while for a propulsive propeller it is positive.

$$K_P = \eta_w = \frac{K_Q}{\lambda} \tag{2.59}$$

3

VALIDATION OF THE PROPELLER ANALYSIS MODEL BY A WINDTUNNEL EXPERIMENT

In this section, a validation study is performed with the aim of validating the propeller analysis calculations performed during the optimisation using the results found from a windtunnel test, performed by Delft University of Technology staff, on the energy recuperation ability of an existing propeller. By inputting the geometry of the reference propeller into the propeller analysis code, the aerodynamic performance of the propeller is simulated and compared it to the available experimental data resulting from the windtunnel test. The aerodynamic performance is represented by plots of the thrust and power coefficients against the advance ratio.

3.1. VALIDATION SETUP

In this section, the validation procedure is outlined. The propeller thrust and power coefficients are defined by equations 3.1 and 3.2 respectively. These are aimed to be plotted against propeller advance ratio as defined by equation 3.3.

$$K_T = \frac{T}{\frac{1}{2}\rho V_\infty^2 \pi R^2} \tag{3.1}$$

$$K_P = \frac{P}{\frac{1}{2}\rho V_\infty^3 \pi R^2} \tag{3.2}$$

$$J = \frac{V_\infty}{nD} \tag{3.3}$$

For performing the validation study, several values of the advance ratio J are selected in the range used during the windtunnel experiment; $0.5 \leq J \leq 1.8$. For each value of J, the corresponding freestream velocity V_∞ is obtained from the graph in figure 3.1. The test velocity used in the windtunnel experiment is plotted against the advance ratio in figure 3.1. This graph depicts the combinations of velocity and advance ratios to which the windtunnel test runs have been performed. The velocity was varied since the objective of the windtunnel experiment was to obtain a constant Reynolds number at $r/R = 0.7$ at all advance ratios. As can be seen from figure 3.1, the velocity increases with advance ratio, which is in line with equation 3.3. The propeller rotational velocity Ω then follows from equation 3.4.

$$\Omega = 2\pi n = \frac{2\pi V_\infty}{JD} \tag{3.4}$$

All the blade geometry parameters are known and therefore, at this point the thrust and power coefficients can be calculated using the same propeller analysis procedure as outlined before in chapter 2, but this time using the given airfoil distribution used in the reference propeller.

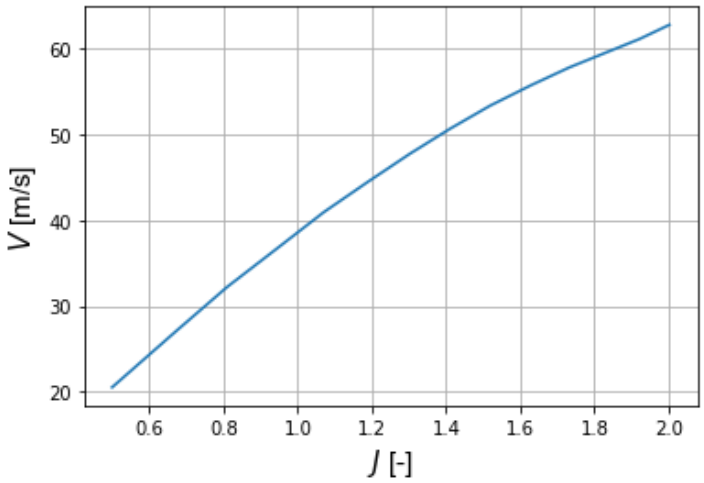

Figure 3.1: Windtunnel test velocities vs. advance ratio

3.2. RESULTS

In figure 3.2, the thrust coefficient is plotted against the advance ratio for the developed numerical propeller analysis code and the experimental windtunnel result. As can be seen, the curves closely match over most of the advance ratio range. However, a slight offset is seen for higher advance ratio values. This can be explained with the aid of equation 3.3 and figure 2.10. For higher advance ratios, the ratio between the velocity vector V and the rotational velocity vector increases. From the velocity triangle of the propeller blade section, it becomes clear that this means that the angle of attack becomes more negative. The reference propeller considered for the validation study consists of positively cambered and, in particular in the tip region, very thin airfoils. At large negative angles of attack, the lift and drag results obtained from an aerodynamic analysis using XFOIL become less reliable. As a result, the prediction of the thrust coefficient values at higher advance ratios becomes less accurate, and this can clarify the offset seen between the numerical and experimental results in figure 3.2.

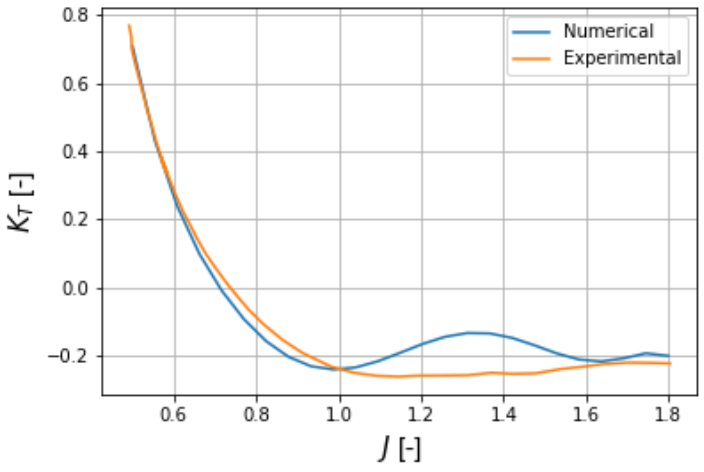

Figure 3.2: Numerical and experimental thrust coefficient vs. advance Ratio

In figure 3.3, the power coefficient is plotted against the advance ratio. Also here some offset is visible at higher advance ratios for the same reasons as discussed for the thrust coefficient above.

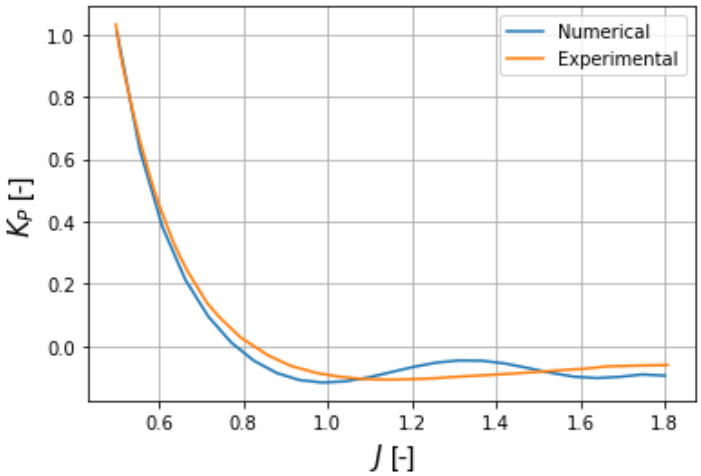

Figure 3.3: Numerical and experimental power coefficient vs. advance ratio

Overall, it can be concluded that there is some offset of the numerical results with respect to the experimental results. However, the reasons for the observed offsets seen can clearly be explained and these are expected to significantly decrease in case the reference propeller would be composed of airfoils with a more moderate thickness and camber instead of the very low thickness and very high camber used in particular at the tip regions of the propeller in the present analysis. This means that the validation of the propeller analysis model can be justified and these offset observations are taken into account for the airfoils selection procedure with respect their camber and thickness when defining the optimisation problem in chapter 4.

4

PROPELLER OPTIMISATION

In this section, the method used to perform an aerodynamic design optimisation of a dual-role propulsive and energy-harvesting propeller for a reference electric aircraft is outlined. This includes the generation of an optimisation objective function, design variables and constraints as well as the selection of a suitable optimisation algorithm. Based on the discussed optimisation method, various optimisation cases are proposed, distinguished by the type of propeller pitch and RPM operation as well as by optimisation for separate parts of the flight mission and the complete mission.

4.1. REFERENCE AIRCRAFT AND FLIGHT MISSION PROFILE

In this project, an aerodynamic optimisation of a dual-role propeller to be applied on a selected reference electric aircraft is aimed to be carried out. In order to perform this optimisation, a few aircraft design and operational parameters are required as inputs to the optimisation. In this section, a reference aircraft as part of the optimisation framework is therefore introduced and motivated as a first step in the optimisation process.

The reference aircraft chosen for this project is the Pipistrel Alpha Electro aircraft, shown in figure 4.1. Details on the design parameters and mission characteristics of the aircraft can be found in the flight manual in [18]. The Pipistrel Alpha Electro is a good example of the state of the art technology in the area of energy-harvesting propeller application on electric aircraft. It is the first fully electric powered aircraft with energy recuperation ability and high potential for further developments and improvements to be implemented in the future [1]. It is therefore very well suitable as a reference aircraft to be used for the goal of this project of designing and optimising the performance of a energy-harvesting propeller that is aimed to minimise the energy consumption of an electric aircraft.

Figure 4.1: Pipistrel's alpha electro aircraft [5]

Concerning the aircraft mission, the Pipistrel Alpha Electro is mainly designed for short-range missions and flying traffic pattern circuits [1]. In this project however, propeller optimisations are carried out for various cruise distances ranging from short-range missions to the maximum range specified for the aircraft of 200km [18]. Longer distances are included as well as these might be interesting to consider for future electric aircraft operation. A regular mission consisting of a single climb, cruise and descent phase is considered for the propeller optimisation in this project. In figure 4.2, the mission geometry is illustrated, including the values of all the constant mission parameters. Examples of parameters required for the propeller optimisation are the climb and cruise velocities and the climb gradient of the aircraft as shown in figure 4.1. During each separate flight phase, the flight velocity is assumed to be constant. Also, the aircraft weight, cruise altitude and maximum motor power of 60 kW are important input parameters. The aircraft weight, climb and cruise velocities, the rate of climb and the rate of descent at zero recuperation are constant aircraft parameters [18]. The climb angle γ is calculated from equation 4.1 for a rate of climb of $RC = 6.1$ m/s. Furthermore, the aircraft weight is $W = 5395.5$ N.

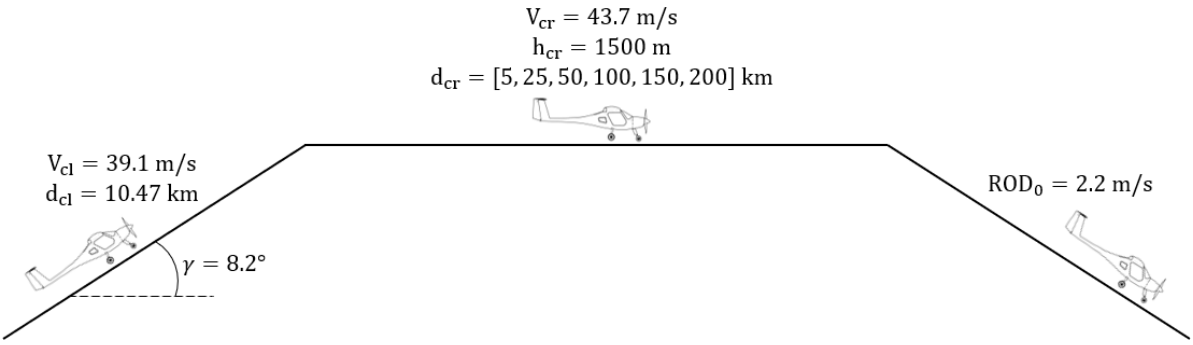

Figure 4.2: Pipistrel alpha electro mission profile

$$\gamma = \sin^{-1} \frac{RC}{V_{cl}} \tag{4.1}$$

4.2. OBJECTIVE FUNCTION

In this section, the objective function for the dual-role propeller optimisation problem is derived. The objective function to be minimised is chosen to represent the energy consumption of the propeller over the entire mission, since reduction in total energy consumption on electric aircraft by energy harvesting is the main motivation behind this project. The objective function is therefore represented by the sum of the energy consumed in the climb, cruise and descent phases. During descent, energy is recuperated and it will therefore attain a negative value. When the propeller operates in propulsive mode during climb and cruise, the energy provided by the shaft to the propeller is the product of the shaft power and the time t, as given by equation 4.2. The propulsive efficiency of the propeller η_p is given by equation 4.3 as the ratio between the product of thrust and velocity, representing the useful output power, and the total shaft input power.

$$E_{sh} = P_{sh} \cdot t \tag{4.2}$$

$$\eta_p = \frac{TV}{P_{sh}} \tag{4.3}$$

Substituting equation 4.3 into equation 4.2 for the shaft power, the energy consumed in propulsive mode is given by equation 4.4, where d is the distance covered in flight direction.

$$E_{sh} = \frac{T \cdot V \cdot t}{\eta_p} = \frac{T \cdot d}{\eta_p} \tag{4.4}$$

When the propeller operates in regenerative mode during descent, the energy delivered to the shaft by the propeller is the product of the power delivered to the shaft and the time t. For the windmilling case, the regenerative efficiency, in this case represented by the power coefficient K_P, is given by equation 4.5 as the ratio between the useful energy delivered to the shaft by the propeller and the total input power contained in the incoming wind streamtube, P_w. The latter is given in equation 4.6, where R represents the propeller radius and V the descent velocity of the aircraft.

$$\eta_w = K_P = \frac{P_{sh}}{P_w} \tag{4.5}$$

$$P_w = \frac{1}{2}\rho\pi R^2 V^3 \tag{4.6}$$

For the regenerative propeller, the energy recuperated is therefore given by equation

$$E_{sh} = P_{sh} \cdot t = \eta_w \cdot P_w \cdot t \tag{4.7}$$

Therefore, the total energy consumption of the aircraft over its mission is given by equation 4.8

$$E_{tot} = E_{cl} + E_{cr} + E_w = \frac{T_{cl} \cdot d_{cl}}{\eta_{cl}} + \frac{T_{cr} \cdot d_{cr}}{\eta_{cr}} + \eta_w \cdot P_w \cdot t_w \tag{4.8}$$

The thrust and efficiency values for climb and cruise in equation 4.8 are calculated using equations 2.56 and 2.58 respectively. The regenerative efficiency η_w is given by equation 2.59.

4.3. CONSTRAINTS

The propeller design is performed under a predefined set of constraints in order to ensure that the design variables are not assigned arbitrary values, but instead meet certain requirements in order to result in functional designs. The constraints therefore limit the design space of the optimisation problem. In this section, all the proposed constraints are discussed and motivated. First of all, the thrust constraints for climb and cruise are computed using known aircraft design parameters, flight mechanics, and estimation methods for the Oswald efficiency factor and for the aircraft climb and cruise drag. The latter is needed to calculate the induced drag coefficient, which eventually forms part of the total drag coefficient. The remaining constraints the propeller design needs to meet are also discussed.

4.3.1. OSWALD FACTOR ESTIMATION

The Oswald factor can be estimated using equation 4.9, in which e_{theo} and $k_{e,F}$ are given by equations 4.10 and 4.13 respectively [19]. It is used to calculate the zero-lift drag and the induced drag, the sum of which leads to the total drag. The latter can then be related to the required thrust by the flight mechanics relations that hold in the flight condition under consideration. In equations 4.10 - 4.13, λ is the wing taper ratio, A is the wing aspect ratio, b is the wingspan, c_r is the wing root chord and d_F is the fuselage width.

$$e = e_{theo} \cdot k_{e,F} \cdot k_{e,D_0} \cdot k_{e,M} \tag{4.9}$$

$$e_{theo} = \frac{1}{1 + f(\lambda)A} \tag{4.10}$$

$$f(\lambda) = 0.0524\lambda^4 - 0.15\lambda^3 + 0.1659\lambda^2 - 0.0706\lambda + 0.0119 \tag{4.11}$$

$$\lambda = \frac{2b}{c_r A} - 1 \tag{4.12}$$

$$k_{e,F} = 1 - 2\left(\frac{d_F}{b}\right)^2 \tag{4.13}$$

The correction factor $k_{e,M}$ is neglected since the flow is assumed to be incompressible. This factor is only relevant for higher Mach numbers. The parameter k_{e,D_0} is estimated to be equal to 0.804 for general aviation aircraft [19].

4.3.2. AIRCRAFT DRAG ESTIMATION

During climb and cruise, it is desired to minimise the amount of energy E consumed for a given flight distance X. Therefore, the ratio between distance and consumed energy must be maximised. This ratio is given by equation 4.14, where it is written as a function of the velocity V by dividing both the numerator and denominator by time t. The energy consumption rate of electric aircraft is given by the product of the thrust and the rate of energy consumption per unit of thrust σ in equation 4.15. The rate of thrust specific energy consumption is assumed to be a constant [20].

$$\left(\frac{d\mathrm{X}}{d\mathrm{E}}\right) = \frac{d\mathrm{X}/d\mathrm{t}}{d\mathrm{E}/d\mathrm{t}} = \frac{V}{d\mathrm{E}/d\mathrm{t}} \tag{4.14}$$

$$\frac{d\mathrm{E}}{d\mathrm{t}} = \sigma T \tag{4.15}$$

Substituting equation 4.15 into equation 4.14 and rewriting using the necessary flight mechanics relations in cruise, further elaborated on in section 4.3.4, equation 4.14 can be further derived as performed in equation 4.16.

$$\left(\frac{V}{\sigma T}\right) = \frac{\sqrt{\frac{W}{S}\frac{2}{\rho}\frac{1}{C_L}}}{\sigma T} = \frac{\sqrt{\frac{W}{S}\frac{2}{\rho}\frac{1}{C_L}}}{\sigma \frac{T}{D}\frac{D}{L}\frac{L}{W}W} = \frac{\sqrt{\frac{W}{S}\frac{2}{\rho}\frac{1}{C_L}}}{\sigma \frac{C_D}{C_L}W} = \frac{\sqrt{\frac{W}{S}\frac{2}{\rho}}}{\sigma W}\frac{\sqrt{C_L}}{C_D} \propto \frac{\sqrt{C_L}}{C_D} \tag{4.16}$$

It is therefore desired to maximise the ratio of $\sqrt{C_L}/C_D$ and to achieve this, the derivative of this ratio is set to zero as can be seen in equation 4.17.

$$\left(\frac{\sqrt{C_L}}{C_D}\right)_{max} \rightarrow \frac{d}{dC_L}\left(\frac{\sqrt{C_L}}{C_D}\right) = 0 \tag{4.17}$$

By substituting equation 4.19 into equation 4.17, the relation between the zero-lift drag coefficient C_{D_0} and the lift coefficient C_L is then obtained and given by equation 4.18, where A is the wing aspect ratio.

$$C_{D_0} = \frac{3C_L^2}{\pi A e} \tag{4.18}$$

The drag coefficient can subsequently be calculated using equation 4.19 and the drag then follows from equation 4.20.

$$C_D = C_{D_0} + \frac{C_L^2}{\pi A e} \tag{4.19}$$

$$D = C_D \frac{1}{2}\rho V^2 S \tag{4.20}$$

Using equations 4.18, 4.19 and 4.20, the drag D can be calculated for a given lift coefficient C_L and Oswald factor e. The zero-lift drag coefficient is assumed to be the same for both climb and cruise, since the flaps are retracted to 0° in both cases [21].

4.3.3. CLIMB THRUST CONSTRAINT

In steady, symmetric, climbing flight, as shown in figure 4.3 equations 4.21 and 4.22 hold for the required lift and thrust respectively. The climb angle γ can be calculated from trigonometry and is given by equation 4.23.

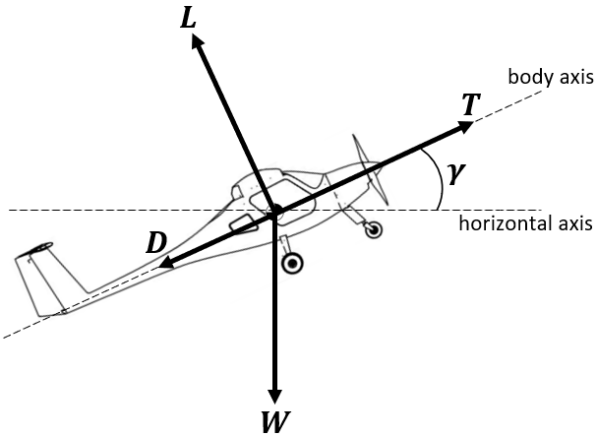

Figure 4.3: Forces in climbing flight

$$L = W\cos\gamma \tag{4.21}$$

$$T = D + W\sin\gamma \tag{4.22}$$

$$\sin\gamma = \frac{RC}{V} \tag{4.23}$$

Therefore, the required climb lift coefficient is given by equation 4.24.

$$C_L = \frac{L}{\frac{1}{2}\rho V^2 S} = \frac{W\cos\gamma}{\frac{1}{2}\rho V^2 S} \tag{4.24}$$

Using equation 4.19, the climb drag coefficient is calculated by substitution of equation 4.24 for the lift coefficient. Finally, the climb thrust requirement is obtained using equation 4.25 by substitution of equation 4.19 for the drag coefficient, which results in $T_{cl,req}$ = 1200.0 N.

$$T_{cl,req} = D + W\sin\gamma = C_D\frac{1}{2}\rho V^2 S + \frac{W}{V}RC \tag{4.25}$$

The climb thrust constraint is therefore given by equation 4.26.

$$\frac{T_{cl}}{T_{cl,req}} - 1 = 0 \tag{4.26}$$

4.3.4. CRUISE THRUST CONSTRAINT

In cruise as shown in figure 4.4, the following relations hold.

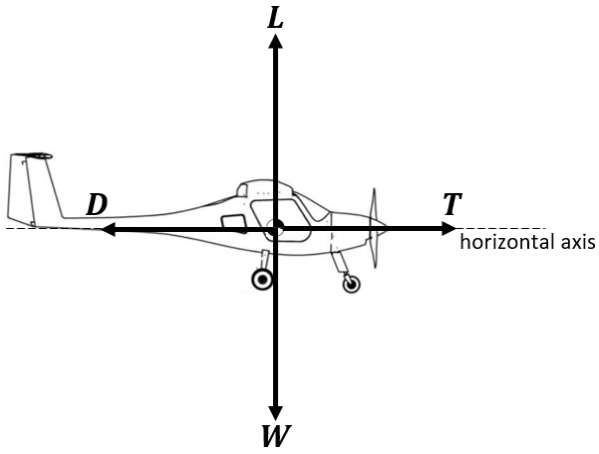

Figure 4.4: Forces in cruise flight

$$T = D \tag{4.27}$$

$$L = W \tag{4.28}$$

Therefore, the required cruise lift coefficient is given by equation 4.29.

$$C_L = \frac{L}{\frac{1}{2}\rho V^2 S} = \frac{W}{\frac{1}{2}\rho V^2 S} \tag{4.29}$$

The thrust required for cruise is obtained using equation 4.30 by substitution of equation 4.19 for the drag coefficient and equation 4.29 for the lift coefficient, which results in $T_{cr,req}$ = 396.0 N.

$$T_{cr,req} = D = C_D\frac{1}{2}\rho V^2 S \tag{4.30}$$

The cruise thrust constraint can therefore be written as in equation 4.31.

$$\frac{T_{cr}}{T_{cr,req}} - 1 = 0 \tag{4.31}$$

4.3.5. RATE OF DESCENT CONSTRAINT

In regenerative descent flight, the clean aircraft drag corresponds to a sink rate of 2.2m/s and with recuperation, the sink rate becomes 3.25m/s [18]. The former can be related to the aircraft drag and the latter to the aircraft drag plus windmilling propeller drag. This can be used to relate the generated descent thrust to the rate of descent. Figure 4.5 shows the forces on the aircraft in descending regenerative flight, that is, negative thrust in the form of windmilling propeller drag D_p is present next to the aircraft drag D_{ac}.

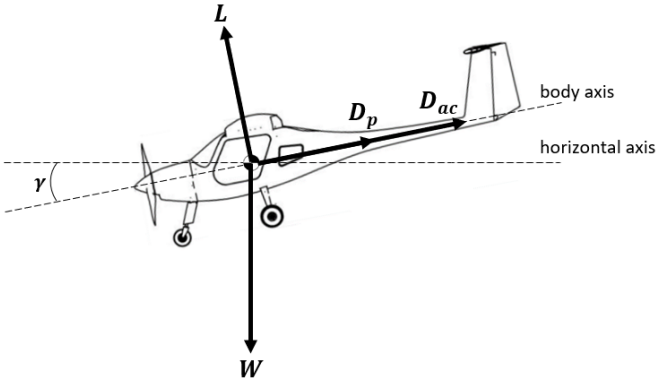

Figure 4.5: Forces in descending flight

Equations 4.32 and 4.33 represent the force equilibrium and rate of descent RD of an aircraft in regenerative descending flight. The total drag of the aircraft is the sum of the aircraft drag D_{ac} and the negative thrust generated by the windmilling propeller, which is equivalent to the windmilling propeller drag D_p. The rate of descent can then be written as a function of the descent velocity V, the total drag and the aircraft weight.

$$D_{ac} + D_p - W\sin\gamma = 0 \tag{4.32}$$

$$RD = V\sin\gamma = V\frac{D_{ac} + D_p}{W} \tag{4.33}$$

From equation 4.33, equations 4.34 and 4.35 are derived, relating the total drag and rate of descent without and with energy recuperation respectively.

$$D_{ac} + D_{p_0} = \frac{W \cdot RD_0}{V} \tag{4.34}$$

$$D_{ac} + D_{p_{reg}} = \frac{W \cdot RD_{reg}}{V} \tag{4.35}$$

From equations 4.34 and 4.35, the difference between the windmilling drag generated with and without recuperation can be derived, which represents the propeller drag generated due to energy recuperation. This can also be seen as the negative thrust force generated by the propeller. Equation 4.36 is derived from equations 4.34 and 4.35 and relates the negative propeller thrust to the aircraft rate of descent.

$$\Delta D_p = D_{p_{reg}} - D_{p_0} = T_w = -\frac{W}{V}\left(RD_{reg} - RD_0\right) \tag{4.36}$$

Therefore, when the descent rate at zero thrust RD_0 is known, this corresponds to $D_{p_0} = 0$. By substituting the computed windmilling thrust resulting from the propeller analysis, the rate of descent RD_{reg} can be calculated from equation 4.36 for a given aircraft weight W, descent velocity V. For safety and practical reasons, it is preferable that the rate of descent stays within the range given by equation 4.37 [1].

$$3m/s \leq RD_{reg} \leq 5m/s \tag{4.37}$$

4.3.6. POWER CONSTRAINT

In sections 4.3.3 - 4.3.5, the thrust constraints were generated. These represent the minimum required thrust values that have to be met in all flight regimes. The final constraint of the optimisation problem ensures that the shaft power during climb and cruise stays below the maximum motor power available (60 kW), as expressed in equation 4.38.

$$\frac{P_{max}}{P_{sh}} - 1 \geq 0 \tag{4.38}$$

4.3.7. DRAG DIVERGENCE MACH NUMBER CONSTRAINT

A constraint is imposed to ensure that at all times the resultant Mach number seen by any airfoil section along the blade span stays below the critical Mach number. This is important to prevent severe compressibility effects leading to an excessive drag rise beyond the drag divergence Mach number [22]. To estimate the drag divergence Mach number, the Korn equation is used and given by equation 4.39. In this equation, C_L is the local lift coefficient generated by the airfoil, t/c is the local thickness-to-chord ratio and κ is the airfoil technology factor which is set equal to 0.87 for NACA airfoil series [22].

$$M_{DD} = \kappa - \frac{C_L}{10} - \frac{t}{c} \tag{4.39}$$

The Mach drag divergence constraint is formulated in equation 4.40, where the local resultant velocity at a blade element U_0 follows from equation 2.38 and a is the speed of sound.

$$M_{DD} - \frac{U_0}{a} \geq 0 \tag{4.40}$$

4.3.8. CHORD AND TWIST DISTRIBUTIONS CONSTRAINTS

A constraint for the blade chord distribution is introduced to avoid unrealistic blade shape designs having structural disadvantages. It is formulated in equation 4.41 and ensures that the tip chord length value c_4 is lower than the chord length value attained at the location of the previous control point, c_3. Similarly, the twist distribution is constrained by equation 4.42. This constraint prevents an overshoot in the twist distribution interpolation near the blade tip and ensures the desired decreasing twist distribution from root to tip for the optimised propeller blade.

$$\frac{c_3}{c_4} - 1 > 0 \tag{4.41}$$

$$\frac{\beta_3}{\beta_4} - 1 > 0 \tag{4.42}$$

4.3.9. LIFT COEFFICIENT AND ANGLE OF ATTACK CONSTRAINTS

Lift coefficient constraints are introduced to ensure that the lift coefficients generated by the airfoils at all blade sections are positive in propulsive mode and negative in regenerative mode. Furthermore, imposing these constraints decreases the design space within the optimisation, which decreases runtime. The constraint for the allowed range of angle of attack is given by equation 4.45. Results corresponding to angles of attack outside of this range lose their reliability since the airfoil database needs to be extrapolated and the airfoil would most likely be operating in highly nonlinear post-stall conditions, where XFOIL results would also become unreliable.

$$C_{L_p} > 0 \tag{4.43}$$

$$C_{L_w} < 0 \tag{4.44}$$

$$-20^\circ \leq \alpha \leq 20^\circ \tag{4.45}$$

4.4. DESIGN VARIABLES

The design variables to be used in an aerodynamic propeller optimisation problem can be divided into three categories: the general, blade and cross-sectional design variables [23]. The general variables are related to the flight conditions and the overall configuration of the propeller. For this research, the radius, cruise rotational velocity and descent rotational velocity are considered to be the general design variables. The number of blades also belongs to this category, however for this research it is considered as a design sensitivity variable. That is, the optimisation results are generated for all considered number of blades and compared to each other. The blade chord and twist distribution belong to the blade design variables category. The cross-sectional design variables are the selection of airfoil sections used. However, in this research the airfoil distribution is an indirect design variable in the sense that the airfoil selection is performed at each combination of

input design variables the optimiser iterates through. In the sections below, all design variables used within the optimisation problem are discussed.

4.4.1. CHORD DISTRIBUTION

The design variables defining the blade chord distribution are the four horizontally equidistant control points, c_1, c_2, c_3 and c_4, through which a cubic spline is fitted. The first control point c_1 is located at the blade root (r/R = 0.2) and the last control point c_4 at the blade tip (r/R = 1.0), as can be seen in figure 4.6. Each control point has a fixed x-coordinate and a y-coordinate that is varied by the optimiser between predefined bounds, the latter represented by the black lines in figure 4.6. More details on the selection of the upper and lower bound points is given later in section 4.5. The red curve represents an example cubic spline fit through a combination of four control points.

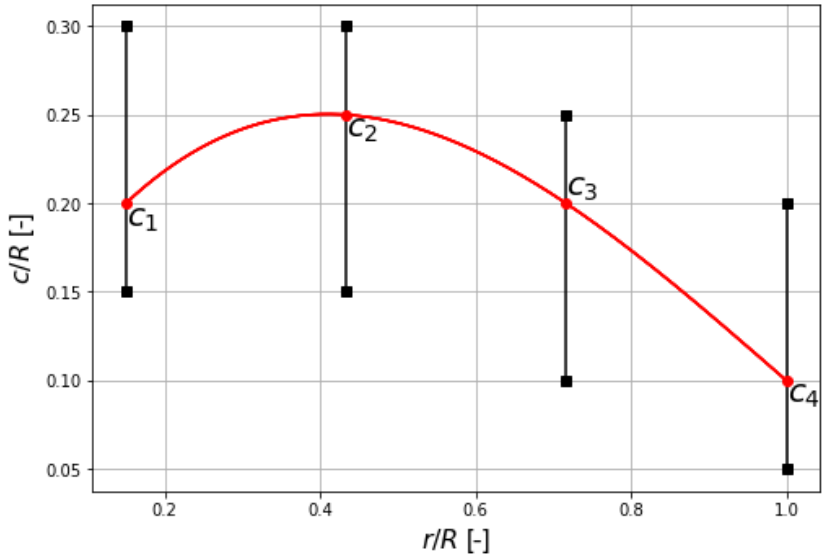

Figure 4.6: Chord distribution by control points

4.4.2. BLADE TWIST DISTRIBUTION AND PITCH SETTINGS

The design variables defining the blade twist distribution are the four horizontally equidistant control points, β_1, β_2, β_3 and β_4, through which a cubic spline is fitted. The first control point β_1 is located at the blade root ($r/R = 0.2$) and the last control point β_4 at the blade tip ($r/R = 1.0$), as can be seen in figure 4.7. Each control point has a fixed x-coordinate and a y-coordinate that is varied by the optimiser between predefined bounds, the latter represented by the black lines in figure 4.7. The red curve represents an example cubic spline fit through a combination of four control points. The blade twist distribution in figure 4.7 must be interpreted as the angle between the chord line of the section at $r/R = 0.2$ and the rotational plane being equal to β_1. Depending on the flight condition, the blade is pitched up by an angle with respect to the twist angle distribution in figure 4.7. These pitch angle settings are represented by β_{cl}, β_{cr} and β_w for the climb, cruise and descent phases respectively. The total blade angle distribution used in the propeller analysis algorithm is therefore obtained by shifting up the twist distribution in figure 4.7 by the pitch angle setting at the flight phase under consideration.

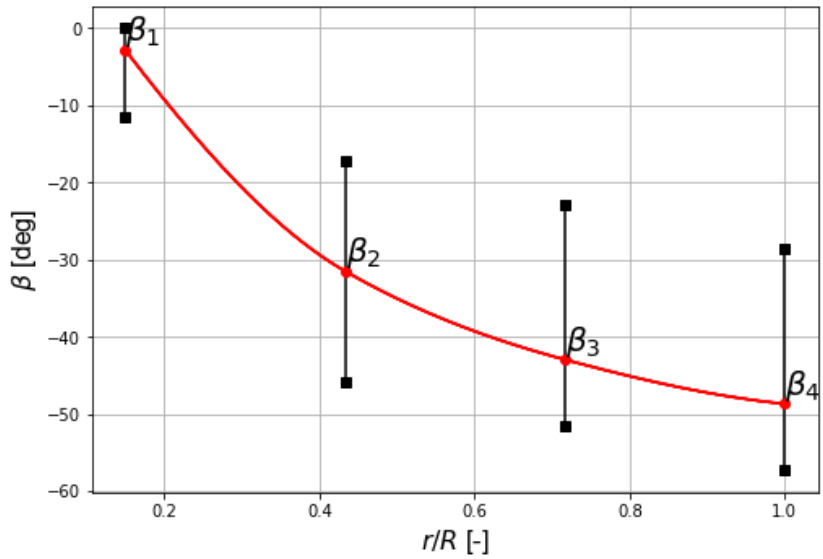

Figure 4.7: Twist distribution by control points

4.4.3. PROPELLER RADIUS AND ROTATIONAL VELOCITY

The propeller radius R is also considered as a design variable in the optimisation problem. Furthermore, the propeller rotational velocities for climb, cruise and descent, Ω_{cl}, Ω_{cr} and Ω_w respectively, are set as design variables. However, since three optimisation cases with respect to propeller pitch and RPM are studied in this research project, one or more of the rotational velocities are set as constant for some of these cases as will become clear at a later stage.

4.4.4. DESCENT VELOCITY

The last design variable considered in the optimisation problem is the descent velocity V_w. As became clear from section 4.3.5, the rate of descent follows from the descent velocity and the time to descend t_w in turn follows from the rate of descent and the known cruise altitude h_{cr}. The descent time is required for the calculation of the objective function in equation 4.8.

4.5. BOUNDS ON DESIGN VARIABLES

All design variables within the optimisation problem must lie within predefined upper and lower bounds. The reason for this is to prevent the variables to attain unrealistic values during the optimisation. Starting with the chord distribution control points, c_1 - c_4, the selected upper and lower bounds mainly ensure structural feasibility of the blade shape. For this, generally at the root larger chord values are seen than at the tip. This implies that the ranges of allowed chord values should decrease towards the tip. The upper bounds on the chord values in the blade root region are mainly to account for hub integration and to ensure staying within a realistic shape design. Too large bounds would also increase the design space, which increases the optimisation run time significantly. The bounds on the twist control points β_1 - β_4 are based on estimations of the inflow angle ϕ on various radial positions, which can be calculated using equation 2.42 using the approximately known propeller operational conditions in all flight phases. The result is shown in figure 4.8, where the inflow angle distribution approximations are plotted for all upper and lower bound values of the propeller rotational velocity in all flight phases. At the stage of defining the optimisation problem, the blade induced velocities are not yet known and therefore, the obtained inflow angle distributions are approximations. It is known from equation 2.41 that the blade angle differs from the inflow angle by the angle of attack. Generally, the angle of attack is relatively small and therefore, by observation of the approximate inflow angle distributions in figure 4.8 and accounting for an offset by a small angle of attack, realistic bounds can be estimated for β_1 - β_4 and for the pitch settings in all flight conditions. The bounds on the pitch angle settings in all flight conditions, β_{cl}. β_{cr} and β_w are all set within 0.8 and 1.3 radians (corresponding to approximately 46 and 74 degrees respectively). This implies that the twist distribution curve as in the example shown in figure 4.7 would be shifted up by a separate value between 0.8 and 1.3 radians for each flight condition, resulting

in the blade angle distribution. Moreover, the defined upper and lower bounds for the twist distribution as illustrated in figure 4.7 follow a similar trend as the inflow velocity distribution approximations in figure 4.8. For the sake of comparison, the actual inflow distribution of the reference propeller geometry used for the validation purpose in this project is also plotted in figure 4.8. This inflow distribution can also clearly be reconstructed within the earlier defined upper and lower bounds of the twist distribution and pitch settings.

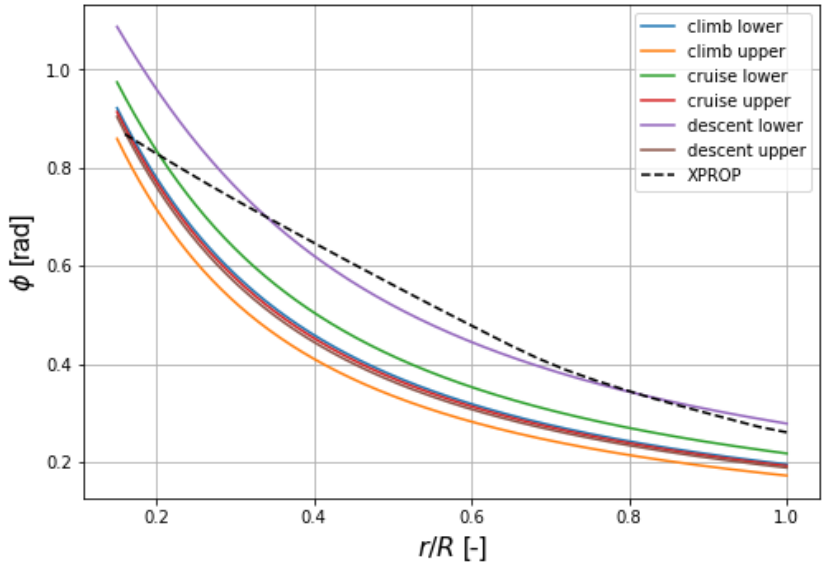

Figure 4.8: Inflow angle distribution approximation

The selected upper bound value for the propeller radius R prevents the tip Mach numbers from becoming too large and ensures sufficient ground clearance. Large tip Mach numbers would result in undesired compressibility effects leading to a rise in drag and a decreased reliability on the aerodynamic data as obtained by XFOIL. The propeller radius is allowed to lie between $R = 0.7$ m and $R = 0.9$ m. The currently used energy harvesting propeller on the Pipistrel Alpha Electro has a radius of $R = 0.82$ [18]. This motivates the selection of the lower bound of $R = 0.7$ m in order for the radius to stay within realistic values during the optimisation. What's more, a sufficiently high lower bound on the radius positively contributes to an acceptable size of the design space, saving optimisation run time. The upper and lower bounds for the propeller rotational velocities in climb, cruise and descent are defined based on (relative) values found for them in literature for a regenerative flight mission. The climb RPM of the reference aircraft is known from [18] to be equal to $RPM_{cl} = 2250$, the cruise RPM is generally similar and the descent RPM is typically approximately a little bit more than half the climb RPM [3]. Based on these findings, realistic lower and upper bounds for both the climb and cruise rotational velocity are defined to be 200 rad/s and 250 rad/s respectively. For energy harvesting, the descent rotational velocity lower and upper bounds are 100 rad/s and 150 rad/s respectively. Realistic lower and upper bounds for the descent velocity V_w follow from the observations made in [1] regarding the descent performance of the Pipistrel Alpha Electro aircraft. Although higher descent velocities result in higher energy recuperation up to a descent velocity of 70 kts for the Pipistrel Alpha Electro aircraft, for safety reasons descent velocities in the range 50-70 kts are generally considered most practical and a low velocity value within this range is preferable [1]. Therefore, the selected lower and upper bounds for the descent velocity become $V_w = 25$ m/s and $V_w = 36$ m/s respectively.

4.6. AIRFOIL SELECTION AND AERODYNAMIC DATABASE

For the propeller analysis as part of the optimisation procedure, the propeller blade is divided into N sections, each assumed to have a constant chord and airfoil geometry. From an aerodynamic perspective, ideally the airfoil with the best compromised L/D performance in the climb, cruise and descent flight conditions should be selected for each blade element. However, in the scope of this project, a single airfoil is selected to be used over the entire blade span. One reason for this is to significantly reduce the optimisation run times. What's more, the main focus of this project is to compare the energy performance of a variable pitch and RPM propeller including energy harvesting to the most currently used constant pitch propeller for this purpose. The

use of more than one airfoil along the span is not expected to significantly contribute to this energy performance comparison, since the use of multiple airfoils would most likely improve the energy performance for all considered optimisation cases in the same order of magnitude.

In order to properly perform an airfoil selection, several airfoils are analysed with respect to their L/D performance over a wide range of positive and negative angles of attack the propeller blade sections are expected to be exposed to during the mission. For this, the L/D is plotted versus α for several airfoils at representative estimations of the Reynolds and Mach numbers along the blade span. The computation of the aerodynamic coefficients of the airfoils is performed using the airfoil analysis program XFOIL. The choice for using XFOIL is made since the author is familiar with its capabilities, and it is a widely used and open source airfoil analysis software including clear documentation [24]. For all considered airfoils in the aerodynamic analysis, the propulsive and regenerative L/D performances are compared and the final selection is based on an estimated best performance compromise in propulsive and regenerative modes.

For the selection of an airfoil family to include in the L/D analysis, some important criteria that the airfoil family has to meet are considered. These are:

- High positive L/D ratio over a wide range of angle of attack in propulsive mode
- Low negative L/D ratio over a wide range of angle of attack in regenerative mode
- Thickness-to-chord ratio between 10% and 20%
- Good low and high speed performance
- Benign stall characteristics

In the optimisation algorithm, lift coefficient constraints ensure that all blade sections operate at positive C_L in propulsive mode and at negative C_L in regenerative mode. Therefore, it is important the the airfoil family contains sections with good overall L/D performance over a broad range of angle of attack in both operational modes. That is, high positive L/D vales are desired in propulsive mode and low negative L/D values in regenerative mode. Regarding the airfoil thickness criteria, it is known that the aerodynamic calculations performed by XFOIL do not tend to converge properly when using relatively thin or thick airfoils, especially at high angles of attack or negative angles of attack for cambered airfoils [24]. Therefore, the allowed thickness-to-chord ratio is chosen to lie within an intermediate range of $0.1 \leq t/c \leq 0.2$. Generally, general aviation propellers attain airfoil thicknesses within this range over the majority of the blade span and in the tip region, the thickness-to-chord ratio is usually lower than 0.1 [25]. However, lower propeller tip velocities are expected for the Pipistrel Alpha Electro aircraft as compared to a conventional general aviation aircraft such as the Pipistrel Alpha Trainer, where the RPM is significantly higher. The use of thin airfoil sections at a propeller blade tip is generally beneficial for higher velocities and therefore, this also justifies the use of airfoils with a thickness above $t/c = 0.1$ everywhere for the Pipistrel Alpha Electro propeller design. It is also important that the airfoils selected demonstrate good lift and drag characteristics at low and high speeds. This is because the local airfoil sections along a propeller blade span operate at a wide range of Mach and Reynolds numbers and the resultant velocities encountered can therefore vary substantially from root to tip. What's more, the induced velocities the blade sections are exposed to are unknown beforehand. Therefore, it is very hard to determine the exact range of Mach and Reynolds numbers beforehand and consequently, it is a good idea to select airfoils that are known to show good lift and drag characteristics at a wide range of velocities. Furthermore, it is beneficial to select airfoils with benign stall characteristics. This will ensure a smooth drop in the lift coefficient at higher angles of attack to which in particular the propeller blade root sections are likely to be exposed. What's more, the aerodynamic data predicted by XFOIL is likely to be more accurate in post-stall conditions for airfoils that show benign stall characteristics [24].

In most modern propeller designs, for structural and aerodynamic reasons typically several distinct airfoils are used along the blade span [26]. From root to tip generally the thickness of the airfoil sections decreases. From a structural point of view this is beneficial in terms of strength and stiffness, and from an aerodynamic point of view, the advantage of thin airfoil sections at the blade tip is their higher critical Mach number. This reduces compressibility drag as a result of higher velocities seen at the blade tip with respect to the root. However, a compromise needs to be found here in this case as the airfoil is constant over the entire blade span for the scope of this project. A family of airfoils that complies very well with the criteria listed above is the 4-digit NACA airfoil series [26]. The four digits represent the airfoil geometrical characteristics, the first digit representing the maximum airfoil camber, the second one the location of maximum camber

and the last two ones the airfoil thickness. All represented geometrical values are normilised with the airfoil chord length [27]. The NACA 44xx family of airfoils are known for their relatively high maximum lift coefficients and benign stall characteristics. For these reasons, they have been used in propeller blade designs before [26]. In this project, a dual-role propeller is designed that is expected to provide sufficient thrust for the climb and cruise phases, however, it should also be capable of recuperating energy in the descent phase. During the latter, negative angles of attack are encountered on the airfoil sections along the blade span and therefore, high positive camber is not beneficial. For this reason, the NACA 24xx and symmetrical NACA airfoil sections are also considered in the L/D analysis. It then remains to determine to what order of magnitude a loss in propulsive performance and a gain in regenerative performance are seen as camber decreases and to perform the final airfoil selection based on these observations.

As mentioned before, it is important to start the L/D analysis of the airfoils by estimating the ranges of Mach number, Reynolds number and angle of attack the airfoils are expected to be exposed to at several radial positions along the blade span during the mission. Equation 4.46 is used to obtain a good estimate of the distribution of the local resultant velocities U_0 seen by the blade sections along the span, composed of the forward flight velocity vector V and the rotational velocity vector Ωr. For present purposes, the axial and tangential induced velocities are not taken into account, since these are not yet known at this point. The Mach and Reynolds number distributions then follow from equations 4.47 and 4.48. The range of angles of attack is set to $-20° \leq \alpha \leq 20°$, since values outside this range lead to unreliable lift and drag results as predicted by XFOIL.

$$U_0 = \sqrt{V^2 + (\Omega r)^2} \qquad (4.46) \qquad M = \frac{U_0}{a} \qquad (4.47) \qquad Re = \frac{\rho U_0 c}{\mu} \qquad (4.48)$$

The lift-to-drag ratio (L/D) of the NACA airfoils shown in table 4.1 have been plotted against the angle of attack from $0° \leq \alpha \leq 20°$ and $-20° \leq \alpha \leq 0°$ to analyse their relative propulsive and regenerative L/D behaviour respectively.

Table 4.1: Airfoil Selection

Symmetrical airfoils	NACA 0012, 0015
2% cambered airfoils	NACA 2412, 2415
4% cambered airfoils	NACA 4412, 4415

As mentioned before, it is important to ensure that all propeller blade sections operate at the maximum achievable lift-to-drag ratio at all times. Given the airfoil, Mach number and Reynolds number, there is a unique value for the angle of attack corresponding to a maximum L/D ratio. From equation 4.46 it is clear that the blade sections near the tip, where r is high, are exposed to higher resultant velocities U_{res} than the root sections. On top of that, the increasing magnitude of the rotational velocity vector towards the blade tip would increase the angle of attack the blade airfoil sections are exposed to from root to tip. For this reason, propeller blades generally tend to be twisted from root to tip, attaining high blade angles at the root and lower blade angles at the tip, with the aim of maintaining the optimum angle of attack for maximum L/D as close as possible everywhere along the blade span. In figures 4.9 - 4.20, the lift-to-drag ratio L/D is plotted against the angle of attack α in propulsive and regenerative modes for the airfoils in table 4.1. It can clearly be seen that the L/D performance is affected by airfoil thickness; the angle of attack for maximum L/D generally increases with thickness. It is clear from figures 4.9 - 4.20 that for low absolute values for the angle of attack, the airfoils with 12% thickness show a better L/D performance, while for intermediate to higher angles of attack, the airfoils with 15% thickness outperform the thinner airfoils both in propulsive and regenerative modes. The effect of camber on the propulsive and regenerative L/D performance is also clear from figures 4.9 - 4.20. In propulsive mode, the highest L/D values correspond to the most cambered airfoils, the NACA 4412 and NACA 4415. The symmetric airfoils, the NACA 0012 and NACA 0015, attain the lowest L/D values over the positive angle of attack range. However, the symmetrical airfoils demonstrate the best L/D performance in regenerative mode at negative angles of attack, while the regenerative performance decreases as camber increases. From a careful observation of figures 4.9 - 4.20, the NACA 4415 airfoil demonstrates a significantly better propulsive L/D performance than the symmetric and the NACA 2412 and NACA 2415 airfoils. Compared to the NACA 4412 airfoil, it can be seen that the NACA 4415 airfoil performs better for intermediate to larger angles of attack, which are expected to be encountered over the majority of the blade span. It is also clear that the NACA 4415 airfoil performs significantly better in regenerative mode with respect to the NACA

4412 airfoil. For these reasons, the NACA 4415 is the final selected airfoil to be used in the propeller optimisation algorithm. It is estimated to demonstrate the best compromised L/D performance over the majority of the considered mission cases, in particular for the ones with larger cruise distances, where the optimisation algorithm will obviously tend to focus more on propulsive performance with respect to energy harvesting performance.

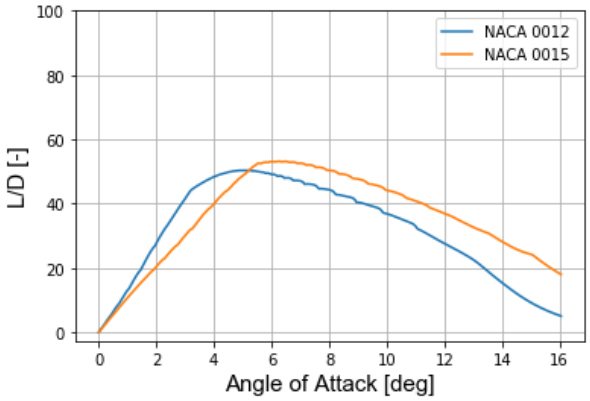

Figure 4.9: NACA 0012 and NACA 0015 propulsive L/D at propeller blade root

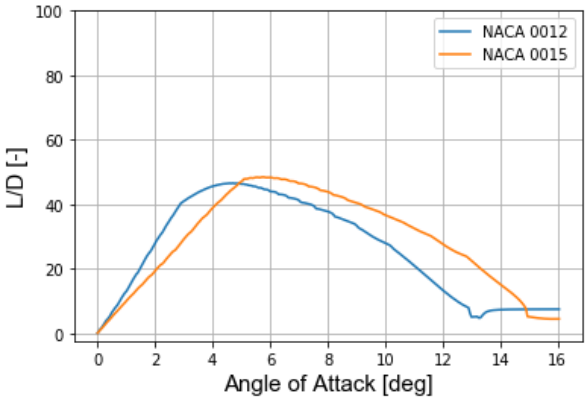

Figure 4.10: NACA 0012 and NACA 0015 propulsive L/D at propeller blade tip

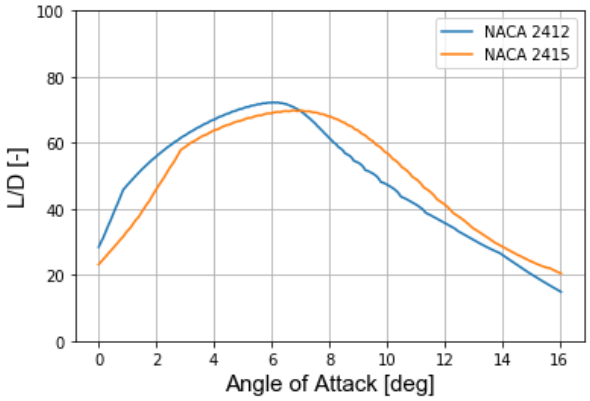

Figure 4.11: NACA 2412 and NACA 2415 propulsive L/D at propeller blade root

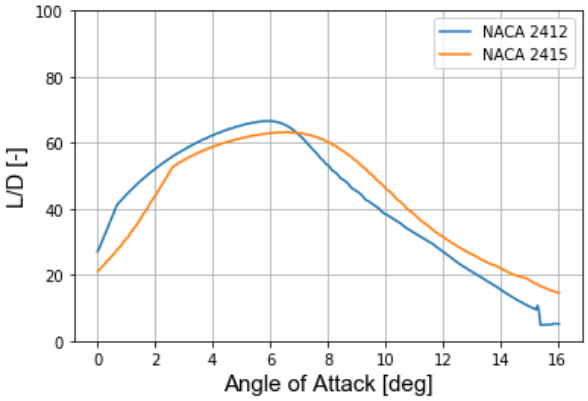

Figure 4.12: NACA 2412 and NACA 2415 propulsive L/D at propeller blade tip

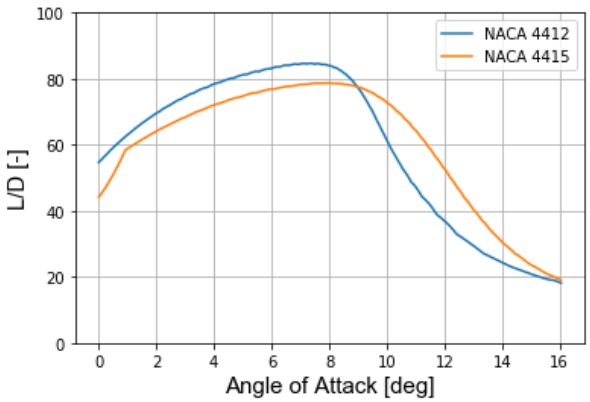

Figure 4.13: NACA 4412 and NACA 4415 propulsive L/D at propeller blade root

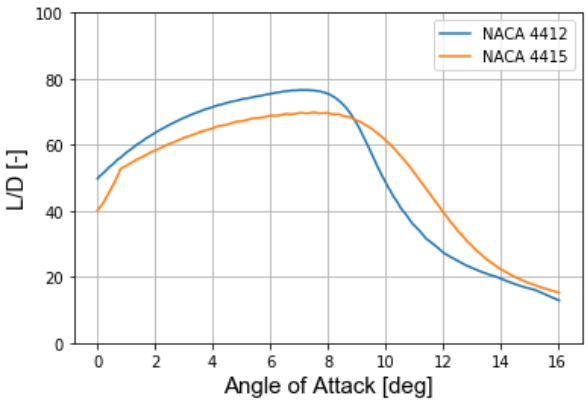

Figure 4.14: NACA 4412 and NACA 4415 propulsive L/D at propeller blade tip

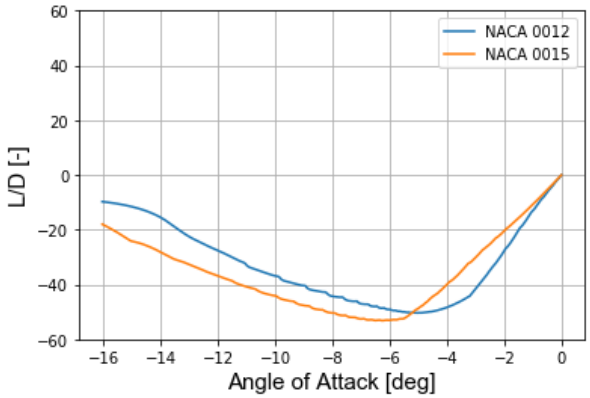

Figure 4.15: NACA 0012 and NACA 0015 regenerative L/D at propeller blade root

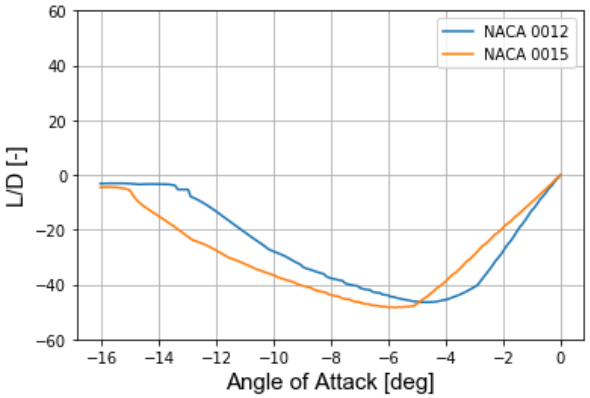

Figure 4.16: NACA 0012 and NACA 0015 regenerative L/D at propeller blade tip

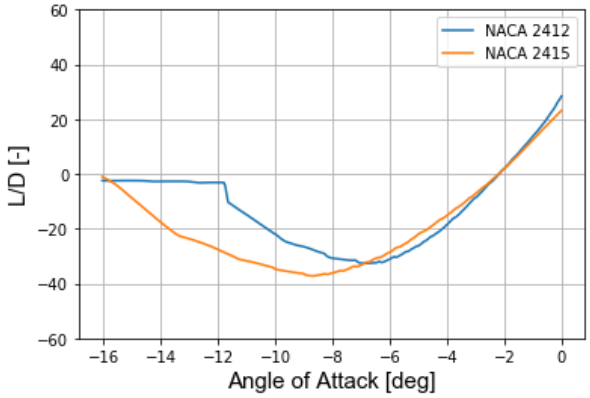

Figure 4.17: NACA 2412 and NACA 2415 regenerative L/D at propeller blade root

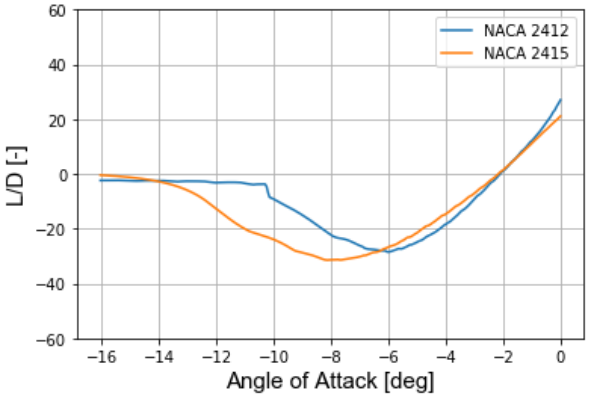

Figure 4.18: NACA 2412 and NACA 2415 regenerative L/D at propeller blade tip

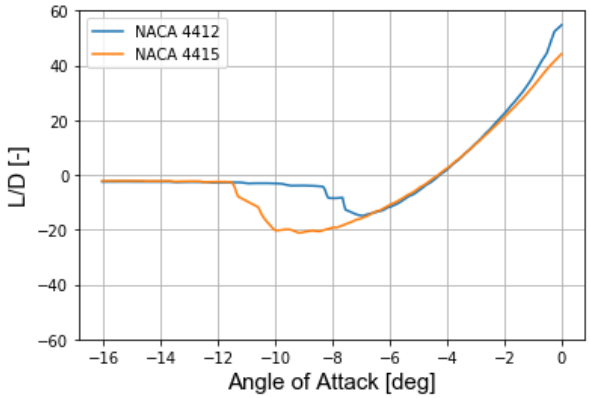

Figure 4.19: NACA 4412 and NACA 4415 regenerative L/D at propeller blade root

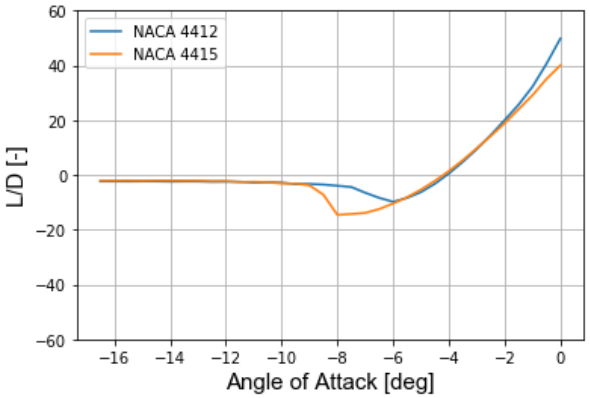

Figure 4.20: NACA 4412 and NACA 4415 regenerative L/D at propeller blade tip

The optimisation algorithm requires the aerodynamic coefficients C_L and C_D of the airfoil used for any input combination of Mach number, Reynolds number and angle of attack. In order to prevent the need of running XFOIL a large amount of times during the optimisation, which would increase the run time significantly, XFOIL is used to create an aerodynamic database for the airfoil as shown in table 4.2 for predefined ranges of Mach number, Reynolds number and angle of attack. With a sufficiently large margin to account

for uncertainties, suitable ranges for the Mach number and Reynolds number are determined using equations 4.47 and 4.48 and the estimated propeller operational conditions during the mission. Two aerodynamic databases that attain the form of table 4.2 are created. One for only the specified range of positive angles of attack and the other for the negative angles of attack. For the database where $\alpha \geq 0$, the Mach number ranges from $M = 0.0$ to $M = 0.6$ with steps of $\Delta M = 0.1$. The Reynolds number varies from $Re = 150,000$ to $Re = 3,000,000$ in steps of $\Delta Re = 285,000$. The angle of attack varies from $\alpha = 0.0°$ to $\alpha = 20.0°$ in steps of $\Delta\alpha = 1.0°$. For the database where $\alpha \leq 0$, the Mach number ranges from $M = 0.0$ to $M = 0.5$ with steps of $\Delta M = 0.1$, the Reynolds number range remains the same and the angle of attack varies from $\alpha = 0.0°$ to $\alpha = -20.0°$ in steps of $\Delta\alpha = -1.0°$. XFOIL is run for all combinations of these Mach numbers, Reynolds numbers and angles of attack to calculate the corresponding lift and drag coefficients of the airfoil, and the results are stored in the aerodynamic database in table 4.2. The resulting aerodynamic database is then read into the optimiser and by three-dimensional linear interpolation, the lift and drag coefficients can be calculated for any local combination of airfoil, Mach number, Reynolds number and angle of attack along the blade span as encountered during the optimisation run.

Table 4.2: Aerodynamic Airfoil Database

Airfoil	Mach	Re	α	C_L	C_D	L/D
⋮	⋮	⋮	⋮	⋮	⋮	⋮

4.7. FORMULATION OF THE OPTIMISATION PROBLEM

At this point, the objective function, constraints and design variables required for the optimisation problem have been discussed. In this section, the optimisation problem is formulated based on these findings. As discussed before, the main proposed objective for the optimisation of the energy-harvesting propeller is to minimise its overall energy consumption E throughout the entire mission, where the total energy is given by equation 4.49.

$$E(\vec{\mathbf{x}}) = \frac{T_{cl} \cdot d_{cl}}{\eta_{cl}} + \frac{T_{cr} \cdot d_{cr}}{\eta_{cr}} + \eta_w \cdot P_w \cdot t_w \tag{4.49}$$

The mathematical formulation of the optimisation problem, including the objective function, constraints, design variables and their corresponding upper and lower bounds, is given by equation 4.50.

$$
\begin{aligned}
\text{minimise} \quad & f(\vec{\mathbf{x}}) = E(\vec{\mathbf{x}}) + p\left[\sum_{i=1}^{5} \min\{0, g_i(\vec{\mathbf{x}})\}^2\right] \\
\text{subject to} \quad & g_1 = \frac{T_{cl}}{T_{cl,req}} - 1 = 0 \\
& g_2 = \frac{T_{cr}}{T_{cr,req}} - 1 = 0 \\
& g_3 = \frac{RD_{reg}}{3} - 1 \geq 0 \\
& g_4 = 1 - \frac{RD_{reg}}{5} \geq 0 \\
& g_5 = \frac{P_{max}}{P_{sh}} - 1 \geq 0 \\
& g_6 = M_{DD} - \frac{U_0}{a} \geq 0 \\
& g_7 = \frac{c_3}{c_4} - 1 > 0 \\
& g_8 = \frac{\beta_3}{\beta_4} - 1 > 0 \\
& g_9 = C_{L_p} > 0 \\
& g_{10} = -C_{L_w} > 0 \\
& g_{11} = 1 - \frac{\alpha}{20^\circ} \geq 0 \\
& g_{12} = 1 + \frac{\alpha}{20^\circ} \geq 0 \\
\text{w.r.t} \quad & \vec{\mathbf{x}} = \left[c_1, c_2, c_3, c_4, \beta_1, \beta_2, \beta_3, \beta_4, \beta_{cl}, \beta_{cr}, \beta_w, R, \Omega_{\text{cl}}, \Omega_{\text{cr}}, \Omega_{\text{w}}, V_w\right] \\
\text{where} \quad & x_i^{min} \leq x_i \leq x_i^{max}; \quad i = 1, 2, ..., 16
\end{aligned}
\tag{4.50}
$$

The objective function $f(\vec{\mathbf{x}})$ of the optimisation problem is a sum of the energy consumption term $E(\vec{\mathbf{x}})$ and a penalty function term which ensures that the objective function value is increased significantly in case one or more of the constraints g_i are violated. This is done by setting the penalty constant p to a large value. The energy consumption $E(\vec{\mathbf{x}})$ itself depends on a number of design variables represented as a design vector $\vec{\mathbf{x}}$. The desired optimisation outcome is a design vector $\vec{\mathbf{x}}$ resulting in minimum energy consumption for a given number of blades and cruise distance. Combinations of the latter two are used to study their influence on the final optimisation results, and are therefore not considered as direct design variables in the optimisation problem, but merely as optimisation sensitivity parameters. The objective function is subject to twelve constraints, the purposes of which were clearly outlined in section 4.3. Every design variable x_i is required to attain a value between predefined bounds, x_i^{min} and x_i^{max}. The bounds on the design variables and the thrust constraints set the optimisation design space.

As mentioned before, the three optimisation cases listed below are considered in this project, which are related to the type of propeller operation with respect to propeller pitch and RPM.

- Case 1: Constant pitch, variable RPM (CPVR)
- Case 2: Variable pitch, constant RPM during climb and cruise, variable RPM during descent (VPCR)
- Case 3: Variable pitch, variable RPM (VPVR)

In the first case, the propeller pitch is set to one constant value throughout the entire mission but the RPM is allowed to vary between all flight phases. This implies that β_{cl}, β_{cr} and β_w in equation 4.50 are replaced by a single pitch setting β to be considered as a design variable instead. In the second case, the pitch is allowed to vary between the flight phases and the RPM attains a single constant value during both climb and cruise flight, however it is still considered a design variable for the descent phase. In this case, the RPM is set to a

constant value of $\Omega_{cl} = \Omega_{cr} = 2250$ rev/min for climb and cruise, which can be found in [18] for the Pipistrel Alpha Electro aircraft, and Ω_w remains a design variable. Finally, for case 3, the blade pitch and RPM are both allowed to vary between all flight phases. This is the most interesting case considered in this project, in the sense that all design variables as shown in 4.50 are optimised for at the same time and the energy performance compared to the other cases, CPVR being the currently applied case for energy harvesting electric aircraft as became clear earlier, can be studied. All optimisations within this project are performed for both two and three propeller blades.

4.8. SELECTION OF AN OPTIMISATION METHOD

The formulated optimisation problem in equation 4.50 can be classified as a single-objective, multivariate, nonlinear, constrained optimisation problem for which a global minimum is desired to be found. In this section, a suitable optimisation method is selected to solve the defined optimisation problem. A general overview of available engineering optimisation methods is given in [28]. A large selection of aerodynamic optimisation techniques is discussed in [29]. An extensive overview of the development of different optimisation methods specifically for different propeller optimisation problems is provided in [30]. The objective and constraint functions of the optimisation problem described by 4.50 are highly nonlinear with unreliable and undefined derivatives. Furthermore, the objective function is multimodal and cannot be written in closed form as a function of all the design variables. The multimodal character of the objective function becomes clear after several optimisation runs, where it is seen that different combinations of design variables are capable of meeting the imposed constraints, resulting in many local minima. For obtaining a global optimum to an optimisation problem with these characteristics, genetic optimisation algorithms are most commonly used [30]. These algorithms fall into the category of modern optimisation methods [28]. Genetic optimisation algorithms are stochastic and global in nature, effectively searching over the entire design space, operating based on the evolutionary principles of natural selection, including mutation, recombination and selection. The input to the algorithm is a population of design vectors in the design space that undergo the processes of mutation, recombination and selection based on their fitness values, being the objective function values. The mutation operation prevents the algorithm to get trapped in local optima. Infeasible solutions are penalised to ensure that their fitness values are worse than for the feasible solutions. The selected best vectors, using the aerodynamic solver, make it to the subsequent improved generation of design vectors and the worse vectors are discarded, while the population size remains constant. This process repeats itself until the fitness variation within the generation reaches a termination criterion, which ends the optimisation. Genetic algorithms only use objective function values and therefore do not need local gradient information for the search. This also contributes in decreasing the probability of the algorithm to converge to a local optimum. For an optimisation of a multimodal objective function, the use of gradient information increases the probability that the algorithm will converge to a local optimum without any further search within the design space. The absence of using function derivative information avoids this, and makes genetic algorithms more appropriate and applicable to a large variety of optimisation problem types. Furthermore, genetic algorithms are relatively simple and have successfully been applied to a large range of science and engineering design problems. These characteristics lead to a growing interest in their applications within engineering [29]. Within the existing genetic algorithms, the differential evolution optimisation algorithm is frequently used to solve constrained, multimodal optimization problems [31]. Furthermore, the simplicity, good convergence characteristics and robustness of the differential evolution algorithm makes it a very popular optimisation technique for a wide variety of global optimisation applications [32]. Based on these considerations, the differential evolution optimisation algorithm is selected to perform the dual-role propeller optimisation.

4.9. PROPELLER OPTIMISATION BY DIFFERENTIAL EVOLUTION

In this section, the application of the differential evolution global optimisation algorithm used for the propeller optimisation is explained. At this point, the method of obtaining the objective function value from a given design vector $\vec{x}$ has been established. In this section, the general working principles of the differential evolution optimisation algorithm are explained and applied to the propeller optimisation problem. The aim of the optimisation algorithm is to find a design vector that minimises the objective function value and meets the constraints. The differential evolution optimisation algorithm is applied to the propeller optimisation problem. A flowchart illustrating the steps taken by the optimiser is shown in figure 4.21.

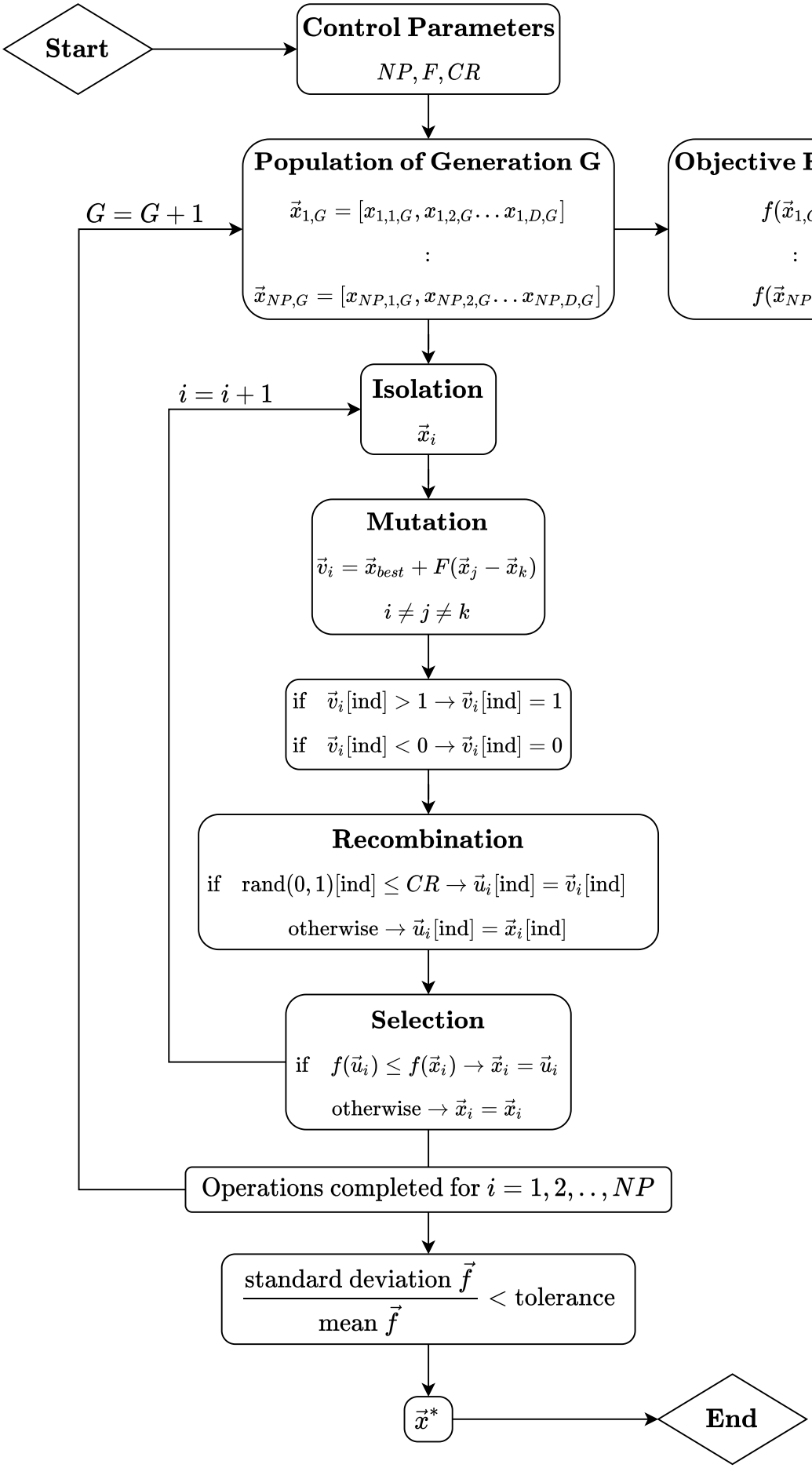

Figure 4.21: Differential evolution algorithm flowchart

There are three optimisation control parameters that have to be specified by the user, which influence the performance of the optimisation algorithm. These are the population size NP, the mutation constant F and the crossover probability CR. By a trial and error process, the population size has been set to 10 times the number of design variables during all optimisation runs, as also suggested in [33]. A too large population size would significantly increase the convergence time. For the mutation constant, dithering is employed so that it attains a randomly chosen value at every new generation, as explained shortly. The input to the optimiser is a set of NP candidate design vectors which represent the first generation G of vectors. For each vector $\vec{x}_{i,G}$ in the generation, the corresponding objective function value $f(\vec{x}_{i,G})$ is computed. Next, one of the vectors $\vec{x}_i$ from the current population is isolated. Corresponding to the isolated vector, a mutation vector $\vec{v}_i$ is created according to equation 4.51, where $\vec{x}_{best}$ is the design vector with the best objective function value in the current generation and $\vec{x}_j$ and $\vec{x}_k$ are randomly chosen distinct vectors from the current generation, both different from the isolated vector $\vec{x}_i$. That is, $\vec{x}_i \neq \vec{x}_j \neq \vec{x}_k$. The mutation constant F is a randomly selected number between 0.5 and 1 and a new random number for F is selected in every new generation. This is known as dithering, which can improve the convergence of the algorithm significantly when compared to the use of only one constant value for F in every generation.

$$\vec{v}_i = \vec{x}_{best} + F(\vec{x}_j - \vec{x}_k) \tag{4.51}$$

Since all design variables in the design vector are normalised, that is, they all attain values between 0 and 1, the mutation operation of equation 4.51 could result in a vector containing indices of design variables attaining values smaller than 0 or larger than 1. In that case, equation 4.52 is applied to ensure the design variables to stay normalised during the optimisation operations applied to them.

$$\vec{v}_i = \begin{cases} \vec{v}_i[\text{ind}] = 1 & \text{if} \quad \vec{v}_i[\text{ind}] > 1 \\ \vec{v}_i[\text{ind}] = 0 & \text{if} \quad \vec{v}_i[\text{ind}] > 0 \end{cases} \tag{4.52}$$

After the computation of the mutant vector $\vec{v}_i$ corresponding to the isolated vector $\vec{x}_i$ from the population, recombination is applied. This operation combines information from the isolated and mutant vectors using equation 4.53. A crossover probability of $CR = 0.7$ is selected and a new trial vector $\vec{u}_i$ is generated where initially every index is a random number between 0 and 1. In this vector, all indices that attain values smaller than CR are replaced by the values at the same index in the mutant vector $\vec{v}_i$ and all indices larger than CR are replaced by the values at the same index in the isolated vector $\vec{x}_i$. After these replacements, the final trial vector $\vec{u}_i$ is generated. The selection of $CR = 0.7$ is based on considerations regarding population stability and convergence speed. A high crossover constant allows a larger number of mutants to proceed to the next generation of design vectors, however at the cost of the population stability and as a result the optimiser is more prone to getting trapped in a local minimum. On the other hand, a low crossover rate will result in better global convergence, however, at the cost of a significant increase in optimisation runtime. The selection of the crossover constant is performed using a trial and error process, as also suggested in [34], by trading off the convergence speed against the estimated accuracy of finding a global minimum after several optimisation runs using several values of the crossover constant.

$$\vec{u}_i[\text{ind}] = \begin{cases} \vec{v}_i[\text{ind}] & \text{if} \quad \text{rand}(0,1)[\text{ind}] \leq CR \\ \vec{x}_i[\text{ind}] & \text{otherwise} \end{cases} \tag{4.53}$$

When the trial vector $\vec{u}_i$ is generated, the objective function value is compared to the objective function value corresponding to the isolated vector $\vec{x}_i$. If the trial vector results in a better objective function value than the isolated vector, the isolated vector in the population is replaced by the trial vector. In case the isolated vector results in a better objective function value than the trial vector, the isolated vector stays in the population. Mathematically, the selection process is given by equation 4.54.

$$\vec{x}_i = \begin{cases} \vec{u}_i & \text{if} \quad f(\vec{u}_i) \leq f(\vec{x}_i) \\ \vec{x}_i & \text{otherwise} \end{cases} \tag{4.54}$$

After selection has taken place, the next vector from the population is isolated and the mutation, recombination and selection operations are performed on it. After all vectors from the population have been isolated followed by mutation, recombination and selection, a new generation of NP design vectors is obtained. This completes one iteration of the differential evolution algorithm. On this new generation of design vectors, all the processes of isolation, mutation, recombination and selection are applied again. Continuing this process

results in increasingly improving generations of design vectors, where the differences between the values attained by the design variables in the design vectors in the population decrease. The optimisation converges when the criterion in equation 4.55 is met. That is, when for a generation the ratio between the standard deviation of the objective function values and the absolute mean objective function value reaches a value below the prescribed termination tolerance. The best design vector of the last generation is then taken as the solution to the optimisation problem.

$$\frac{1}{|\bar{f}|}\sqrt{\sum_{i=1}^{NP}\frac{|f_i-\bar{f}|}{NP}} \leq \text{tolerance} \tag{4.55}$$

5

SINGLE-POINT OPTIMISATION RESULTS

Before performing propeller optimisations for minimum energy consumption over an entire mission including climb, cruise and descent, in this chapter single-point optimisations for the separate flight phases are initially performed. The idea behind this is to obtain the propeller blade geometry that would achieve optimal performance in each separate flight phase and then the changes in geometry required to perform optimally for a complete mission, considering all flight phases at the same time in the optimisation, can be studied.

Having obtained the single-point propeller geometries, these are then operationally optimised for the remaining flight mission to investigate how they perform over the complete mission. The optimisation problem is defined first in section 5.1, after which the propeller blade geometry results are analysed in terms of the chord and blade angle distributions in section 5.2 and the propeller radius in section 5.3 for all considered optimisation cases. Subsequently, these geometry results combined with propeller aerodynamics theory are used to analyse the corresponding propeller performance for all considered cases in the remaining sections of this chapter.

5.1. OPTIMISATION PROBLEM DEFINITION

For each propeller operational case with respect to pitch and RPM settings (CPVR, VPCR and VPVR as clarified in section 4.7), a single-point optimisation is performed for each flight phase separately. That is, for the three operational cases, a single-point optimisation is performed for each term in equation 4.49, and both for a two and three-bladed propeller. The objective function when the propeller is optimised for only the climb phase of the mission is given by equation 5.1. Similarly, the objective function when optimising for cruise is given by equation 5.2 and for descent equation 5.3 is used. For all these separate optimisations, all constraints in the remaining two flight phases are still required to be met.

$$E_{cl}(\vec{\mathbf{x}}) = \frac{T_{cl} \cdot d_{cl}}{\eta_{cl}} \qquad (5.1) \qquad E_{cr}(\vec{\mathbf{x}}) = \frac{T_{cr} \cdot d_{cr}}{\eta_{cr}} \qquad (5.2) \qquad E_{w}(\vec{\mathbf{x}}) = \eta_{w} \cdot P_{w} \cdot t_{w} \qquad (5.3)$$

The objective functions defined by equations 5.1 - 5.3 result in optimised blade geometries for a single point in the flight mission. The resulting blade geometries are then optimised only for their operation on the remaining part of the mission. That is, the pitch and/or RPM settings, depending on the optimisation case considered (CPVR, VPCR or VPVR), are optimised for the remaining two flight conditions. In this way, the performance over an entire mission of a propeller optimised for a single point can be studied and eventually compared to the performance of a propeller that is optimised for all flight phases at the same time for the same mission, as will be done in chapter 6. All single point propeller optimisations and their subsequent optimisations for mission performance are performed for a cruise range of $d_{cr} = 200$ km, since this is approximately the maximum range of the Pipistrel Alpha Electro aircraft and therefore the most interesting for future reference [18].

5.2. CHORD AND BLADE ANGLE DISTRIBUTIONS

In this section, the chord and blade angle distributions of the propellers optimised for climb, cruise and descent are analysed for all optimisation cases and number of blades.

5.2.1. CASE 1: CONSTANT PITCH, VARIABLE RPM

In figure 5.1 and 5.2, the chord distributions for respectively two and three blades are shown for the CPVR optimisation case. These are visualised in figures 5.3 - 5.8. The remaining chord distribution visualisations for the other two cases (VPCR and VPVR) can be found in appendix A. Some interesting observations can be made from these figures. First of all, there is a clear difference in geometry between the descent propeller for energy harvesting and the propulsive climb and cruise propellers. The descent propellers in both cases show a larger solidity in order to maximise the energy harvested at low speed operation as compared to the climb and cruise propellers. The blade sections of the descent propellers are exposed to negative angles of attack at relatively low resultant velocity. Since the section efficiency in many cases rapidly decreases as the angle of attack becomes highly negative, for the descent propellers it becomes more beneficial to increase the chord values for increased L/D performance than to operate at more negative angles of attack with lower chord values. The three-bladed descent propeller has lower chord values than the two-bladed propeller as can be noted from figures 5.1 and 5.2. In order to perform as efficiently as the two-bladed propeller while meeting the same maximum rate of descent as determined by its corresponding constraint, lower chord values are required for the three-bladed propeller. Higher chord values for the three-bladed propeller would lead to inefficient section performance as the section angles of attack would become too low as compared to the angle of attack for maximum negative L/D.

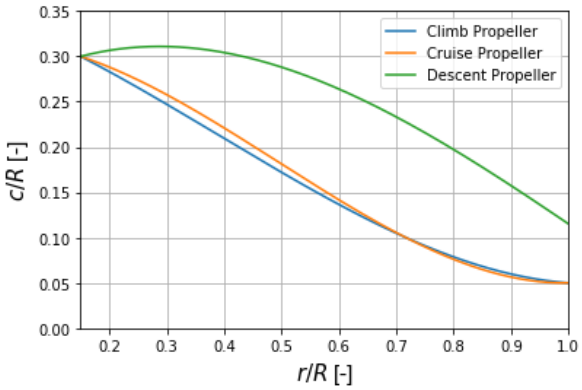

Figure 5.1: Chord distributions for CPVR, B = 2

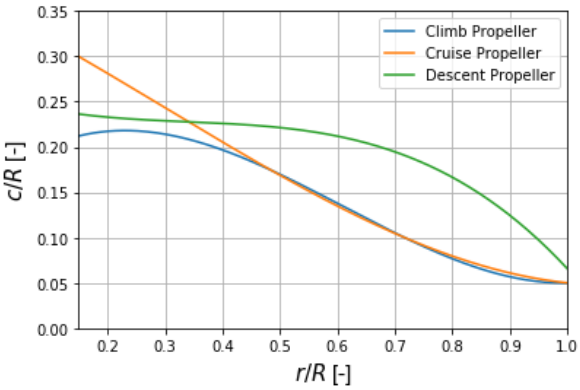

Figure 5.2: Chord distributions for CPVR, B = 2

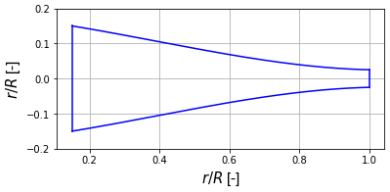

Figure 5.3: CPVR Chord distribution for climb Propeller, B = 2

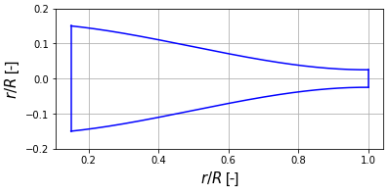

Figure 5.4: CPVR Chord distribution for cruise Propeller, B = 2

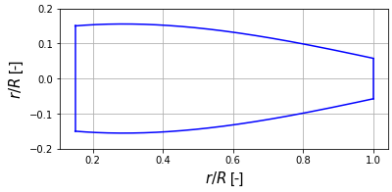

Figure 5.5: CPVR Chord distribution for descent Propeller, B = 2

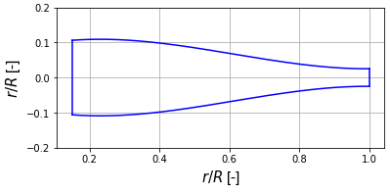

Figure 5.6: CPVR Chord distribution for climb Propeller, B = 3

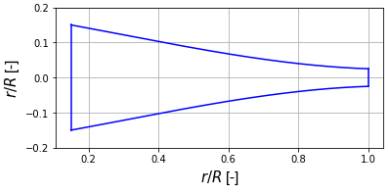

Figure 5.7: CPVR Chord distribution for cruise Propeller, B = 3

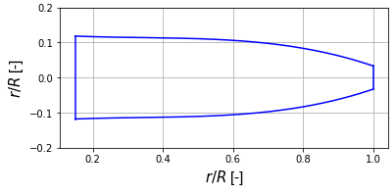

Figure 5.8: CPVR Chord distribution for descent Propeller, B = 3

In figures 5.9 and 5.10, the blade angle distributions corresponding to the chord distributions from figures 5.1 and 5.2 for respectively two and three blades are shown for the CPVR optimisation case. Since the cruise propeller requires significantly less thrust than the climb propeller, the RPM is lower in order to decrease the magnitude of the resultant velocities at the blade sections. Instead, high blade angles are beneficial for cruise since an efficient angle of attack distribution can be attained by a combination of low RPM and high blade angle at the relatively high cruise flight velocity. The blade angle distribution of the climb propeller is slightly lower since for the high thrust required during this flight phase, a high RPM is required. In combination with a lower flight velocity, lower blade angles are required in order to prevent the section angles of attack from increasing beyond efficient operational values. For descent, the lowest blade angles of attack are required since in this flight phase, the blade sections operate at negative angles of attack and lower values of flight velocity and RPM as compared to climb and cruise operation.

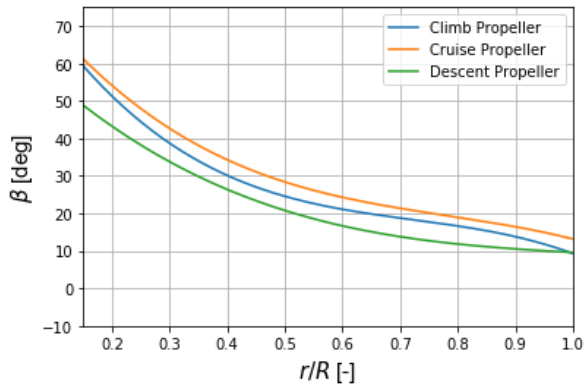

Figure 5.9: Blade angle distributions for CPVR, B = 2

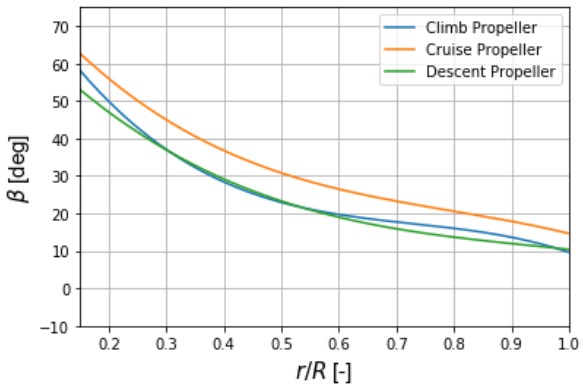

Figure 5.10: Blade angle distributions for CPVR, B = 3

5.2.2. CASE 2: VARIABLE PITCH, CONSTANT RPM

In figure 5.11 and 5.12, the chord distributions for respectively two and three blades are shown for the VPCR optimisation case. Again, a clear difference in geometry between the descent propeller for energy harvesting and the propulsive climb and cruise propellers can be observed. Also, the two-bladed climb and cruise propellers attain practically the same geometry. However, the three-bladed climb propeller has a lower solidity than the three-bladed cruise propeller. The most likely reason for this is that since the radii of the climb propellers stay almost constant, the increase in solidity by more blades is compensated by decreasing the chord values in order to meet the same climb thrust requirement. However, the three-bladed cruise propeller has a smaller radius than the two-bladed one and therefore, the same low thrust requirement is met using a smaller radius in this case.

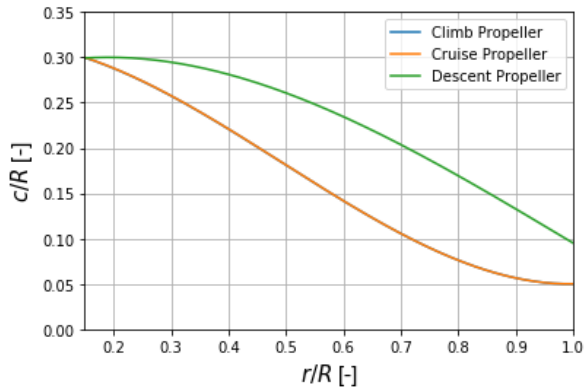

Figure 5.11: Chord distributions for VPCR, B = 2

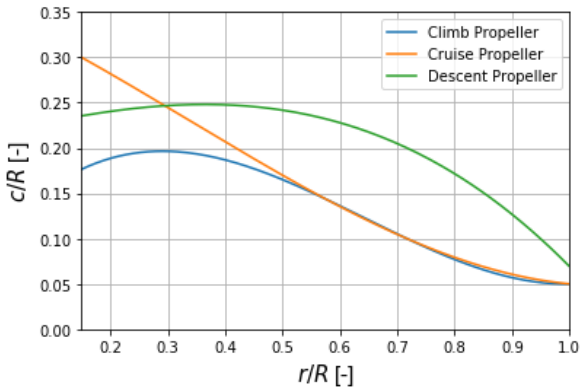

Figure 5.12: Chord distributions for VPCR, B = 3

Since for this optimisation case, and also for the VPVR case as discussed shortly, the pitch is allowed to vary between the flight phases, separate blade angle distributions are attained for each flight phase. In figures 5.13 and 5.14, the blade angle distributions for the climb phase are plotted for two and three blades respectively.

As compared to the CPVR case, the main difference is the higher blade angles for the cruise propellers in both cases. This is a result of the same value of RPM attained in climb and cruise. In order for the cruise propeller with a smaller radius than the climb propeller to be capable to produce sufficient thrust during climb at a fixed RPM the blade angles must be high in order to attain sufficiently large section angles of attack. From the propeller analysis results, it indeed results that for CPVR, the climb RPM of the cruise propeller is higher than the constant value of RPM = 2250 rev/min for climb and cruise in the VPCR case.

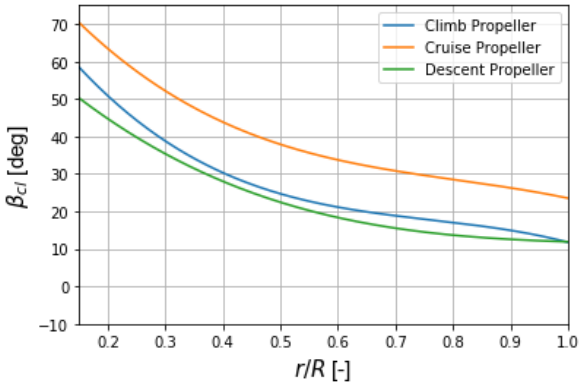

Figure 5.13: Climb blade angle for VPCR, B = 2

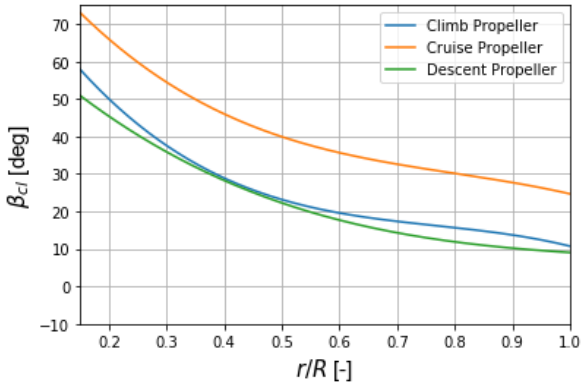

Figure 5.14: Climb blade angle for VPCR, B = 3

In figures 5.15 and 5.16, the cruise blade angle distributions are plotted for two and three blades respectively. Here, it can be seen that the cruise blade angles are lower than the climb blade angles as expected, since less thrust is required and as a result, lower angles of attack become beneficial for meeting the cruise thrust constraint. The descent propeller attains a low blade angle distribution in this case since the descent velocity is low. In order to meet the low thrust constraint, the pitch is decreased so the blade sections operate at lower blade angles and consequently, at efficient angles of attack.

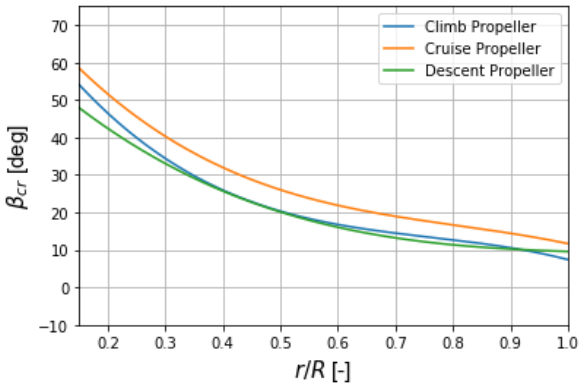

Figure 5.15: Cruise blade angle for VPCR, B = 2

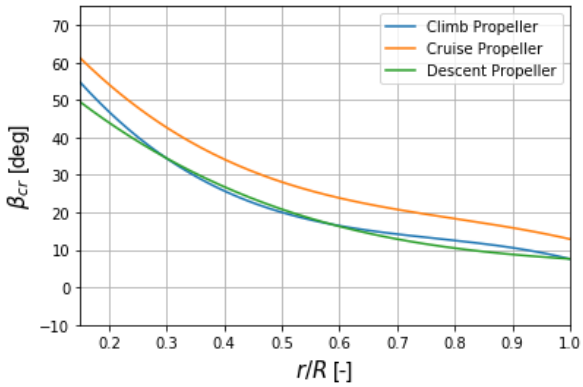

Figure 5.16: Cruise blade angle for VPCR, B = 3

In figures 5.17 and 5.18, the descent blade angles are shown for the two-bladed and three-bladed propellers. In this case, the climb and cruise propellers operate at lower blade angles since as a result of less blade area, it is beneficial for these propeller geometries to operate at higher angles of attack for maximum energy recuperation.

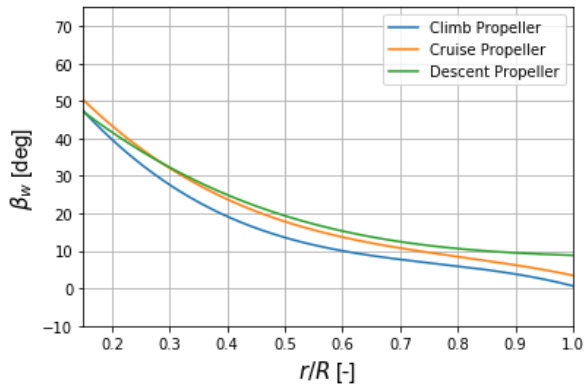

Figure 5.17: Descent blade angle for VPCR, B = 2

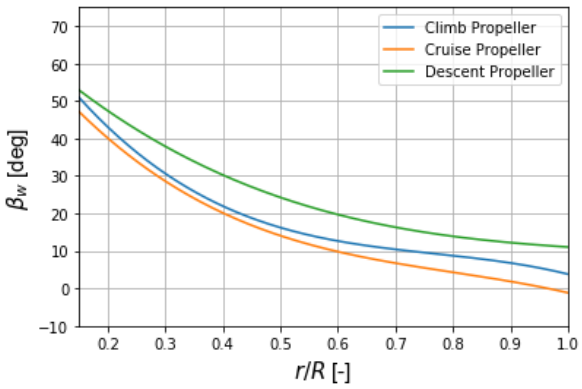

Figure 5.18: Descent blade angle for VPCR, B = 3

5.2.3. CASE 3: VARIABLE PITCH, VARIABLE RPM

In figures 5.19 and 5.20, the chord distributions for the two-bladed and three-bladed propellers for the VPVR optimisation case are shown. Again, it can be seen that the chord distributions of the climb and cruise propellers are similar and this time, the descent propellers have slightly less solidity. This can be explained by the fact that in this case, since both the pitch and the RPM are variable in all flight phases, there are more combinations of blade angle and RPM possible to be able to meet the thrust constraints during climb and cruise. As a result, less descent blade surface area is required to meet in particular the large climb thrust constraint. The climb and cruise propellers attain the same geometry with similar solidity. This is most likely related to the fact that the same thrust constraints are required to be met as for the CPVR and VPCR cases, the small differences in propeller optimisations for all cases being determined by their blade angle distributions and RPM to a larger extent.

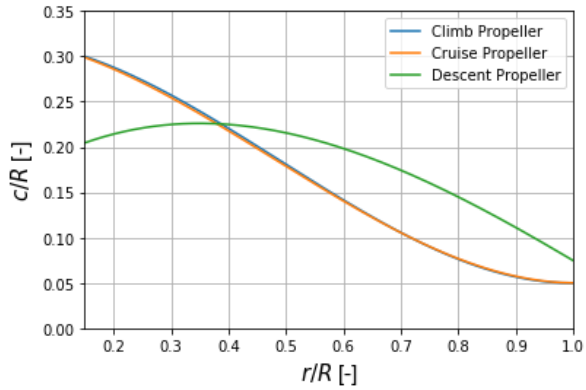

Figure 5.19: Chord distributions for VPVR, B = 2.

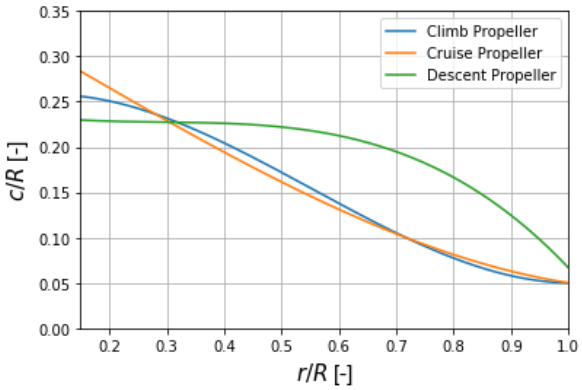

Figure 5.20: Chord distributions for VPVR, B = 3

In figures 5.21 and 5.22, the climb blade angle distributions are plotted for the two-bladed and three-bladed propellers. It can be concluded that also for the VPVR case, the blade angles of the cruise propeller must be increased in order to meet the climb thrust constraint with a low blade radius, operating at maximum RPM. The blade sections operate at higher angles of attack as a result. In the VPVR case, the cruise propeller operates at higher RPM than in the VPCR case where the RPM is fixed at 2250 rev/min. Therefore, the high RPM in the VPVR case contributes more to the increase in section angles of attack than in the VPCR case and as a result, similar angles of attack can be attained at lower blade angles in the VPVR case. This can also be seen when comparing figures 5.21 and 5.13. For the climb and descent propellers, it is clear that the two-bladed descent propeller now requires higher blade angles than the climb propeller. For climb, high thrust is required and therefore, it is beneficial to obtain a high L/D at a low inflow angle. As a result, the optimiser increases the RPM to a higher value and the blade angle is lowered in order to maintain efficient angles of attack along the span. For three blades, a lower climb RPM is required due to the added solidity and as a result, the inflow angle increases. In order to maintain efficient angles of attack, the blade angle increases as well with respect to the two-bladed propeller.

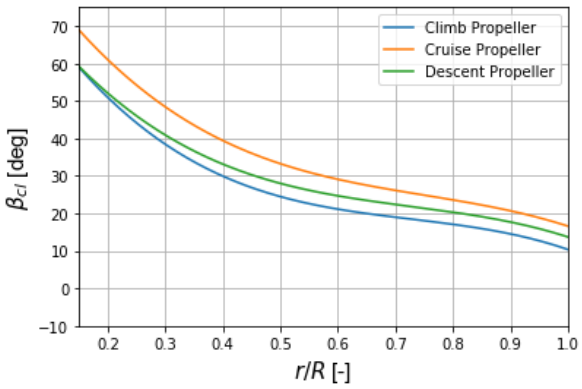

Figure 5.21: Climb blade angle for VPVR, B = 2

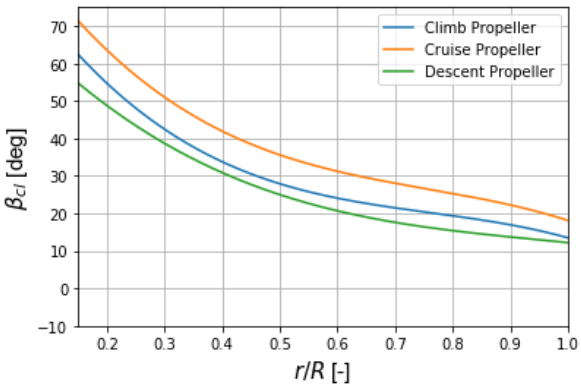

Figure 5.22: Climb blade angle for VPVR, B = 3

In figures 5.23 and 5.24, the cruise blade angle distributions are plotted for the two-bladed and three-bladed propellers. Operating at the lowest possible RPM value as constrained by the optimisation problem and as a result of the low thrust requirement in cruise, the blade angles are relatively high for the cruise propeller in order to prevent the angles of attack from becoming too low.

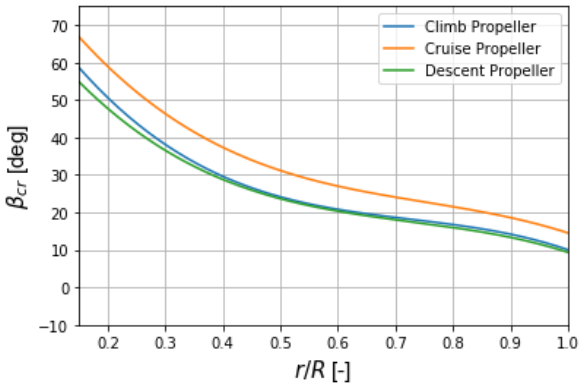

Figure 5.23: Cruise blade angle for VPVR, B = 2

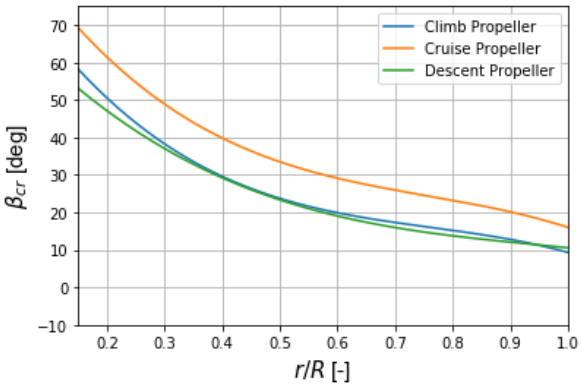

Figure 5.24: Cruise blade angle for VPVR, B = 3

In figures 5.21 and 5.22, the descent blade angles are plotted for the two-bladed and three-bladed propellers. Again, the descent propellers show higher descent blade angles than the climb and cruise propellers since the latter have less blade area and therefore require lower negative angles of attack for maximum energy recuperation than the descent propeller itself.

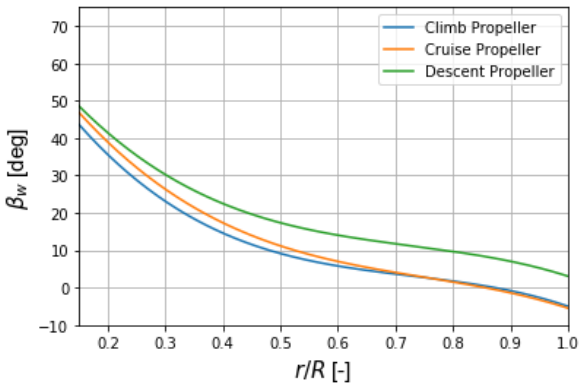

Figure 5.25: Descent blade angle for VPVR, B = 2

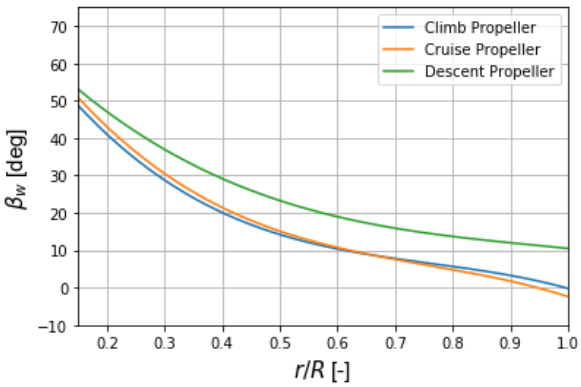

Figure 5.26: Descent blade angle for VPVR, B = 3

5.3. PROPELLER RADIUS

In figure 5.27, the propeller radius is plotted for all optimisation cases and number of blades. It is evident that the propellers designed for cruise operation attain smaller radii than the climb and descent propellers. A possible reason for this is the low thrust requirement in cruise; the thrust requirement for climb is about four times the cruise thrust required, while the descent velocity is variable and with this the descent thrust does not become an equality constraint for the optimisation. From the propeller analysis results, it can be observed that the cruise propellers operate at very low angles of attack along the blade span, often even negative angles of attack are present over the majority of the span. At these negative angles of attack, the applied highly cambered NACA 4415 airfoil still generates positive lift. A larger radius at a similar solidity for the cruise propellers would imply that the angles of attack would even become more negative in order to comply with the low thrust equality constraint, with a large drop in the lift coefficient and a significant increase in the drag coefficient as a result. This could lead to a large loss in efficiency due to a decreased L/D in this situation and as a result, an increase in cruise energy consumption, which is possibly the reason why the optimiser selects a lower radius for the cruise propellers. A high radius with a low solidity for cruise would most likely lead to low Reynolds numbers which would negatively impact the L/D performance of the blade.

On the other hand, for the climb and descent propellers a large radius seems to be beneficial. For climb, a high thrust equality constraint needs to be met. A high radius is therefore selected in order to eliminate the need to increase the section angles of attack along the blade span too much as this would lead to a significant loss in lift and increase in drag, both detrimental for obtaining high thrust. A large radius is likely favoured over an increase in the local chord values since the propeller diameter has a larger influence on the power absorption than the blade chord values [35]. For descent, a large radius is also beneficial since a large negative power is aimed to be achieved. Since the highly cambered airfoils are exposed to negative angles of attack in the descent phase, the loss in efficiency as the angle of attack becomes more negative is limited by increasing the propeller radius and the resulting larger area also means that more power can be extracted from the flow. It is also clear from figure 5.27 that the propeller radius for the three-bladed cruise propellers is lower than for the two-bladed propellers in all cases. The dominant factor resulting in the optimiser to reduce the radii for the three-bladed propellers are most likely their higher solidity. The chord distributions of the two-bladed and three-bladed cruise propellers are relatively similar and as a result, the solidities of the three-bladed propellers become higher than the solidity of the two-bladed propellers. In order to achieve similar thrust performance, the radius is therefore decreased for the three-bladed propeller since the thrust coefficient increases with the solidity.

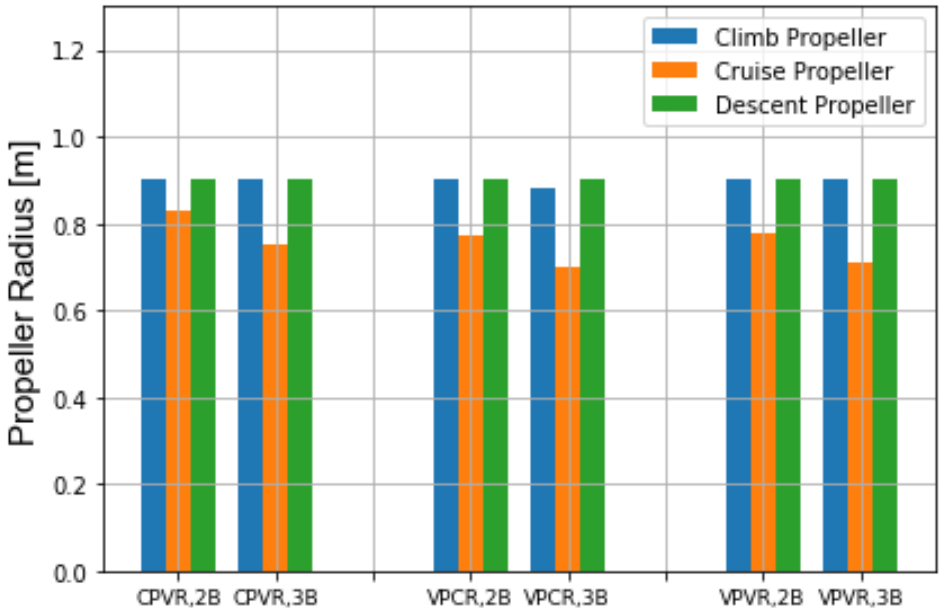

Figure 5.27: Propeller radius

5.4. MISSION ENERGY PERFORMANCE

In the previous sections, all propeller geometry parameters have been discussed and in this section, the total energy consumed during the entire flight phase is discussed for all optimisation cases and number of blades. In figure 5.28, the total energy consumed over the mission profile in figure 4.2 for a cruise distance of d_{cr} = 200 km is shown for all combinations of propeller operation and number of blades. It is clear that generally, the propeller optimised for cruise performance has the lowest energy consumption when it is used over the whole flight mission. This can be explained by the fact that the cruise distance of 200 km is relatively large compared to the distances covered during climb and descent. Although during the climb phase the energy consumption per unit time is highest, the relatively large decrease in efficiency of the cruise propeller in the climb phase (see figure 5.29) does not outweigh the gain in its energy performance during cruise. Furthermore, it can be seen that the propeller optimised for climb performance consumes slightly more energy over the entire mission than the cruise propeller. This propeller is obviously most efficient in the intensive climb phase, which ultimately contributes to the total mission energy consumption of the climb propeller being close to the results for the cruise propeller for all cases in figure 5.28, despite the relatively low fraction of the energy consumed in the climb phase over this considered mission. The propeller optimised for descent performance consumes most energy when operated over the entire mission as can clearly be observed from figure 5.28. This is expected, since the geometry of the descent propeller is optimised to achieve maximum negative lift and minimum drag at local negative angles of attack and at relatively lower Reynolds and Mach numbers, which influence the lift and drag, as compared to the climb and cruise phases. The section chord lengths influence the Reynolds number and the local blade loading, and are therefore also relevant in relation to aerodynamic performance. On the contrary, during climb and cruise the propeller blade sections operate at positive angles of attack and relatively high Reynolds numbers. Exposing the optimised geometry of the descent propeller to these conditions can be expected to result in lower overall mission performance. In sections 5.5 - 5.7, respectively the climb, cruise and descent efficiency performances of all single-point optimised propellers are analysed in each separate flight phase and will further contribute to the elucidation of the observations as seen for the complete mission performance in figure 5.28. The efficiency is closely related to the energy consumption. That is, the higher the propeller efficiency that can be achieved during a particular flight phase, the lower the energy consumption and vice versa.

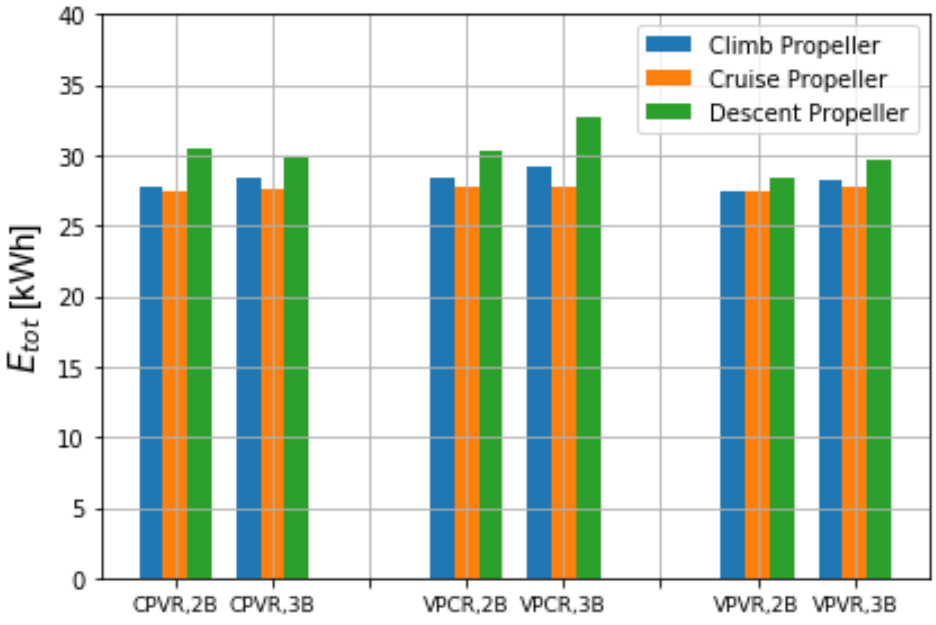

Figure 5.28: Total mission energy consumption

5.5. CLIMB PERFORMANCE

In figure 5.29, the climb efficiency results of all single-point optimised propellers for all optimisation cases (CPVR, VPCR, VPVR) are shown. As can be seen, for all cases the highest efficiencies are reached by the

propeller optimised for climb. In most cases, the propeller optimised for descent shows increased climb efficiency with respect to the cruise propeller which is generally the least efficient when operationally optimised for climb. Only for the constant pitch, variable RPM operation case the climb efficiency attained for the propeller optimised for descent is lower than for the cruise propeller.

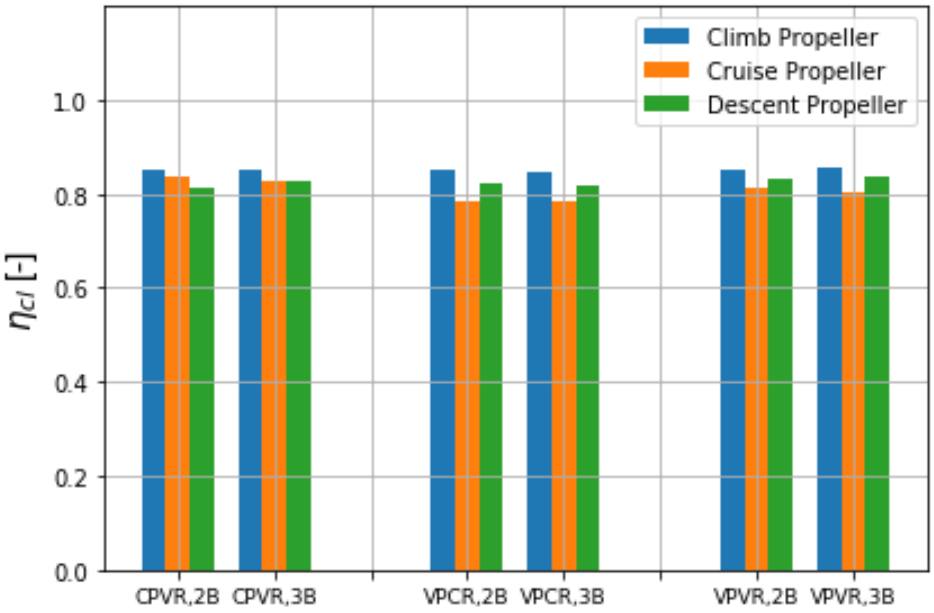

Figure 5.29: Climb efficiency

From the discussion on the propeller geometries and blade angles in section 5.2, it became clear that the propeller optimised for cruise in the CPVR case has a similar solidity, a smaller radius and is exposed to higher blade angles over its entire span with respect to the propeller optimised for climb. Therefore, in order for the cruise propeller to achieve the same climb thrust as the climb propeller at the same climb velocity, from equation 2.56 it is clear that the thrust coefficient K_T is required to increase. From equation 2.52, this implies that it is beneficial for the cruise propeller, having a solidity σ similar to the climb propeller, to increase its L/D in climb. In order to achieve this, the angle of attack distribution over the blade during climb is shifted upwards with respect to the climb angle of attack distribution of the climb propeller by increasing the RPM and the slightly lower flight velocity in climb contributes to an increase in the angle of attack as well. This results in increased values of the lift and drag coefficients along the blade span for the cruise propeller operation in climbing flight, however, as the propeller analysis results show, increased values of L/D are attained over the majority of the blade span. Since both the blade angles and the angles of attack along the cruise propeller blade span are higher than for the climb propeller in the climb phase, by equation 2.41 it can be concluded that the inflow angles ϕ are similar in both cases. From equation 2.53 it is therefore clear that for an increase in both the lift and drag coefficient the torque coefficient K_Q increases as well. Since the power coefficient K_P is directly proportional to both the torque coefficient and the rotational velocity, this explains why the power coefficient of the cruise propeller increases quite significantly with respect to the power coefficient of the climb propeller in climb. As a result, from equation 2.58 it can be explained why the cruise propeller attains a slightly lower efficiency than the climb propeller during climb.

Regarding the performance of the descent propeller during climb, it is clear that for the CPVR case, its climb efficiency is lower than the values attained for the climb and cruise propellers. The descent propeller has a higher solidity and lower blade angles than the climb and cruise propellers. The descent propeller has a similar radius to the climb propeller and therefore, its thrust coefficient needs to be similar to the one of the climb propeller in order to achieve the same required climb thrust. For this, it needs to be ensured that higher L/D values are attained along the blade span of the descent propeller during climb as compared to the L/D values seen during descent. The climb velocity is higher than the descent velocity, which decreases the local angles of attack. Since also lower blade angles are seen for the descent propeller, the angle of attack increase along the blade span during climb must therefore be realised by increasing the blade RPM. As a result of the low blade angles, the angles of attack of the descent propeller during climb are lower than for

the climb and cruise propellers. This results in lower values for C_l along the blade span and slightly lower C_d values. The overall L/D values attained for the descent propeller during climb are still lower than for the climb and cruise propellers during climb, however, the larger solidity of the descent propeller increases the thrust coefficient K_T to a sufficient value to meet the climb thrust requirement. The torque coefficient of the descent propeller during climb is decreased by the low values for the lift and drag coefficients and increased by the relatively high solidity and as a result, it is similar to the torque coefficient of the climb propeller. However, as a result of the higher RPM, the power coefficient of the descent propeller during climb increases and this explains the reduction in climb efficiency of the descent propeller with respect to the climb efficiency of the climb propeller. Both the thrust and power coefficients of the descent propeller during climb decrease by approximately the same amount with respect to the values seen for the cruise propeller during climb. This results in the climb efficiency of the descent propeller being lower than for the cruise propeller.

Observing the VPCR case in figure 5.29, it can be seen that the climb efficiency is lowest for the propeller optimised for cruise. The cruise propeller has a smaller radius than the climb and descent propellers in all cases. This means that in order for the cruise propeller to meet the climb thrust requirement, its thrust coefficient needs to be increased. In the VPCR case however, the RPM remains constant in both climb and cruise. This implies that in order to reach the required thrust coefficient, the optimiser increases the blade pitch angle of the cruise propeller significantly for the climb phase. This results in higher values of L/D over the majority of the cruise propeller blade span during climb. However, due to the high angles of attack encountered at the blade root due to the high blade angle required, the drag near the root of the cruise propeller blade during climb becomes very high. The high values of C_l and C_d result in a very high climb torque coefficient K_Q for the cruise propeller. Despite the increase in climb thrust coefficient K_T for the cruise propeller, the climb torque coefficient increases to a larger extent due to the large increase in drag coefficient at the blade root during climb. This leads to a considerable drop in the cruise propeller efficiency in the climb phase. On the other hand, the descent propeller needs a lower pitch setting to achieve the same climb thrust requirement since its solidity is higher. This leads to a lower thrust coefficient than for the cruise propeller and the resulting low negative angles of attack along the span of the descent propeller during climb lead to very low drag coefficients, which in turn result in a low torque and power coefficient. This ultimately results in an increased climb efficiency of the descent propeller with respect to the climb efficiency of the cruise propeller.

The VPVR case shows similar behaviour to the VPCR case, however, it can be observed that the cruise efficiency is slightly higher. This is the result of the RPM of the cruise propeller to be allowed to increase during climb in this case. Therefore, higher resulting velocities at the blade sections mean that the same climb thrust can be realised at lower angles of attack. This decreases the drag and improves the lift to drag ratio of the cruise propeller in climb, leading to a higher climb efficiency.

5.6. CRUISE PERFORMANCE

In figure 5.30, the cruise efficiencies attained for all optimisation cases and number of blades is shown. The same trend is observed for all cases; the highest cruise efficiencies are obviously reached by the propeller optimised for cruise, the climb propeller has a slightly lower cruise efficiency and the descent propeller performs worst in cruise for all cases.

In the CPVR case, the blade angles along the cruise propeller blade span are higher than along the climb propeller and lowest along the descent propeller blade span. Despite the decrease in cruise angles of attack along the climb propeller caused by the increased velocity in cruise, the cruise RPM of the climb propeller is not altered by the optimiser. Due to the larger radius of the climb propeller and a very similar chord distribution to the cruise propeller, the cruise thrust requirement can still be met at slightly lower angles of attack along the blade span. This leads to a decrease in the cruise L/D values along the climb propeller blade span resulting in a lower cruise thrust coefficient K_T, which is eventually the leading cause of the decrease in cruise efficiency of the climb propeller as compared to the cruise propeller during cruise. The descent propeller shows relatively low blade angles along its blade span and therefore, for the considerably increased velocity in cruise as compared to the descent phase, in order to achieve sufficient lift along the blade the angles of attack need to be increased by increasing the RPM of the descent propeller for cruise operation. However, due to its large solidity, the descent propeller only needs low angles of attack in cruise in order to achieve sufficient thrust. This results in low L/D values and consequently, a low thrust coefficient for the descent propeller in cruise. The torque coefficient is increased by the high solidity, however, decreased by the low cruise lift and drag coefficients found for the descent propeller. The result is little alteration to the torque coefficient and therefore, the considerably lower thrust coefficient leads to a low cruise efficiency of the descent propeller.

For the VPCR case, the most remarkable observation is the relatively low cruise efficiency of the descent propeller with three blades. Propeller analysis results show only slightly decreased angles of attack and lift coefficients along the majority of the blade span in that case. However, the higher number of blades likely causes the torque coefficient to increase since the torque coefficient increases with the solidity. As a result, the power coefficient increases as well, since for the descent propeller in cruise, the advance ratio is the same for two and three blades since both the radius and RPM are the same for both cases. This causes the cruise efficiency drop observed for the three-bladed descent propeller.

In the VPVR case, it can be seen that the cruise efficiencies reached are slightly higher for most cases, especially for the descent propeller. The solidity of the descent propeller is slightly less in this case, which implies that for achieving the same thrust, the pitch setting and RPM are selected such that higher angles of attack are present along the blade in order to increase the lift and drag coefficients. In this case, this leads to an improvement in L/D values and hence a higher thrust coefficient. What's more, the lower cruise RPM as compared to the VPCR case reduces the cruise power coefficient. This leads to an improved cruise efficiency of the descent propeller.

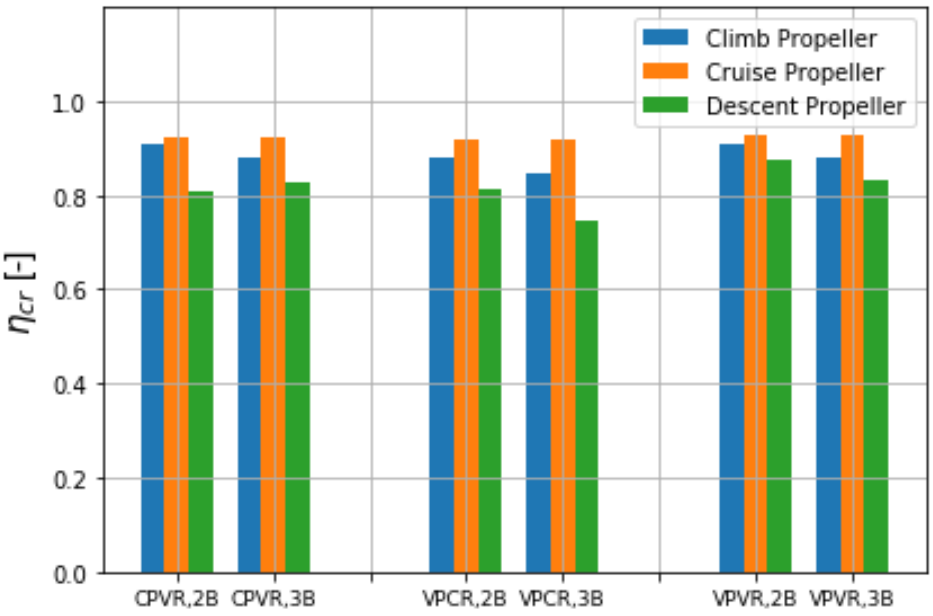

Figure 5.30: Cruise efficiency

5.7. DESCENT PERFORMANCE

In figure 5.31, the descent efficiencies are plotted for all optimisation cases and number of blades. As expected, the propellers optimised for the descent phase show the highest descent efficiencies in all cases. It can also be observed that the climb propellers perform better during descent than the cruise propellers in all cases. First of all, the difference between the descent efficiency performances of the climb and cruise propeller are analysed for two and three blades for the CPVR case. The two-bladed climb and cruise propellers for the CPVR optimisation case have a very similar chord distribution, however, the climb propeller has a larger radius. The cruise propeller has higher blade angles, while during descent, the propeller requires small blade angles to achieve negative angles of attack which are beneficial for energy harvesting performance. The descent velocity is relatively small and therefore in order to prevent too large positive angles of attack and to be able to meet the minimum rate of descent constraint, the optimiser selects the smallest possible descent RPM for the cruise propeller in order to decrease the angles of attack to have sufficient negative thrust to meet the rate of descent constraint. Since the climb propeller has lower blade angles than the cruise propeller, lower angles of attack can be reached by decreasing the RPM to its minimum value and this leads to lower negative descent lift coefficients along the majority of the blade span for the climb propeller. This leads to only a slightly lower negative torque coefficient for the climb propeller, since the torque coefficient of the cruise propeller is, despite its more positive lift coefficients, also decreased by its slightly larger solidity. Since the climb and cruise propeller are operated at the same RPM during descent, the cruise propeller has a larger

descent advance ratio due to its smaller radius. This is eventually the leading cause of the decrease in the descent efficiency of the cruise propeller with respect to the climb propeller. For three blades in the CPVR case, the blade angles of the climb propeller are lower than for two blades. Negative angles of attack are easier realised by decreasing the RPM for descent. This leads to more negative lift coefficients and this is the leading cause of the the torque coefficient becoming more negative than for the two-bladed case and this leads to an increase in descent efficiency of the three-bladed climb propeller with respect to the two-bladed one.

For the VPCR case in figure 5.31, it is clear that the climb efficiencies of the climb and cruise propellers are higher than for the CPVR case. Comparing the chord distributions of the propeller blades in the the VPCR case to the CPVR case, it can be seen that they are very similar. However, in the VPCR case, the pitch is also variable in descent, which can significantly improve the descent efficiency performance of the climb and cruise propeller geometries. The descent blade angles of the VPCR climb propellers are selected to be lower as compared to the CPVR case for the descent phase in order to prevent the RPM from becoming too low, since that would lead to a decrease in reverse thrust and as a result less energy would be harvested. This explains why higher RPM values are seen for the climb and cruise propellers during descent, also in order to prevent the angles of attack from becoming too negative, which would decrease descent performance of the applied highly positive cambered NACA 4415 airfoil exposed to negative angles of attack during descent. The higher descent RPM of the climb propeller results in a higher resultant velocity and higher negative thrust. Furthermore, it leads to a lower advance ratio for the two-bladed climb propeller and even lower for the three-bladed propeller; possibly since the three-bladed propeller has a larger solidity, this allows to reduce the angles of attack by increasing the RPM, which becomes beneficial for increasing the descent efficiency more than achieving higher absolute values for lift and drag as seen along the two-bladed propeller. Regarding the descent performance of the cruise propeller, it can be seen that it reaches higher efficiencies than in the CPVR and VPVR cases. The cruise propellers have a smaller radius than the climb and descent propellers, which leads to an increase in descent RPM to increase the reverse thrust in order to meet the rate of descent constraint. This leads to an increase in the descent torque coefficient and together with a larger RPM, the descent efficiency of the cruise propeller in the VPCR case increases with respect to the CPVR case. In the CPVR case, the descent blade angles of the cruise propeller are higher which requires a smaller RPM in descent in order to maintain sufficient negative angle of attack to meet the rate of descent constraint. However, the smaller descent RPM in the CPVR case decreases the descent torque coefficient and the descent efficiency in this case. For the VPVR case, it is noticed that the descent efficiency of the cruise propellers are lower than for the VPCR case, even though the radius and chord distributions of the VPCR and VPVR cruise propellers are very similar. For the VPVR case, the difference between the blade angles at the root and tip is larger. As a consequence, when the blade pitch of the VPVR cruise propeller is decreased for descent operation, negative blade angles are present at the blade tip. This leads to highly negative angles of attack at the blade tip with a loss in lift as a result. What's more, the descent RPM is lower for the VPVR cruise propeller as compared to the VPCR cruise propeller in order to maintain smaller negative descent angles of attack at the blade root of the VPVR cruise propeller. This lower RPM contributes to a decrease in descent efficiency, also by decreasing the descent torque coefficient, of the VPVR cruise propeller as compared to the VPCR descent efficiency of the cruise propeller.

Furthermore, it is interesting to note from figure 5.31 that the differences between the descent efficiency performance of the climb and cruise propellers with two blades are consistently smaller than for three blades. This is most likely influenced by the cruise propeller radius being smaller for three blades than for two blades in all optimisation cases (CPVR, VPCR and VPVR). The propeller designed for descent operation are all designed at the maximum possible radius, which indicates that a large radius is beneficial for descent.

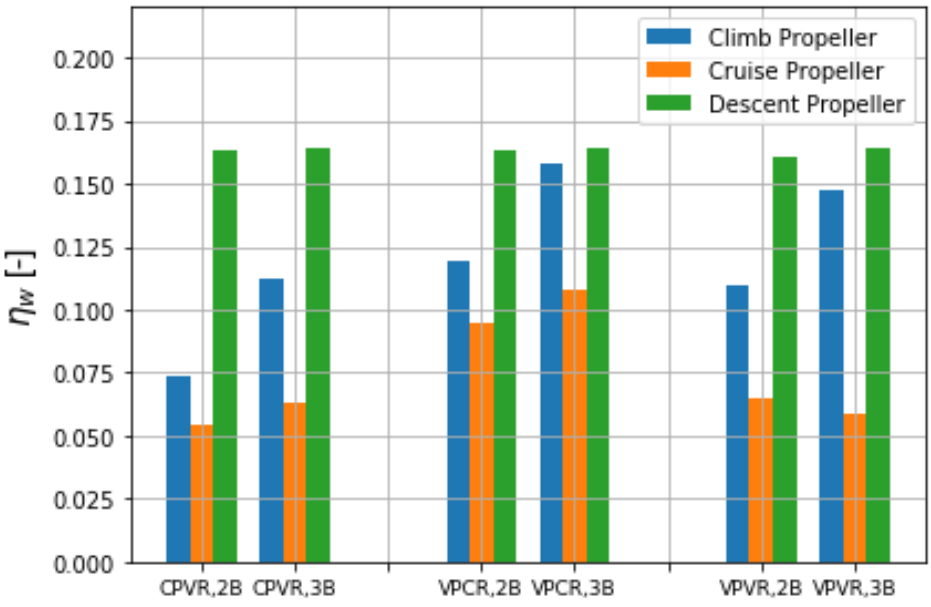

Figure 5.31: Descent efficiency

5.8. RATE OF DESCENT

In figure 5.32, the rate of descent is plotted for all optimisation cases and number of blades. In order to maximise the energy harvesting performance, it is clear from figure 5.32 that the rate of descent is maximised in all cases. The rate of descent is directly proportional to the negative thrust generated during descent by equation 4.36. High negative L/D is important for energy harvesting, since this will lead to a large descent torque coefficient and consequently a desired high descent power coefficient. Since a high L/D also increases the magnitude of negative thrust, high rate of descents are indeed expected for the descent propellers in all optimisation cases. Furthermore, it is clear from figure 5.32 that the climb propellers have higher rates of descent than the cruise propellers. The rate of descent of a propeller is in a close correlation with the radius and solidity, since these influence the thrust to a large extent. The climb propellers have a large radius in all cases, however, their solidities are lower than the ones of the descent propellers. Since the velocity and RPM are lower in descent than in climb and cruise, an increase in solidity becomes more beneficial for obtaining high thrust, since the L/D section performance increases with Reynolds number and the larger blade area increases the thrust at low velocity. If high chord values would be applied for climb and cruise, the angles of attack would need to become too low in order to meet the set thrust equality constraints for these flight phases, resulting in poor aerodynamic efficiency of the blade sections. For these reasons, although the radii of the climb propellers are similar to the descent propellers, their rate of descent is lower as a result of lower negative thrust because of lower blade solidity at lower velocity and RPM operation with respect to the climb phase. Since the three-bladed climb propellers have a slightly higher solidity, their descent thrust becomes more negative and as a result, their rates of descent are higher than for the two-bladed propellers. Regarding the cruise propellers, these are designed both for relatively low radii and solidity. As a result, lower rates of descent are obtained. In this case, there is less difference between the two-bladed and the three-bladed propellers since, for a similar normilised chord distribution in both cases, the three-bladed cruise propellers have higher solidity but lower radii, and therefore they have a similar effect on the rate of descent as compared to the two-bladed propellers.

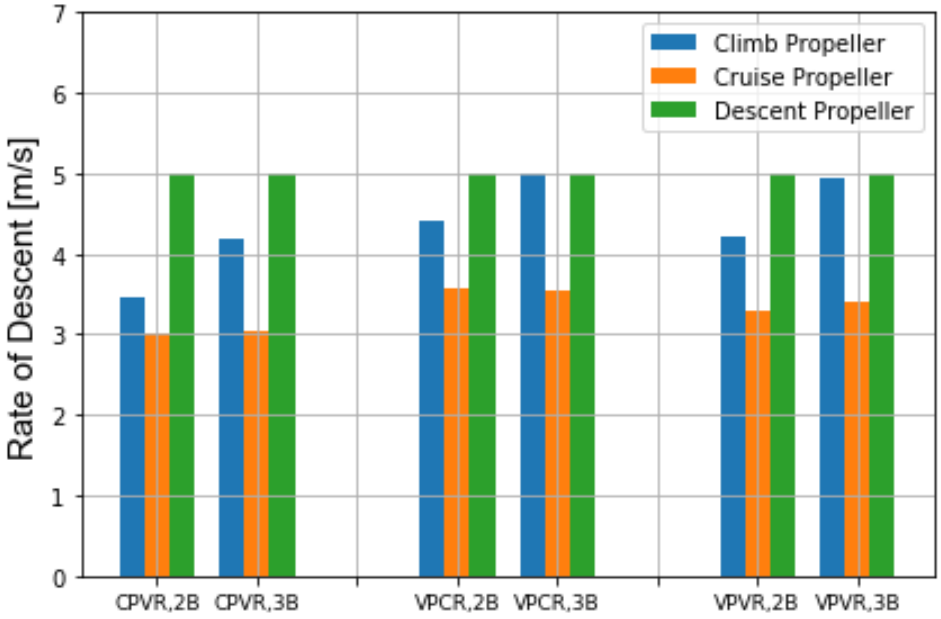

Figure 5.32: Rate of descent

In tables B.1 - B.3 in appendix B, all previously discussed performance and geometry results of the climb, cruise and descent propellers are summarised for all optimisation cases and number of blades.

6

Multi-Point Optimisation Results

In this chapter, the multi-point optimisation results, obtained by carrying out the optimisation problem as formulated in equation 4.50, are discussed for all combinations of optimisation case (CPVR, VPCR and VPVR) and number of blades. First, the propeller geometry results are presented in terms of the chord and blade angle distributions, which are subsequently used for the analysis of the propeller performance results. All the optimisations are now performed for the whole aircraft mission at cruise distances of 5, 25, 50, 100, 150 and 200 km and the resulting propeller performance parameters are plotted as a function the cruise distance. These include the propeller efficiency, energy performance and the rate of descent. Using non-linear least squares regression, curve fits are generated between the points representing the optimisation results at all considered cruise distances of the performance parameter under consideration. By doing this, the effect of varying the cruise distance within the aircraft mission on the propeller performance in climb, cruise, descent and over the total mission can be studied as well as the effect the cruise distance has on the propeller geometry resulting from the optimisations. Also, the relative energy performance and descent performance of the VPVR propeller with respect to the CPVR and VPCR propellers is presented. In this way, the improvements in performance that can be obtained by varying both the propeller pitch and RPM as compared to varying only the pitch or only the RPM of the propeller can be studied. Finally, the effects of airfoil camber and thickness are discussed in sections 6.5 and 6.6.

6.1. Chord and Blade Angle Distributions

In this section, the results for the chord and blade angle distributions for all optimisation cases, number of blades and cruise distances are discussed. Plots are made for the cruise distances of 5, 50, 100 and 200 km in all cases.

6.1.1. CPVR

In figures 6.1 and 6.2, the chord distributions for the CPVR case for two and three blades are shown respectively and in figures 6.3 - 6.6, the corresponding blade planform shapes are illustrated for two and three blades for the cruise distances of 5 km and 200 km. The most important observation is the decrease in blade solidity at larger cruise distances. As was seen before in chapter 5, large solidity is beneficial for descent and therefore it is indeed expected that for the lowest cruise distance the solidity is highest since in that case, the relative importance of the descent performance is highest. At large cruise distances, less solidity is beneficial in order to allow the blade sections to operate at positive angles of attack over a larger part of the blade span, since positive angles of attack on a highly cambered airfoil are beneficial for efficient operation. A large solidity in cruise would result in negative angles of attack over a larger part of the blade span, which would lead to lower aerodynamic blade section efficiencies. Furthermore, it is clear that the three-bladed propellers generally attain lower c/R values in order to compensate for the solidity gain by the extra blade, preventing the solidity from becoming too high for efficient blade section operation. At high cruise distances however, the chord distributions for two and three blades are more similar, where the three-bladed propeller attains a significantly lower radius in order to meet the same thrust constraint. For lower cruise distances where the descent performance has more relevance, a large radius is selected instead, since that is beneficial for good descent performance as discussed previously in chapter 5.

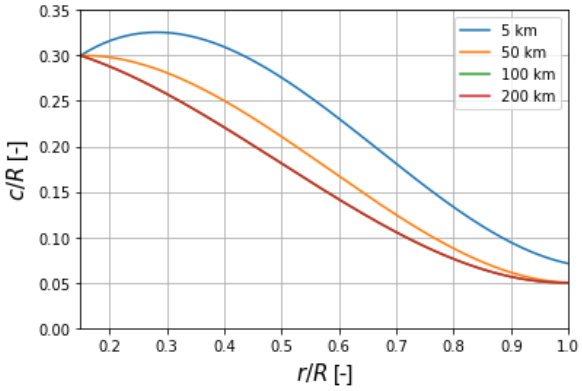

Figure 6.1: Chord distributions for CPVR, B = 2

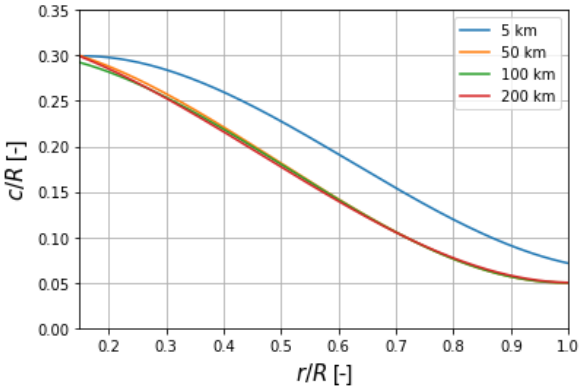

Figure 6.2: Chord distributions for CPVR, B = 3

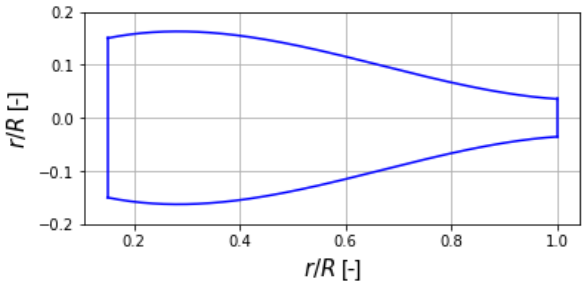

Figure 6.3: CPVR Chord distribution for d_{cr} = 5 km, B = 2

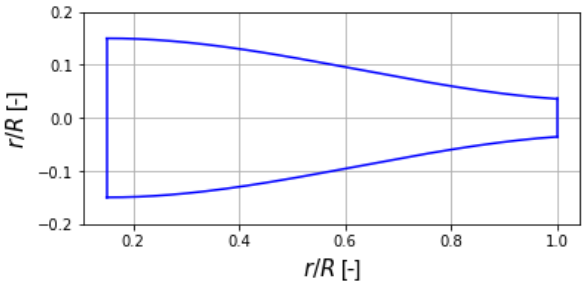

Figure 6.4: CPVR Chord distribution for d_{cr} = 5 km, B = 3

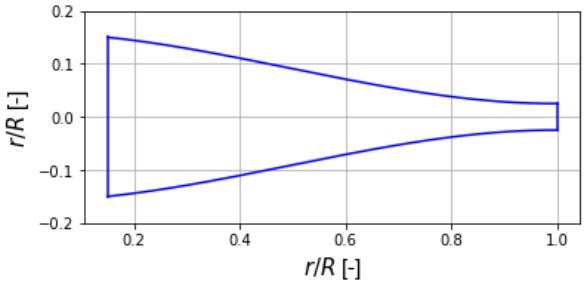

Figure 6.5: CPVR Chord distribution for d_{cr} = 200 km, B = 2

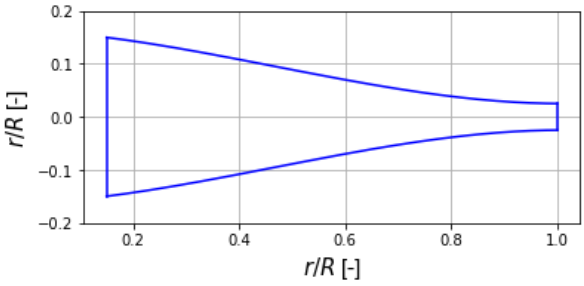

Figure 6.6: CPVR Chord distribution for d_{cr} = 200 km, B = 3

In figures 6.7 and 6.8, the blade angle distributions are plotted for two and three blades respectively for several cruise distances. It can be seen that the blade angles increase with the cruise distance. As mentioned before, high blade angles are beneficial for cruise since the cruise velocity is relatively high and since the thrust constraint is low, a low RPM in combination with a high blade angle is required in order for the blade sections to operate at an efficient L/D. This results in large inflow angles, which contribute to achieve the low required thrust value during cruise within the set bounds for the RPM within the optimisation. In order to maintain efficient angles of attack for good L/D performance, the blade angles are therefore required to be higher than for low cruise distances, where the climb and descent phases have more influence on the optimisation results.

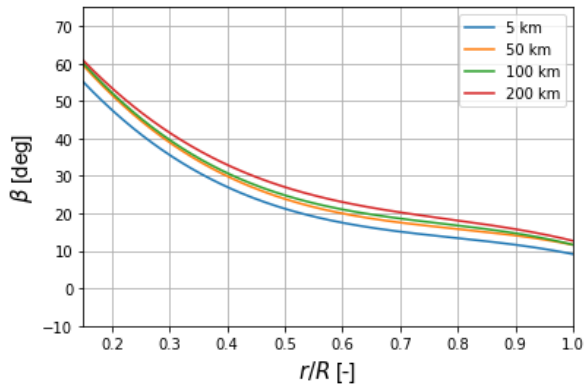

Figure 6.7: Blade angle distributions for CPVR, B = 2

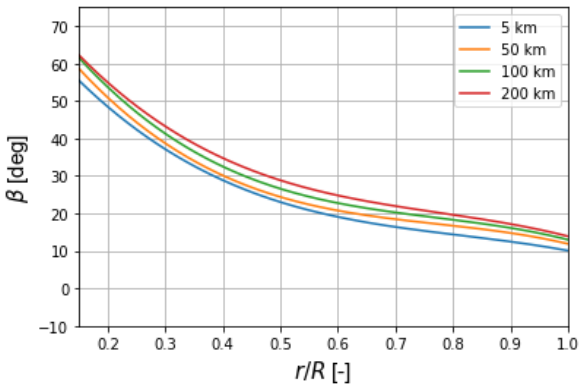

Figure 6.8: Blade angle distributions for CPVR, B = 3

6.1.2. VPCR

In figures 6.11 and 6.12, the blade angle distributions for the VPCR case are shown for two and three blades respectively. Compared to the CPVR case, it is clear that generally less solidity is needed here at lower cruise distances, where the climb and descent phases are very influential, since the pitch can be varied. This facilitates the blade sections to meet both the climb and rate of descent constraints where the sections operate at positive and negative angles of attack respectively and without the need of high a blade area to be able to meet all the constraints at a single pitch setting. Observing the difference between the blade chord shapes for two and three blades in figures 6.9 and 6.10, it can be seen that for example for the cruise distance of 5 km, the solidity is most significantly lower for the three-bladed propeller as compared to the two-bladed propeller. This is a result of the lower descent RPM selected by the optimiser, resulting in higher angles of attack and therefore a reduction in the blade area for the same propeller radius in order not to exceed the rate of descent constraint by an excessive negative thrust. On the other hand, for 200 km for example, the same descent RPM is selected by the optimiser for two and three blades but this time, the three-bladed propeller has a lower radius and slightly higher blade angles in all flight phases in order to meet the same thrust constraints as the two-bladed propeller.

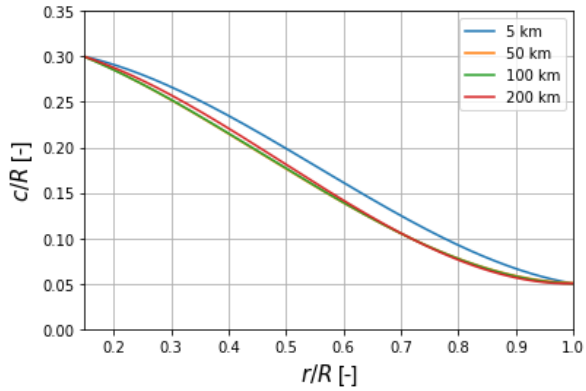

Figure 6.9: Chord Distributions for VPCR, B = 2

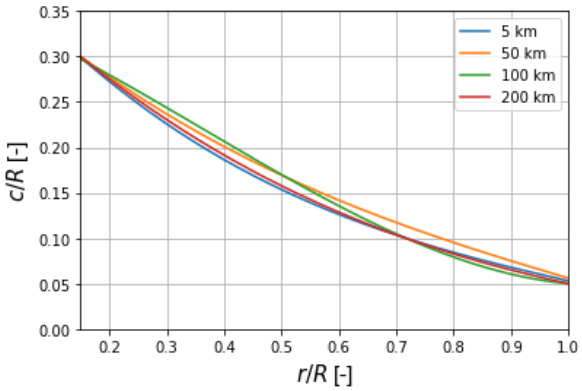

Figure 6.10: Chord Distributions for VPCR, B = 3

In figures 6.11 - 6.16, the blade angle distributions are shown for climb, cruise and descent for two and three blades for the VPCR optimisation case. Since the same RPM value is attained for climb and cruise, the climb blade angles are required to increase with respect to the cruise blade angles in order to meet the climb thrust constraint at sufficiently high angles of attack. The climb blade angles increase with cruise distance. This is the result of the blade solidity decrease when the cruise phase becomes more influential during the optimisation, requiring higher angles of attack during climb in order to meet the same climb thrust constraint. The lowest blade angles are seen during the descent phase, since the blade sections here are required to operate at negative angles of attack and since both the descent velocity and RPM are lower with respect to climb and cruise phases, lower blade angles are required for descent.

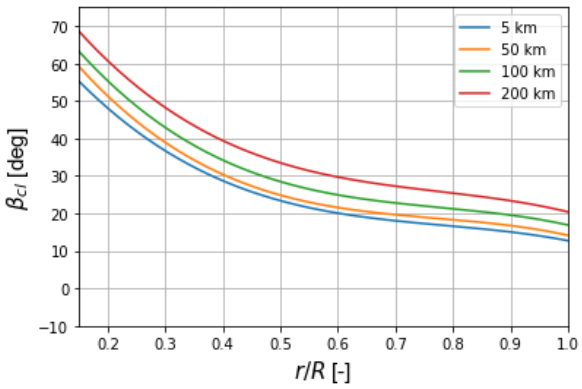

Figure 6.11: Climb blade angle distributions for VPCR, B = 2

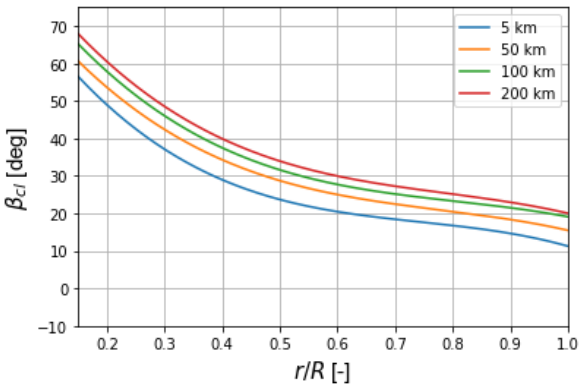

Figure 6.12: Climb blade angle distributions for VPCR, B = 3

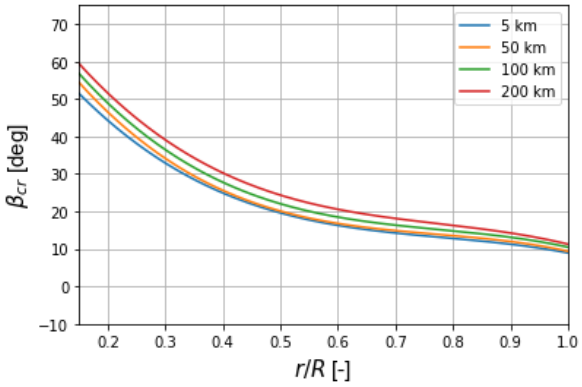

Figure 6.13: Cruise blade angle distributions for VPCR, B = 2

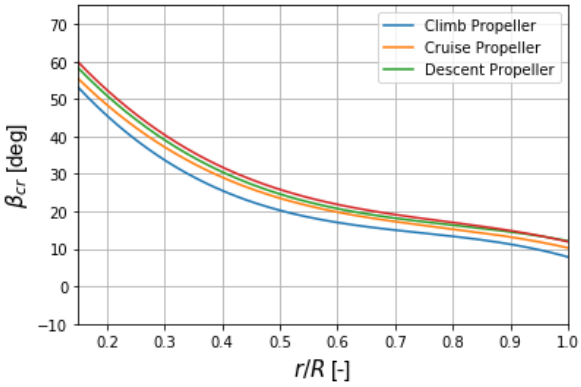

Figure 6.14: Cruise blade angle distributions for VPCR, B = 3

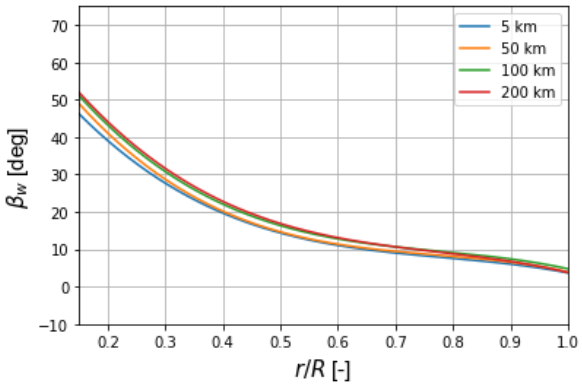

Figure 6.15: Descent blade angle distributions for VPCR, B = 2

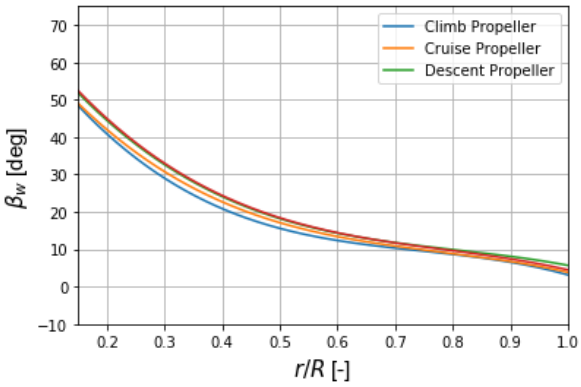

Figure 6.16: Descent blade angle distributions for VPCR, B = 3

6.1.3. VPVR

In figures 6.17 and 6.18, the chord distributions for the VPVR optimisation case are plotted for two and three blades respectively. Again, lower blade solidities are seen for the lower cruise distances with respect to the CPVR case, where the pitch is constant over the whole mission, as a result of the ability to vary the pitch in the VPVR case. At this point, it is interesting to compare the chord distributions in figure 6.17 of the multi-point optimisations to the chord distributions of the VPVR case from the single-point optimisation results as seen in figure 5.19. It can be seen that the chord distribution for the lowest cruise distance of 5 km has the highest solidity and it therefore resembles most the chord distribution of the descent propeller in figure 5.19. This is expected, since the descent phase has the highest relative importance at the lowest cruise distance of

5 km. However, the overall solidity for a 5 km cruise distance is still lower for the multi-point optimisation result since a compromise is found here for all flight phases, where a lower solidity is beneficial for cruise as outlined before. On the other hand, for the cruise distance of 200 km, the multi-point chord distribution result in figure 6.17 resembles the single-point cruise propeller optimisation result from figure 5.19. This is expected, since for a cruise distance of 200 km the cruise flight phase has the highest relative importance within the multi-point optimisation. Furthermore, the radius of the 200 km cruise propeller is slightly higher than for the cruise propeller from the single-point optimisation result, since for the climb and descent phases a larger radius is beneficial as outlined before.

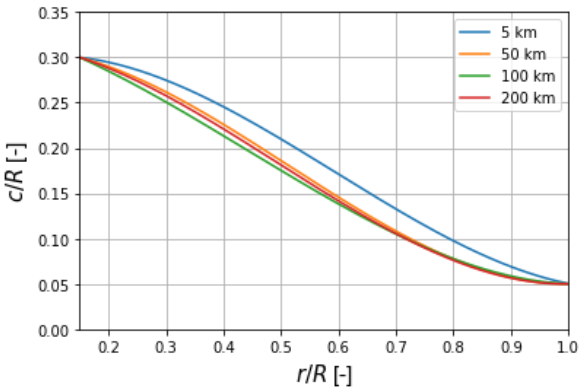

Figure 6.17: Chord Distributions for VPVR, B = 2

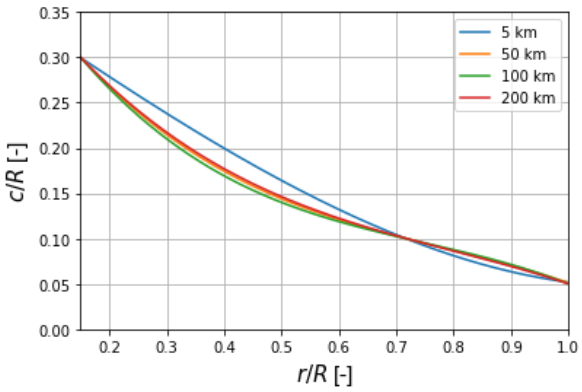

Figure 6.18: Chord Distributions for VPVR, B = 3

In figures 6.19 - 6.24, the blade angle distributions are plotted for the VPVR case for climb, cruise and descent for two and three blades. Since for the VPVR case the RPM can also be varied for all flight phases, this eliminates the requirement for high blade angles during climb. This can clearly be seen when comparing figures 6.19 and 6.20 to figures 6.11 and 6.12 for the VPCR case. Also, it is interesting to compare the cruise blade angle distributions in figure 6.21 to the VPVR single-point cruise blade angle distributions in figure 5.23. It can be seen that the higher the cruise distance, the more the blade angle distribution in figure 6.19 shifts towards the cruise blade angle distribution of the cruise propeller in figure 5.23 as expected, since the cruise phase becomes relatively more important for the optimisation as the cruise distance increases. Furthermore, as was seen for the VPCR case, for the VPVR case the descent blade angles required are again lower than for the climb and cruise phases.

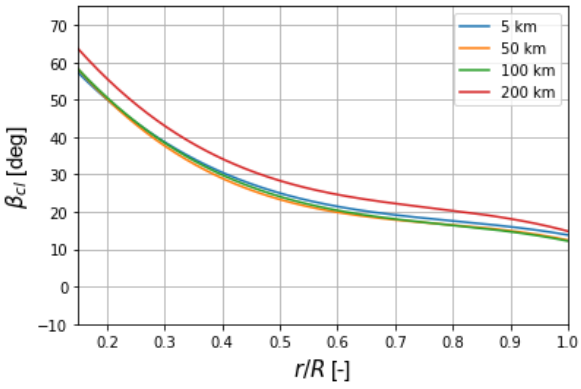

Figure 6.19: Climb blade angle distributions for VPVR, B = 2

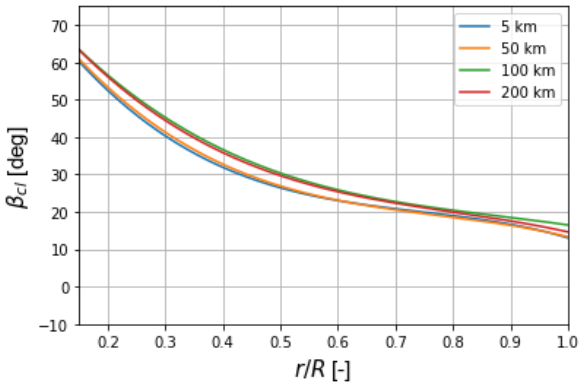

Figure 6.20: Climb blade angle distributions for VPVR, B = 3

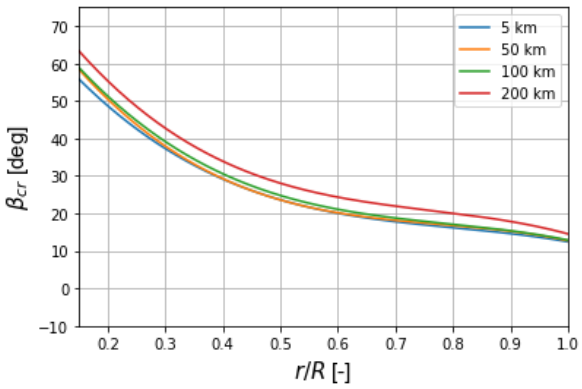

Figure 6.21: Cruise blade angle distributions for VPVR, B = 2

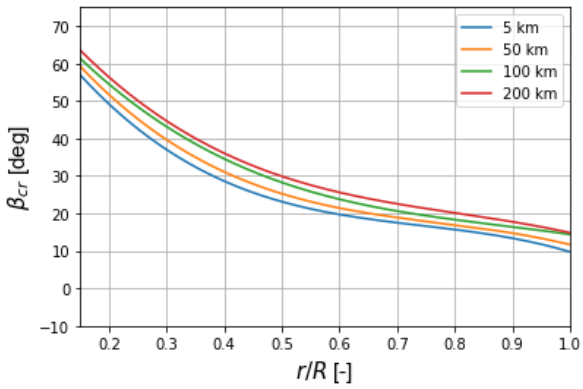

Figure 6.22: Cruise blade angle distributions for VPVR, B = 3

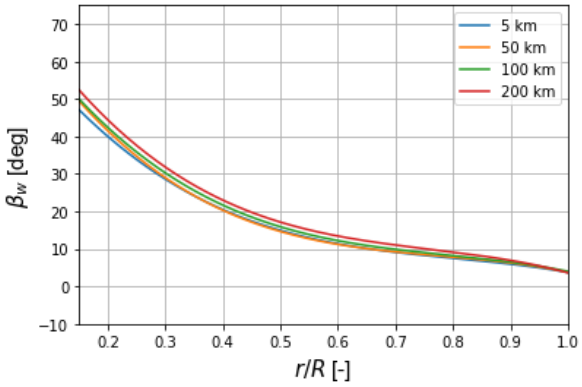

Figure 6.23: Descent blade angle distributions for VPVR, B = 2

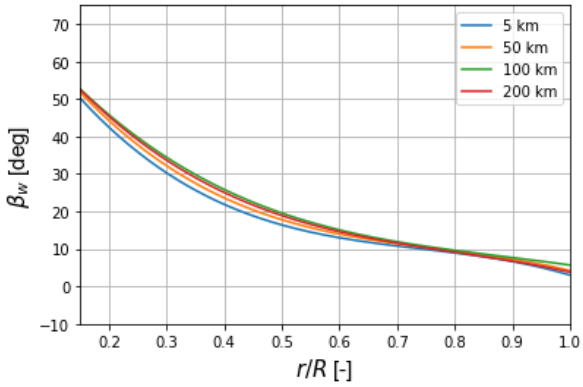

Figure 6.24: Descent blade angle distributions for VPVR, B = 3

6.2. PROPELLER EFFICIENCY

The propeller geometry results that have been obtained at this point are used in the subsequent sections to analyse the propeller performance. In this section, the propeller climb, cruise and descent efficiencies as a function of the cruise distance are presented and analysed for all optimisation cases. These propeller efficiency results are closely related to the propeller energy consumption, which is ultimately the most interesting aspect to investigate, and therefore they are useful for clarifying the subsequent discussion on the propeller energy consumption for all the optimisation cases in section 6.3.

6.2.1. CLIMB EFFICIENCY

In figure 6.25, the climb efficiency as a function of the cruise distance is plotted for the CPVR case for a two-bladed and three-bladed propeller. It can clearly be seen that in this case, the climb efficiency initially increases with the cruise distance and then decreases after a certain point both for the two-bladed and the three-bladed case. A possible explanation for this is the relative importance of the climb, cruise and descent phases in terms of energy consumption during the optimisation. In the CPVR optimisation case, the blade angle distribution along the blade span is the same for all flight phases. For low cruise distances, a high percentage of the energy can be recuperated during descent and this percentage decreases fast as cruise distance increases as will become clear later. For low cruise distances, the selected pitch setting is influenced by the amount of energy that can be recuperated with respect to the amount that can be saved during climb. For this reason, initially the pitch setting is selected in order to increase performance during descent and as cruise distance increases, it becomes more beneficial to select a pitch setting which will perform better during climb until a point is reached where the cruise distance becomes high relative to the climb and descent phases and the pitch setting is selected in order to increase cruise performance at the cost of climb performance. The higher climb efficiencies of the two-bladed propeller at higher cruise distances result from the fact that for large cruise distances, the chord distribution is optimised mostly for cruise operation and is very

similar for the two-bladed and three-bladed propellers; the main difference being the smaller radii for the three-bladed propellers in order to meet the same climb thrust constraint. The blade angle distributions are also very similar for the two-bladed and three-bladed propellers as will become clear later. With little variation in climb RPM as well, the inflow angles and angles of attack seen for the two-bladed and three-bladed propellers show only very small differences. However, the three-bladed propeller has a higher solidity than the two-bladed propeller and this is the main factor increasing both the climb thrust and the climb torque coefficients by about the same factor of the three-bladed propeller with respect to the two-bladed propeller for large cruise distances. The three-bladed propeller has a high climb torque coefficient and a lower climb efficiency for larger cruise distances as compared to the two-bladed propeller, since the radius is smaller than for the two-bladed propeller.

It must be mentioned that the differential evolution algorithm used to perform all the optimisations within this project is stochastic in nature and therefore, it is very unlikely that the global optimum found for a particular optimisation run will be the same for every other run. There are three main parameters within the differential evolution algorithm that have a large influence on its performance. As they have been discussed before, these are the population size, mutation constant and crossover constant. For the mutation, dithering is applied, however, the combination of the population size and crossover constant needs to be found using a trial and error process. The aim is to find the combination that leads to the best compromise between optimisation runtime and accuracy in finding the global optimum. The latter can be recognised by seeing little variation in the results between several runs. On the other hand, when significant differences between several runs are seen this implies that likely multiple local optima are being found and a change is required in the combination of population size and crossover constant. However, small changes between different optimisation runs will always remain, and in order to provide an estimate of the variability of the data points in the figures in this chapter, an error bar is added to each figure, as can also be seen in figure 6.25. The error bar represents a 95% confidence interval for the data points and its length is 1.96 times the standard deviation of the particular parameter under consideration, which is the climb efficiency in figure 6.25 for example. The standard deviation σ of a performance parameter is obtained by running a selected optimisation case (VPVR, two blades, 50 km cruise distance) multiple times and calculating it based on all the values of that parameter resulting from these runs using equation 6.1, where N is the number of runs, x_i are the values of the performance parameter under consideration resulting from the several runs and μ is the mean of all the values.

$$\sigma = \sqrt{\frac{1}{N}\sum_{i=1}^{N}\left(x_i - \mu\right)^2} \tag{6.1}$$

The VPVR case is selected for this purpose since it is the most interesting case for future applications and therefore, it is interesting to visualise the accuracy of the optimiser for that purpose. However, the difference in standard deviation that would have been computed using a different number of blades or a different optimisation case (CPVR or VPCR) is not expected to be too large. For the latter, this is because there is only a slight reduction in the total amount of design variables with respect to the VPVR case. In fact, the large amount of design variables within the VPVR optimisation case makes it a conservative choice for the calculation of the data variability. As explained shortly, the choice for the cruise distance for this purpose is expected to have a slightly larger effect on the standard deviation calculations and therefore, an intermediate cruise distance of 50 km is expected to give the best representation of the overall standard deviation.

For the VPCR and VPVR cases in this chapter, multiple points are plotted for the same optimisation run for three blades at the lowest cruise distances. There, the uncertainty in the data points is highest since the climb, cruise and descent performance are more equally influential for the final result and this results in more potential designs for the optimiser to select that perform similarly. In figure 6.26, the climb efficiency as a function of the cruise distance is plotted for the VPCR case for a two-bladed and three-bladed propeller. In this case, a clear difference can be seen with respect to the climb efficiencies obtained in the CPVR case. The climb efficiency drops much faster as the cruise distance increases. The three-bladed case at 200 km is considered as an example for the clarification of the difference seen in the climb efficiencies at 200 km in figures 6.25 and 6.26. In the CPVR case, the propeller operates at higher RPM and it has a higher radius in order to be able to meet the climb thrust constraint, since the pitch setting is mostly optimised for cruise here due to the relatively large cruise distance. As a result, lower angles of attack are required than for the VPCR case and this results in lower lift and drag coefficients and also in lower thrust, torque and power coefficients than for the VPCR case. However, as required, the total thrust remains the same during climb and cruise. In the VPCR

case, the propeller operates at slightly higher blade and inflow angles and the lift and drag coefficients are higher. A significantly higher torque coefficient is obtained as a result in the VPCR case, which increases the power coefficient significantly, and is the leading cause for decreasing the efficiency with respect to the CPVR case. This therefore explains the steeper drop in climb efficiency as the cruise distance increases for the VPCR case with respect to the CPVR case. However, despite the large differences seen between the climb efficiencies of the CPVR case and the VPCR case, there is relatively less difference between the various optimisation cases regarding the energy consumption performance over the entire mission.

At low cruise distances, the relatively high importance of the descent performance during the optimisation lowers the climb efficiency in the CPVR case with respect to the VPCR case. In the CPVR case, the pitch setting is fixed for the entire mission and the optimiser focusses more on ensuring good energy harvesting performance at low cruise distances in the CPVR case, at the cost of climb efficiency with the selected pitch setting. In the VPCR case, the pitch setting can be adjusted for climb and descent separately and the RPM in the descent is also variable. This possibly increases the climb efficiency at low cruise distances with respect to the CPVR case.

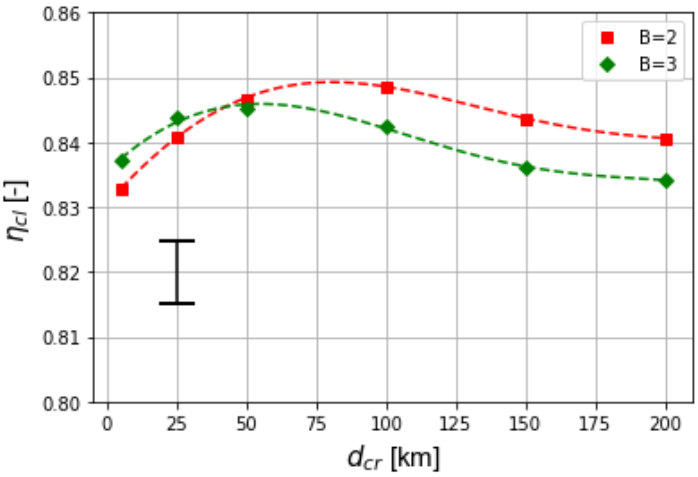

Figure 6.25: CPVR climb efficiency

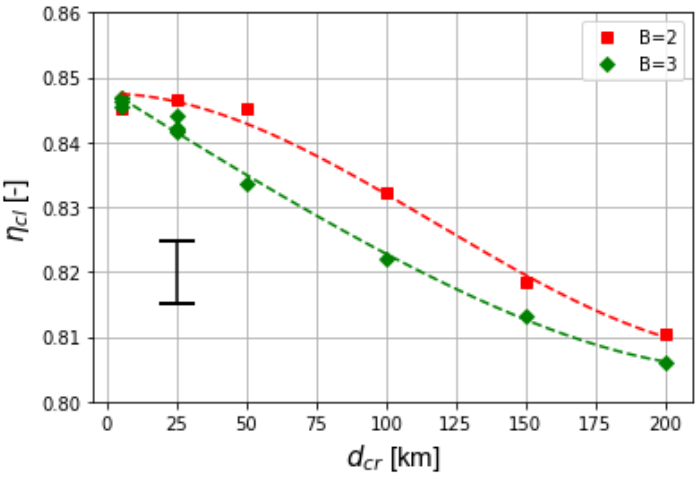

Figure 6.26: VPCR climb efficiency

In figure 6.27, the climb efficiency as a function of the cruise distance is plotted for the VPVR case for a two-bladed and three-bladed propeller. In this case, both the RPM and pitch settings are variable for all flight phases and as a result, the RPM and pitch settings can always be adjusted for good performance in all flight phases. The decrease in climb efficiency as cruise distance increases is then a result of the changes in chord

and blade angle distributions optimised for the increasing importance of the cruise phase. That is, lower solidity for higher cruise distances in order to meet the low cruise thrust requirement results in higher cruise efficiencies at the cost of climb and descent efficiency performance.

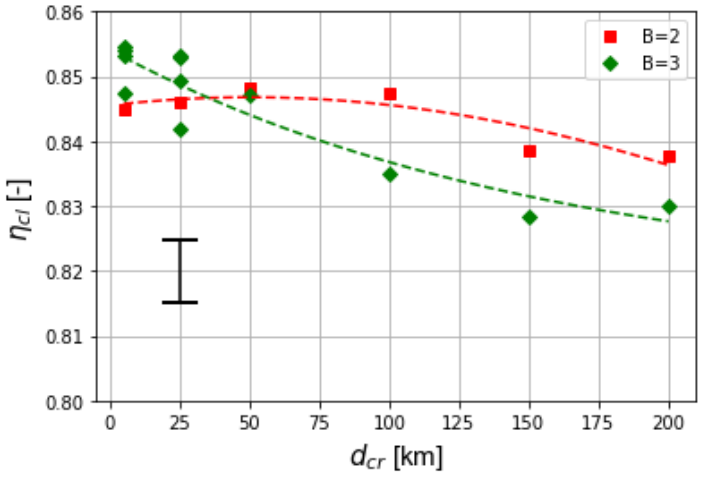

Figure 6.27: VPVR climb efficiency

6.2.2. CRUISE EFFICIENCY

In figure 6.28, the cruise efficiency is plotted for the CPVR case for both the two-bladed and three-bladed propellers. Initially, the cruise efficiency increases significantly but as the cruise distance gets very large compared to the climb and descent distances, the efficiency gain shows asymptotic behaviour. This is expected, since the changes in the ratio between the cruise distance and the distance covered during the whole mission become less as cruise distances increases.

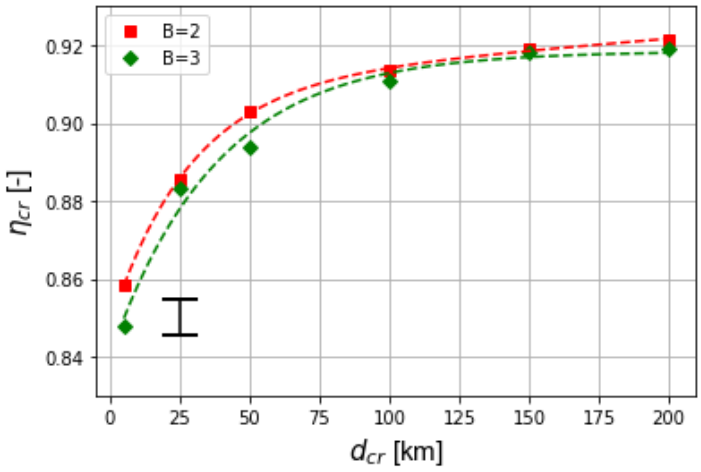

Figure 6.28: CPVR cruise efficiency

In figure 6.29, the cruise efficiency is plotted for the VPCR case for both the two-bladed and three-bladed propellers. In this case, the same asymptotic behaviour is present. However, it is interesting to note that the cruise efficiency of the two-bladed propeller is higher at low cruise distances than for the three-bladed propeller here. In this case, this is the result of the larger difference in the angles of attack the blade sections operate at for the two and three-bladed cases. During cruise, the majority of the blade sections operate at slightly negative angles of attack and for the two-bladed case, these angles of attack are more positive than for the three-bladed case in order to compensate for the loss in thrust due to the reduced blade solidity. The latter is due to a lower difference in chord distribution at low cruise distances between two and three blades and therefore a higher difference in solidity between two and three blades in case the blade pitch is variable

with respect to the constant pitch case. The more positive angles of attack seen for the two-bladed propeller during cruise increase its cruise efficiency with respect to the three-bladed propeller at low cruise distances.

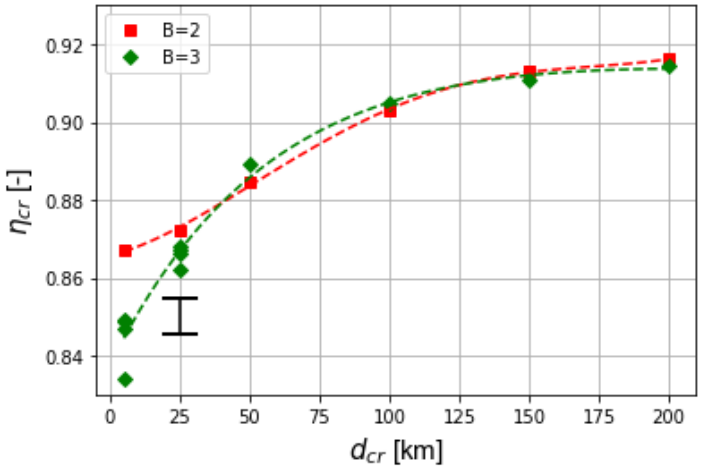

Figure 6.29: VPCR cruise efficiency

In figure 6.30, the cruise efficiency is plotted for the VPVR case for both the two-bladed and three-bladed propellers. The ability to vary the RPM in climb and cruise now as well leads to improved efficiencies over all cruise distances with respect to the efficiencies seen in figure 6.29, where the RPM in cruise was fixed to 2250 rev/min. A low RPM and large blade angles are selected for cruise in the VPVR case in order to increase the aerodynamic efficiency the airfoil sections operate at. For cruise, low angles of attack are seen; in fact, negative angles of attack are present over the majority of the blade span. Since a highly positive cambered airfoil does not perform efficiently at negative angles of attack, a low RPM value allows the angles of attack to be increased for the VPVR case. Since the cruise velocity is high, the blade angles are chosen to be high as well in order to maintain sufficient angles of attack along the blade span. Using this way of selecting the combination of pitch and RPM, higher cruise efficiencies can be achieved by the propeller.

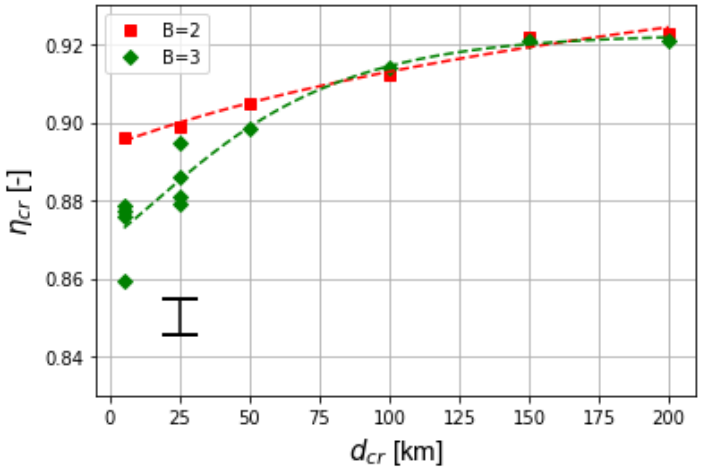

Figure 6.30: VPVR cruise efficiency

6.2.3. DESCENT EFFICIENCY

In figure 6.31, the descent efficiency is plotted against the cruise distance for the CPVR case for two and three blades. As expected, the descent efficiency decreases as the cruise distance increases and as the cruise distance gets larger, the difference in relative importance of the descent phase decreases as well and the descent efficiency shows an asymptotic behaviour. It is interesting to note that the three-bladed propeller has a larger descent efficiency for all cruise distances. The increase is likely a result from a larger propeller

solidity, leading to an increase in descent torque coefficient and as a result, this becomes the leading cause of a larger descent efficiency.

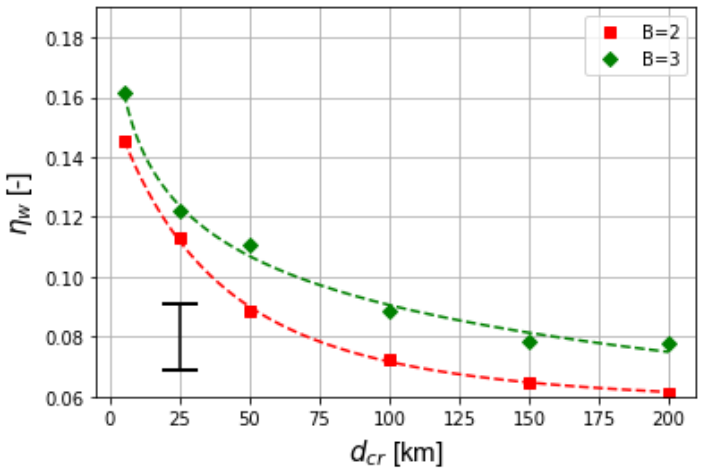

Figure 6.31: CPVR descent efficiency

In figure 6.32, the descent efficiency is plotted against the cruise distance for the VPCR case for two and three blades. The ability to vary the pitch significantly increases the descent efficiencies as can be observed from figure 6.32 as compared to figure 6.31. The blade pitch has a large influence on the angles of attack encountered along the blade span, and since the propeller operates at negative angles of attack during descent, this can be achieved by pitching the blades.

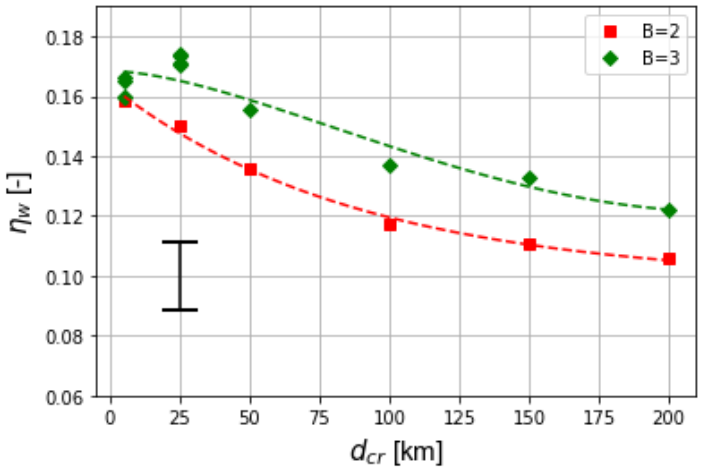

Figure 6.32: VPCR descent efficiency

In figure 6.33, the descent efficiency is plotted against the cruise distance for the VPVR case for two and three blades. Similar efficiencies are seen here as compared to the VPCR case as expected, since for the latter case, both the descent pitch and RPM were variable as well.

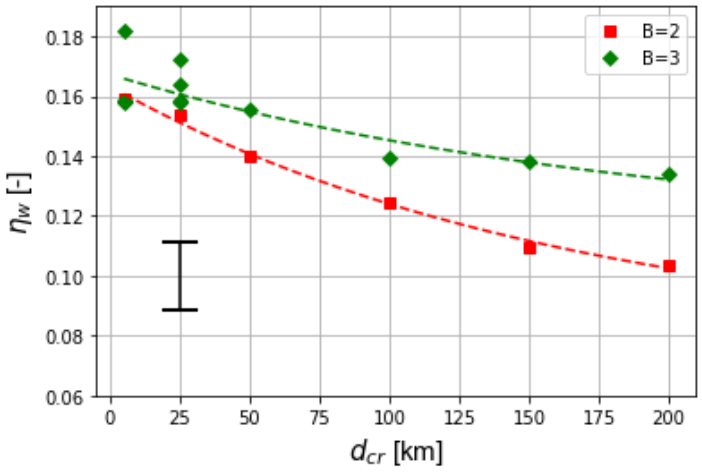

Figure 6.33: VPVR descent efficiency

6.3. PROPELLER ENERGY CONSUMPTION

In this section, results for the propeller energy consumption are presented for all optimisation cases. The influence of varying the propeller pitch and RPM on the total energy consumption, climb energy consumption and the fraction of energy recuperated over the whole mission is studied.

6.3.1. TOTAL ENERGY

In figure 6.34, the total propeller energy consumed during the mission is plotted against the cruise distance for all optimisation cases for two blades. Only the two-bladed case is shown here, since the relative difference when using three blades with respect to two blades cannot clearly be observed from the total energy plot. However, shortly this difference will be discussed using an alternative approach. The total energy consumed during the mission is mostly influenced by the cruise energy, since for most of the cruise distances considered, these distances are relatively large as compared to the climb and descent distances. Although the increase in cruise efficiency is not linear with cruise distance, its contribution to the calculation of the cruise energy is very small with respect to the contribution of the magnitude of the cruise distance and therefore, as expected, the total energy shows a linear behaviour with the cruise distance. At this point, it is interesting to compare the total energy consumption result for the multi-point optimisation in figure 6.34 to figure 5.28. It can be seen that the energy consumption values of the cruise propeller from the single-point optimisation results are very similar to the multi-point results for the total energy consumption for a 200 km cruise distance. In fact, as expected the single-point total energy consumption results are only slightly higher for all cases.

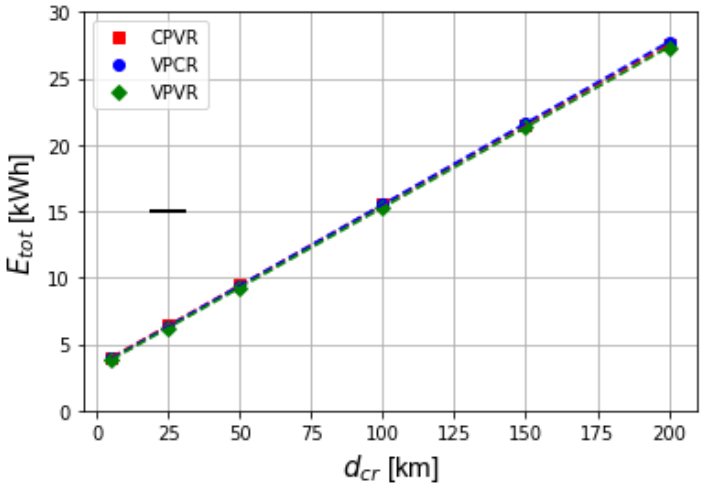

Figure 6.34: Total energy consumption for CPVR, VPCR and VPVR, B = 2

From figure 6.34, it appears that there are only very small differences in total energy consumption between the three optimisation cases. Since it is hard to visualise the differences in energy consumption between the various cases from the total energy plot, figures 6.35 and 6.36 are generated. Figure 6.35 shows the percentual difference in total energy consumption of the VPVR propeller with respect to the CPVR propeller as a function of the cruise distance. It can clearly be seen that the advantage of varying the pitch on the total energy consumption is highest at lower cruise distances. This is expected because of the higher relative importance of the three separate flight phases with respect to each other in terms of energy consumption or regeneration at lower cruise distances. Also, it can be concluded that the two-bladed VPVR propeller shows a higher decrease in total energy consumption with respect to the two-bladed CPVR propeller as compared to the three-bladed case, in particular as the cruise distance decreases. This behaviour is in line with the cruise efficiency plots in figures 6.28 and 6.30 for the CPVR and VPVR cases respectively. From these figures, it was observed that for two blades, the difference in cruise efficiency between the VPVR and CPVR cases is higher than for the three-bladed case, resulting in a lower relative cruise energy consumption for two blades. On the other hand, it was seen that the relative difference between the use of two or three blades between the VPVR and CPVR cases is less for the climb and descent efficiencies at lower cruise distances and therefore, the larger influence of the relative cruise efficiencies is the dominant factor leading to a reduced relative energy consumption for two blades with respect to three blades at lower cruise distances.

In figure 6.36, the percentual difference in total energy consumption of the VPVR propeller with respect to the VPCR propeller as a function of the cruise distance is plotted. Comparing figures 6.35 to 6.36, it is clear that the influence of varying only the blade pitch is higher with respect to total energy consumption at lower cruise distances as compared to the influence of varying only the RPM. However, at larger cruise distances (starting from about d_{cr} = 50 km), the influence of varying only the RPM during climb and cruise results in a larger decrease in total energy consumption as compared to the variable pitch case. This is most likely a result of the fact that for large cruise distances, the constant cruise RPM for the VPCR case is not an optimal value, while for the CPVR case the pitch setting will mostly be optimised for cruise for large cruise distances and unlike the VPCR case, in the CPVR case the possibility to vary the RPM still exists.

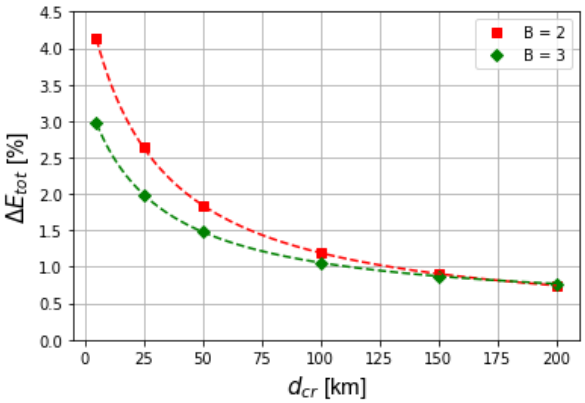

Figure 6.35: Percentage decrease in total energy for a VPVR propeller w.r.t. a CPVR propeller

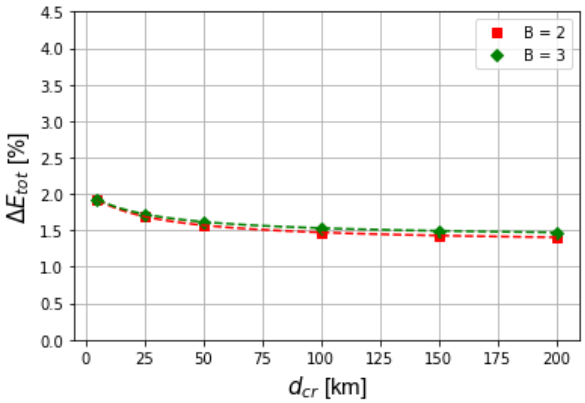

Figure 6.36: Percentage decrease in total energy for a VPVR propeller w.r.t. a VPCR propeller

6.3.2. CLIMB ENERGY

Since the climb phase is characterised by a relatively high energy consumption as compared to the remaining flight phases, it is interesting to investigate the influence of varying the propeller pitch and RPM on the energy consumption during climb as well. In figure 6.37, the percentual difference in the climb energy consumption of the VPVR propeller with respect to the CPVR propeller as a function of the cruise distance is plotted. It can be seen that for lower cruise distances (below approximately d_{cr} = 50 km), the VPVR propeller consumes less energy during climb as compared to the CPVR propeller while at cruise distances above approximately 50 km the CPVR propeller shows a decreased climb energy consumption with respect to the VPVR propeller. An explanation for this behaviour is the fact that for the CPVR case, the climb efficiency is relatively low at low cruise distances with respect to the VPVR case as can be seen from figures 6.25 and 6.27. Hence, the climb energy consumption for the CPVR case becomes relatively high with respect to the VPVR case. For larger cruise distances however, the climb efficiency of the CPVR propeller remains relatively high as compared

to the decrease in climb efficiency with the cruise distance for the VPVR case, resulting in a better climb energy performance for the CPVR propeller. The improvement in climb energy consumption of the CPVR case with respect to the VPVR case at higher cruise distances might sound counterintuitive since for the VPVR case, unlike for the CPVR case, the possibility to also vary the blade pitch in every flight phase is possible. However, as was seen before from figure 6.35, for the overall flight mission indeed a reduction of the total energy consumption of the VPVR case with respect to the CPVR case was seen. However, the blade geometries of the CPVR and VPVR case differ and this could possibly cause the improvement in climb performance of the CPVR case with respect to the VPVR case at higher cruise distances. The inability to vary the blade pitch for the CPVR case leads to higher blade radii when optimising over the complete flight mission for larger cruise distances, which could be beneficial for the climb performance with respect tot the VPVR case.

In figure 6.38, the percentual difference in the climb energy consumption of the VPVR propeller with respect to the VPCR propeller as a function of the cruise distance is shown. In this case, an increase in the difference between the climb energy consumption for the two cases can be seen as the cruise distance increases. This is largely a result of the fact that the climb efficiency for the VPCR case decreases rapidly with the cruise distance as compared to the VPVR case as was seen in figures 6.26 and 6.27.

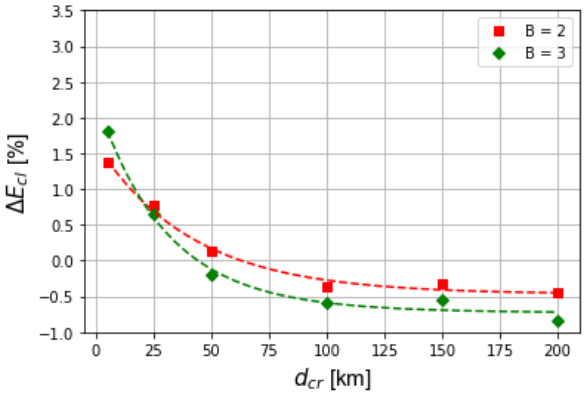

Figure 6.37: Percentage decrease in climb energy for a VPVR propeller w.r.t. a CPVR propeller

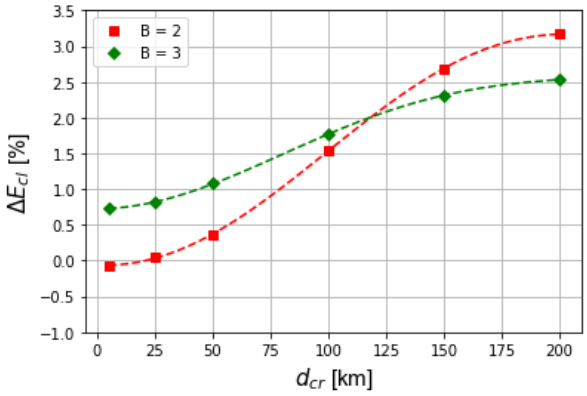

Figure 6.38: Percentage decrease in climb energy for a VPVR propeller w.r.t. a VPCR propeller

6.3.3. PERCENTAGE OF ENERGY RECUPERATED

In figures 6.39 and 6.40, the fraction of energy recuperated during the mission E_{rec} is plotted versus the cruise distance for all optimisation cases for two and three blades respectively. It is calculated using equation 6.2 as the ratio between the energy recuperated and the total energy consumed during the propulsive flight phases.

$$E_{rec} = \left(\frac{E_w}{E_{cl} + E_{cr}} \right) \cdot 100\% \tag{6.2}$$

A clear exponential decline of the fraction of energy recuperated is seen for all optimisation cases in figures 6.39 and 6.40. Both for two and three blades, the fraction of energy recuperated is highest for the VPVR case and lowest for the CPVR case. This can be explained by the fact that the ability to vary the propeller blade pitch during the mission is very beneficial for energy harvesting performance, as outlined before. In section 6.2, it was seen that for two blades, the climb and cruise efficiencies are generally higher than for three blades and that for three blades, the descent efficiencies are generally higher for all optimisation cases. This implies that the two-bladed propellers recuperate less energy, but also consume less energy during the propulsive flight phases with respect to the three-bladed propellers. Therefore, for the two-bladed propellers, both the numerator and denominator in equation 6.2 are decreased with respect to the three-bladed propellers. This explains the very similar behaviour seen in figures 6.39 and 6.40 for the fraction of energy recuperated for two and three blades respectively.

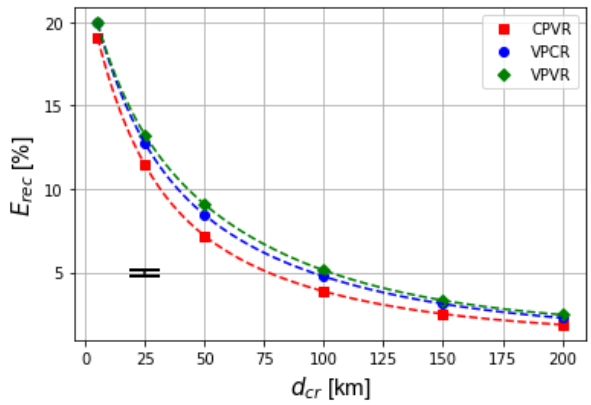

Figure 6.39: Fraction of energy recuperated for CPVR, VPCR and VPVR, B = 2

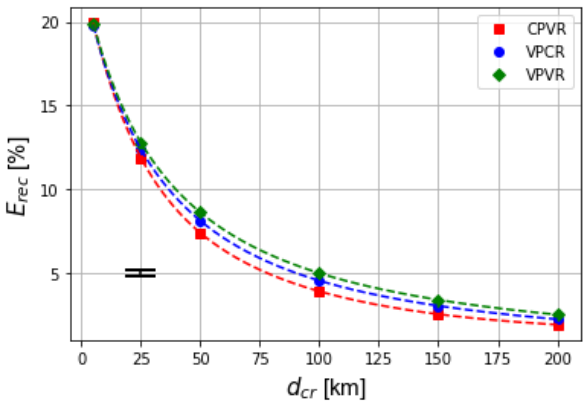

Figure 6.40: Fraction of energy recuperated for CPVR, VPCR and VPVR, B = 3

6.4. RATE OF DESCENT

In figures 6.41 and 6.42, the rate of descent as a function of cruise distance is plotted for all optimisation cases for two and three blades respectively. The rate of descent is closely related to the energy harvesting performance. A high rate of descent corresponds to a high descent efficiency and therefore, as expected, the rate of descent decreases as the cruise distance increases as can be seen in figures 6.41 and 6.42. Comparing figures 6.41 and 6.42 to figures 6.31 - 6.33, it can clearly be observed that indeed the rate of descent is closely related to the descent efficiency.

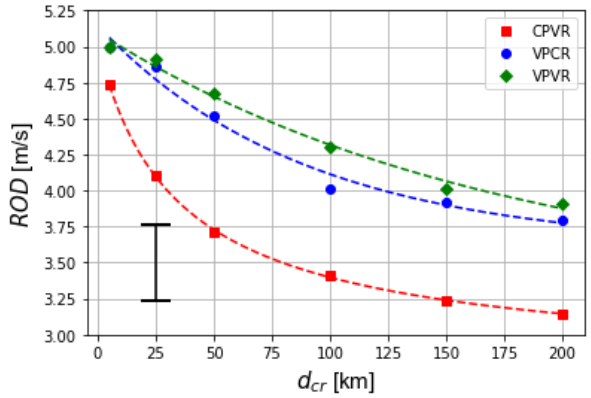

Figure 6.41: Rate of descent for CPVR, VPCR and VPVR, B = 2

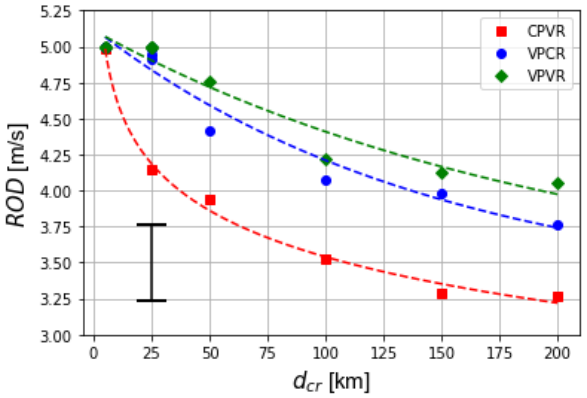

Figure 6.42: Rate of descent for CPVR, VPCR and VPVR, B = 3

6.5. EFFECT OF AIRFOIL CAMBER

In this section, the effect of airfoil camber on the propeller performance is studied. For all the optimisation results discussed in this report so far, only the NACA 4415 airfoil has been applied along the blade span. It is therefore interesting to investigate the influence of airfoil camber on the optimisation results. This investigation is performed for the VPVR case for two blades, since it is the most interesting case for future reference. Optimisation runs are performed for the NACA 0015 and NACA 2415 airfoils for flight missions with cruise distances of 5 km and 200 km in order to be able to assess the extent to which camber can influence the propulsive, energy harvesting and overall energy performance on these missions. For the mission where the cruise distance is 5 km, the descent phase represents a relatively large fraction of the total mission and therefore, the energy harvesting performance is relatively important here. On the other hand, the propulsive performance becomes relatively more important for the mission where the cruise distance is 200 km.

In figures 6.43 and 6.44, the total energy consumed and the percentage of energy recuperated by the propellers using the NACA 0015, NACA 2415 and NACA 4415 airfoils along the span are shown respectively for a cruise distance of d_{cr} = 5 km. As can be seen, the propeller using the NACA 0015 airfoil consumes the least amount of energy during the mission where the cruise distance is 5 km as compared to when using the NACA

2415 or the NACA 4415 airfoil. Having a very similar cruise performance as compared to the NACA 4415 propeller, the NACA 0015 airfoil recuperates more energy during the descent as compared to the NACA 2415 and NACA 4415 propellers as expected, due to the decrease in section efficiency when exposing positively cambered airfoils to negative angles of attack encountered during the descent.

Compared to the NACA 0015 and NACA 4415 airfoils, the propeller using the NACA 2415 airfoil results in the highest energy consumption throughout the mission with a cruise distance of 5 km. It consumes slightly more energy during climb and slightly less during cruise as compared to the propeller using the NACA 4415 airfoil, however, it recuperates less energy than the NACA 4415 airfoil and far less than the propeller using the NACA 0015 airfoil.

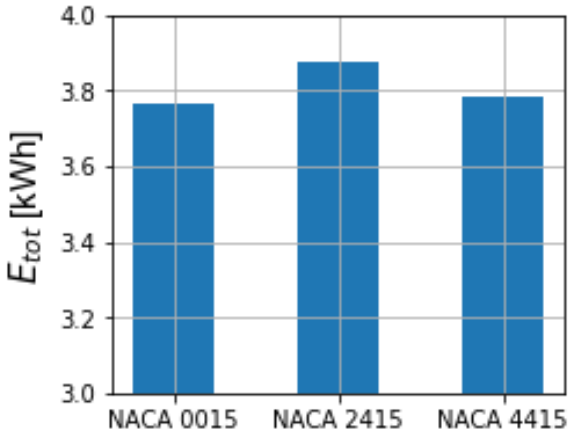

Figure 6.43: Total energy consumption for d_{cr} = 5km

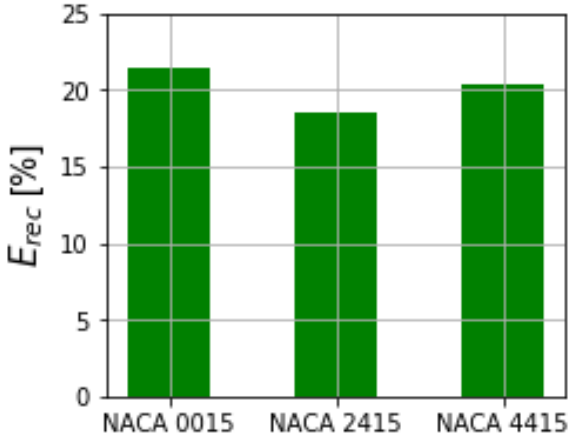

Figure 6.44: Fraction of energy recuperated for d_{cr} = 5km

In figures 6.45 and 6.46, the total energy consumed and the percentage of energy recuperated by the propellers using the NACA 0015, NACA 2415 and NACA 4415 airfoils along the span are shown respectively for a cruise distance of d_{cr} = 200 km. During this mission, the propeller using the NACA 0015 airfoil also consumes less energy over the whole mission than the propeller using the NACA 4415 airfoil. Although the propeller with the NACA 4415 airfoil consumes slightly less energy during cruise, the NACA 0015 propeller recuperates significantly more energy than the NACA 4415 propeller. The latter is the dominant factor for the difference in total energy consumption between the NACA 0015 and NACA 4415 propellers. As can also be seen from figure 6.45, the propeller using the NACA 2415 airfoil consumes the least amount of energy as compared to the propellers using the NACA 0015 or NACA 4415 airfoil. It recuperates less energy than in the NACA 0015 case, however it performs better during climb and cruise. Compared to the NACA 4415 airfoil case, the propeller using the NACA 2415 performs better in all flight phases and the contribution to the reduction in total energy consumption of the NACA 2415 propeller with respect to the NACA 4415 propeller is mainly a result of the relatively high amount of energy recuperated.

As became clear earlier, the main purpose of this project is to investigate the influence of the application of variable propeller pitch and RPM on the propeller energy consumption on a mission including energy harvesting and compare it to the performance using constant pitch. The choice of the propeller airfoil is not expected to cause significant differences in the relative performance between the variable and constant pitch cases. Therefore, although it can be concluded the NACA 4415 airfoil does not show the best energy performance as compared to the NACA 0015 and NACA 2415 airfoils for the considered mission cases, the earlier obtained results for the influence of variable pitch and RPM on the energy performance are still valuable for the purpose of this project.

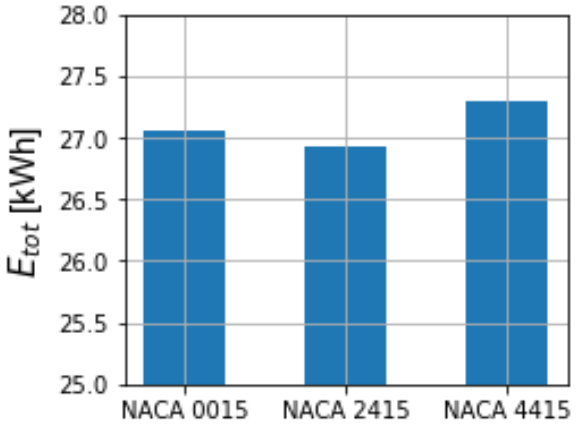

Figure 6.45: Total energy consumption for d_{cr} = 200km

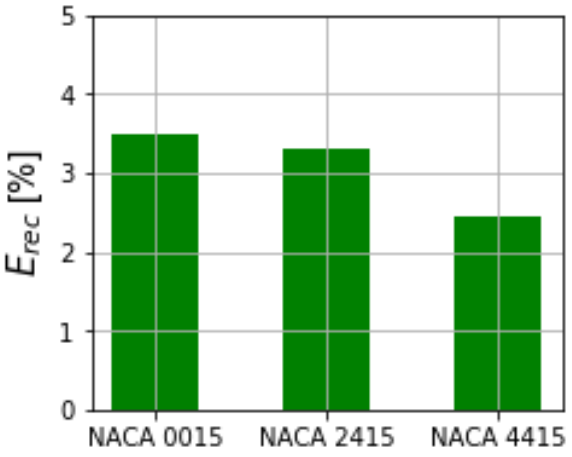

Figure 6.46: Fraction of energy recuperated for d_{cr} = 200km

As an example for the mission where d_{cr} = 200 km, the energy performance can be explained based on the observed blade loading shown in figures 6.47 - 6.50. In figures 6.47 and 6.49, the angle of attack distributions are plotted for the NACA 0015 and NACA 4415 propellers and in figures 6.48 and 6.50 show the corresponding L/D distributions. Observing the angles of attack for the NACA 0015 and NACA 4415 propellers, it is clear that the NACA 4415 propeller operates at relatively low angles of attack as compared to the NACA 0015 propeller since for the application of a cambered airfoil, smaller angles of attack along the span are capable of meeting the same overall propeller thrust requirement as compared to the use of symmetrical airfoils. Because of the high camber this results in a slight increase in overall L/D along the blade span for the NACA 4415 propeller as compared to the NACA 0015 propeller. However, the regenerative L/D performance is significantly better for the NACA 0015 propeller as compared to the NACA 4415 propeller as can be seen from figures 6.48 and 6.50. Figures 6.51 and 6.52 show the angle of attack and L/D distributions of the NACA 2415 propeller for a cruise distance of 200 km.

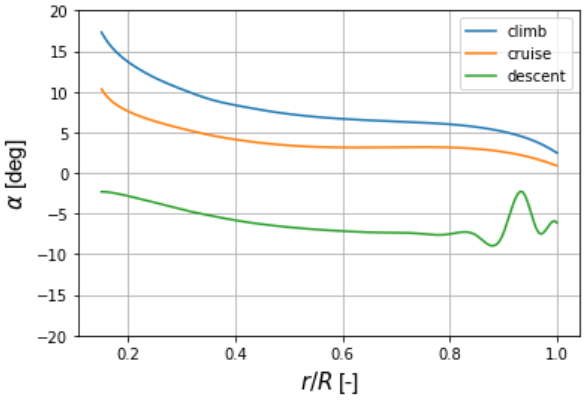

Figure 6.47: Angle of attack distribution for NACA 0015, d_{cr} = 200 km

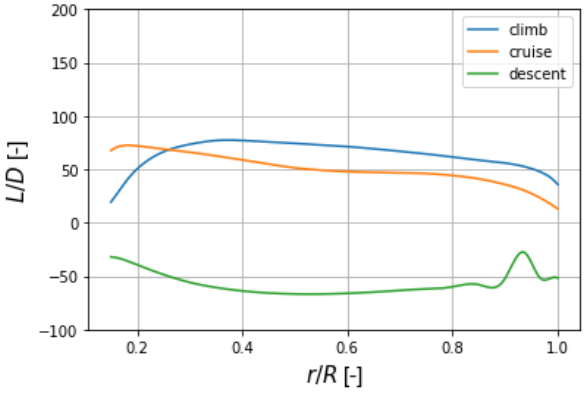

Figure 6.48: L/D distribution for NACA 0015, d_{cr} = 200 km

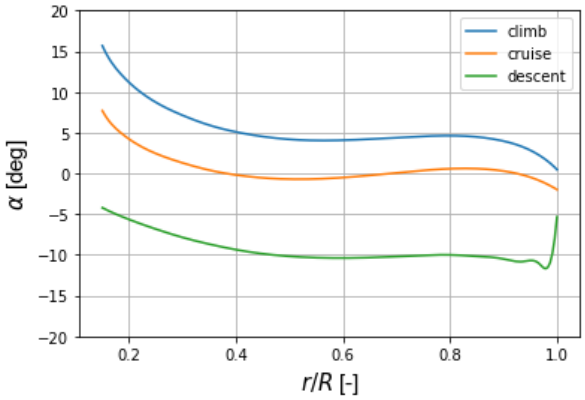

Figure 6.49: Angle of attack distribution for NACA 4415, d_{cr} = 200 km

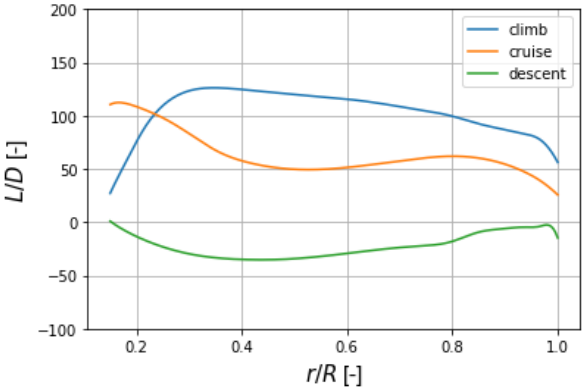

Figure 6.50: L/D distribution for NACA 4415, d_{cr} = 200 km

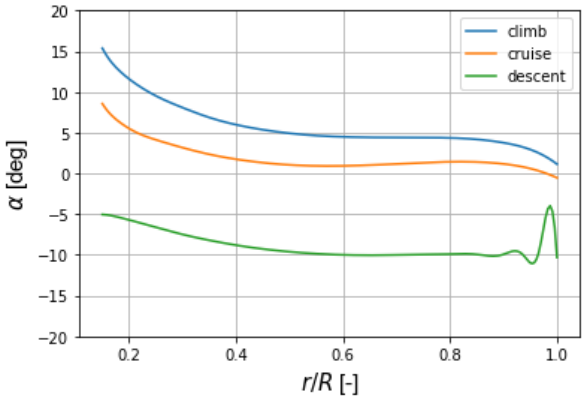

Figure 6.51: Angle of attack distribution for NACA 2415, d_{cr} = 200 km

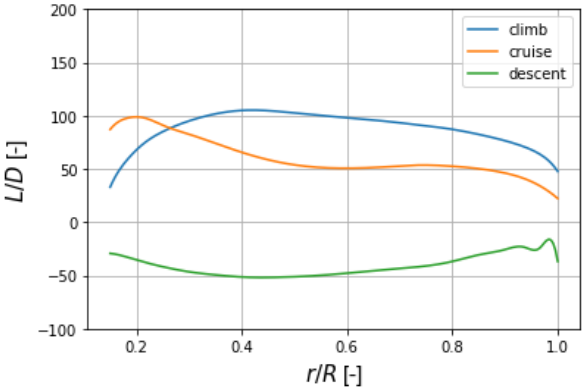

Figure 6.52: L/D distribution for NACA 2415, d_{cr} = 200 km

6.6. EFFECT OF AIRFOIL THICKNESS

In this section, the effect of the airfoil thickness is studied using the NACA 4412 airfoil for the propeller and comparing the results to the ones obtained earlier for the NACA 4415 airfoil. Again, the missions with cruise distances of 5 km and 200 km are considered. For the 5 km case, the NACA 4412 airfoil propeller performs worse during all flight phases as compared to the NACA 4415 airfoil propeller. Figures 6.53 and 6.54 show the total energy consumption and percentage of energy recuperated respectively for the NACA 4412 and NACA 4415 airfoils. Overall, the NACA 4412 case also performs worse over the whole mission than all other considered airfoils with a different camber.

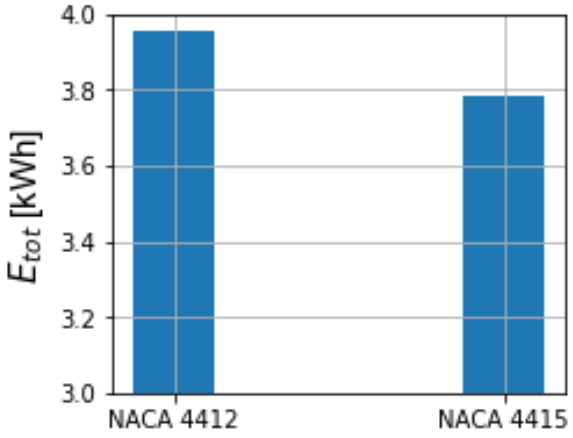

Figure 6.53: Total energy consumption for d_{cr} = 5km

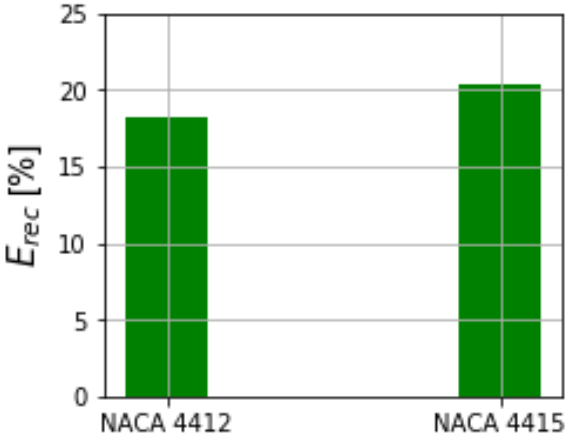

Figure 6.54: Fraction of energy recuperated for d_{cr} = 5km

For the 200 km cruise mission, the NACA 4412 airfoil again performs worse than all other airfoil cases. In figures 6.55 and 6.56, the total energy consumption and the fraction of energy recuperated are shown respectively for the NACA 4412 and NACA 4415 airfoils. Despite its slightly reduced energy consumption during climb and cruise with respect to the NACA 4415 case, less energy is harvested by the NACA 4412 propeller as can be concluded when comparing figures 6.57 and 6.58, showing the angle of attack and L/D distributions for the NACA 4412 propeller, to figures 6.49 and 6.50. A possible explanation for this is that the NACA 4412 airfoil is less efficient at the negative angles of attack encountered during the regenerative descent phase as compared to the NACA 4415 airfoil due to its combination of high camber and reduced thickness.

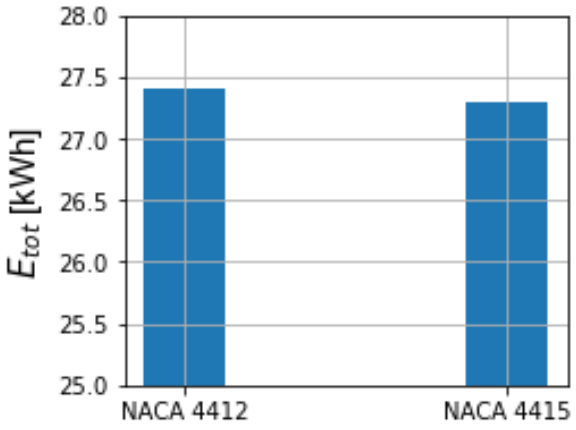

Figure 6.55: Total energy consumption for d_{cr} = 200km

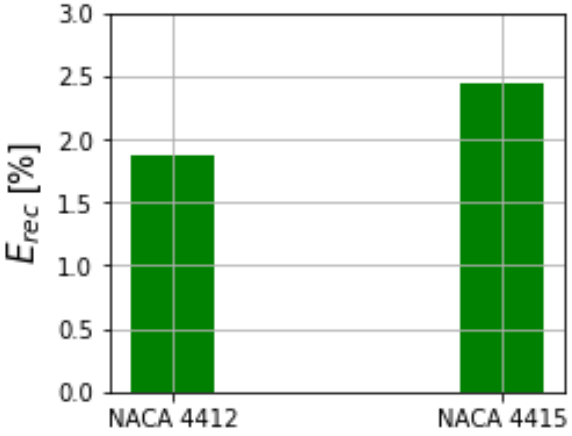

Figure 6.56: Fraction of energy recuperated for d_{cr} = 200km

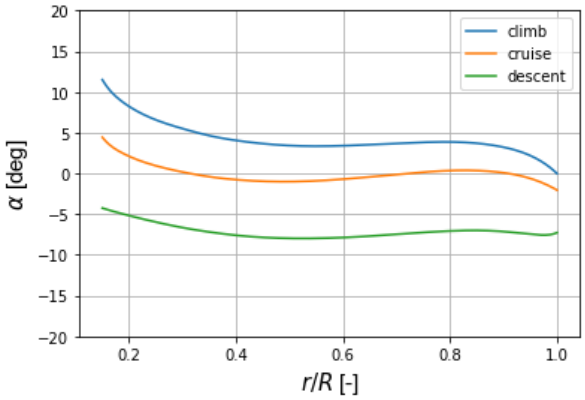

Figure 6.57: Angle of attack distribution for NACA 4412, d_{cr} = 200 km

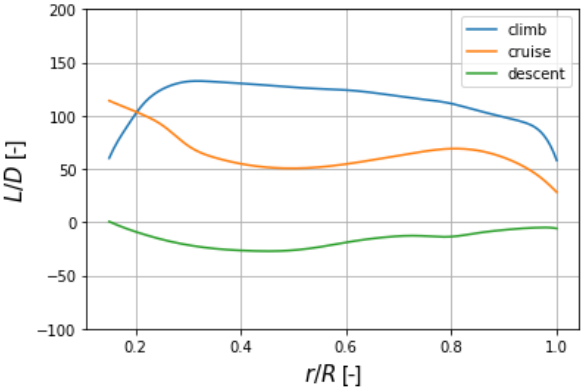

Figure 6.58: L/D distribution for NACA 4412, d_{cr} = 200 km

7

CONCLUSIONS AND RECOMMENDATIONS

In this chapter, conclusions and future recommendations are given as a result of the work performed in this project. Section 7.1 summarises the main conclusions that can be drawn and in section 7.2, recommendations for future research are proposed.

7.1. CONCLUSIONS

In this project, the influence of varying propeller blade pitch and RPM on the total energy consumption of an aircraft, including energy harvesting during the descent, is studied. As a first step, a propeller analysis model is selected that includes an accurate representation of the Goldstein circulation function under the assumption of helicoidal vortex sheet formation in order to evaluate the bound circulation on the propeller and subsequently the blade loading by iterating between the theoretical results and the experimental results for the blade loading at a given combination of local angle of attack, Reynolds number and Mach number. This propeller analysis algorithm is validated using a windtunnel experiment for energy harvesting on an existing propeller geometry. Using this geometry as an input to the propeller analysis model, the numerical and experimental results from the windtunnel are compared, using plots of the thrust and power coefficients versus the advance ratio, and analysed. It can be concluded that these results match very well, with the exception of some offset for the thrust coefficient at high advance ratios, which is most likely a result of the decreased accuracy of the XFOIL blade loading results at high angles of attack.

An optimisation algorithm needs to be selected in order to optimise the propeller blade shape and operational parameters for minimum energy consumption for three different cases regarding the variation of blade pitch and RPM. These are constant pitch, variable RPM (CPVR), variable pitch, constant RPM (VPCR) and variable pitch, variable RPM (VPVR). For VPCR, the RPM is still set as a variable during descent. As a first step, the exact optimisation problem needs to be formulated. A reference aircraft is selected for which the propeller optimisations are performed. Several design parameters of this aircraft are required for the design and optimisation of a propeller operating on it, allowing all the constraints and design variables, including their upper and lower bounds, for the optimisation problem to be defined. The propeller airfoil selection is performed using and XFOIL analysis where the L/D is plotted against the angle of attack for several combinations of Reynolds and Mach numbers as the blade sections are estimated to be exposed to during flight. Based on these results, it is expected that the NACA 4415 airfoil would perform best, since it appears to achieve the best compromise between propulsive and regenerative performance as compared to the airfoils with less camber and the symmetrical ones. After defining the objective function, constraints, design variables and their upper and lower bounds, the optimisation problem is defined to be the minimisation of the energy consumption over the whole aircraft mission subject to all the constraints and upper and lower bounds on the design variables. The type and nature of the optimisation problem leads to the selection of the differential evolution optimisation method to solve it, since genetic algorithms and in particular the differential evolution algorithm, are widely used for this type of problem. Gradient-based methods would not be suitable for the optimisation problem as a result of the large amount of design variables and the lack of capability to visualise the objective function, since it can not be written in closed-form.

The propeller optimisations are performed as a single-point and multi-point optimisation. The idea of the single-point optimisations is to optimise the propeller, both for two and three blades, only for one flight

condition at a time and optimising the resulting geometry for maximising its performance as much as possible for the remaining part of the mission. That is, optimising for the pitch and/or RPM in order to minimise total energy consumption. It can be concluded that the case where the pitch and the RPM are variable during the whole mission (VPVR) generally shows lower total energy values for the climb, cruise and descent propellers as compared to the CPVR and VPCR cases, although for some cases the differences are small. For the climb propellers, the total energy consumption is highest for the VPCR case and smallest for the VPVR case. With respect to the CPVR climb propeller case, the use of a two or three bladed VPVR climb propeller results in a decrease in total energy consumption in the order of 0.2 kWh. The largest differences in the total energy consumption between the CPVR, VPCR and VPVR cases are seen for the descent propellers. The total energy consumption of the descent VPVR propellers is in the order of 2.5 kWh less with respect to the VPCR case. Comparing the descent VPVR propellers to the descent CPVR propellers, larger differences are observed between the use of two and three blades. For two blades, the total energy consumption is about 2.0 kWh less for the VPVR case. However, for three blades, the VPVR propeller consumes about 0.2 kWh less. Furthermore, it is clear that the cruise propellers require a lower radius than the climb and descent propellers, most likely as a result of the low thrust constraint for this part of the flight mission. The radius of the two-bladed cruise propellers are about 10% lower than the radii of the climb and descent propellers for all optimisation cases, while this difference is about 18% for the three-bladed case. It can also be noted that the propellers optimised for descent have a higher solidity than the climb and cruise propellers for all optimisation cases.

During the multi-point optimisations, the propeller geometry and operation parameters are optimised, for two and three blades in all cases, for minimum energy consumption over the whole aircraft mission. For all optimisation cases, the optimisation runs are repeated for several cruise distances and the efficiencies and energy consumption is each flight phase are plotted against the cruise distance. Generally, it can be concluded that the cruise efficiency increases with cruise distance at the cost of climb and descent performance. Regarding the performance over the complete flight mission, the VPVR case consumes the least amount of energy for all cruise distances. Compared to the other cases, the percentage of total mission energy that can saved using a VPVR propeller with respect to the other two cases depends on the cruise distance. The largest percentage of total mission energy saved using the VPVR propeller with respect to the CPVR propeller is about 4.1% for a cruise distance of 5 km when using two blades and about 3.0% for three blades. This percentage is approximately 0.7% for a mission where the cruise distance is d_{cr} = 200 km, both for the two and three-bladed cases. It can be concluded that the performance of the two-bladed VPVR propeller with respect to the two-bladed CPVR propeller in terms of total energy consumption is better than for the three-bladed case for all considered cruise distances below d_{cr} = 150 km. Compared to the VPCR case, the VPVR propeller is capable of saving a larger percentage of the total energy than compared to the CPVR case for larger cruise distances, and a smaller percentage for shorter cruise distances. The largest percentage of total mission energy saved using the VPVR propeller with respect to the CPVR propeller is about 4.1% for a cruise distance of 5 km when using two blades and about 3.0% for three blades. This percentage reduces to approximately 0.7%, both for two and three blades, for a mission where the cruise distance is d_{cr}= 200 km. Compared to the VPCR case, the VPVR propeller saves a larger percentage of the total energy than compared to the CPVR case for larger cruise distances, and a smaller percentage for shorter cruise distances. These observations on the influence of the variation of the propeller pitch and RPM on the propeller energy consumption, within a mission including energy recuperation during the descent, answer the previously formulated main research objective of this thesis project. The percentage of energy saved during the climb phase for the VPVR propeller with respect to the CPVR propeller decreases with the cruise distance and becomes negative for cruise distances larger than approximately d_{cr}= 50 km. On the other hand, the climb energy saved using the VPVR propeller with respect to the VPCR propeller increases with the cruise distance and is mostly positive for all cruise distances. Regarding the fraction of energy recuperated, the VPVR propeller is capable of recuperating more energy at all cruise distances as compared to the CPVR and VPCR propellers. The rate of descent is also higher for the VPVR propeller as compared to the CPVR and VPCR propellers. Throughout the project, all propeller optimisations are performed using a constant NACA 4415 airfoil along the blade span. The effects of airfoil camber and thickness are briefly studied as well and it can be concluded that the airfoil selection based on minimum energy consumption highly depends on the cruise distance within the mission. For small cruise distances, the symmetrical NACA 0015 airfoil is most suitable while for long cruise distances, the NACA 2415 airfoil is the one that results in the least amount of total energy consumption. Regarding the effect of thickness, the application of the NACA 4415 airfoils results in reduced energy consumption as compared to the NACA 4412 airfoil in all the mission cases considered.

7.2. RECOMMENDATIONS FOR FUTURE RESEARCH

Considering the complete optimisation methodology developed throughout this project, several recommendations for future research are formulated. The list below indicates the proposed future work regarding the improvement of the performance of harvesting propellers on electric aircraft.

- Include design variables representing the airfoil geometry. This will add significantly more design variables to the optimisation problem, whereas in this project this is not applied due to the fact that this would require several XFOIL analysis procedures or additional panel method analysis runs during the optimisation run, which would significantly increase the optimisation run time. Using multiple airfoils along the blade span, designed specifically for a compromise between propulsive and energy harvesting performance, is expected to improve the overall energy performance of the propeller.
- Since a variable pitch propeller requires additional mechanisms to be incorporated within the aircraft, this adds complexity and extra overall weight to the aircraft. It is therefore required to investigate the feasibility of applying variable pitch for the purpose of improving energy performance in a mission including energy harvesting during descent; a feasibility analysis, related to the amount of energy that is saved at the cost of additional complexity and weight when applying a variable pitch and RPM propeller with respect to the current state of the art constant pitch propeller for energy harvesting application, needs to be performed.
- The propeller sweep is not considered in this project for the sake of simplifying the aerodynamic blade analysis, however, this would be an interesting additional design variable to consider for future research since the application of sweep could possibly further improve the propeller performance.
- The comparison of the performance of multiple global optimisation algorithms for the propeller optimisations would add valuable information to the results obtained using the differential evolution optimisation algorithm considered in this project, since their performance with respect to the differential evolution algorithm is unknown at this point

.

A

Chord Distributions for Single-Point Optimisations

A.1. Constant Pitch, Variable RPM

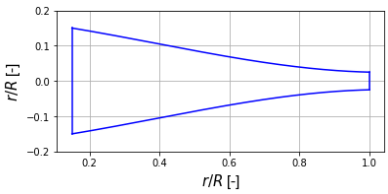

Figure A.1: CPVR Chord distribution for Climb Propeller, B = 2

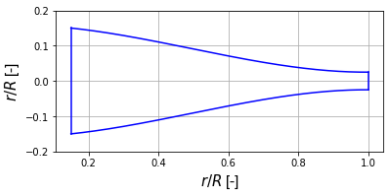

Figure A.2: CPVR Chord distribution for Cruise Propeller, B = 2

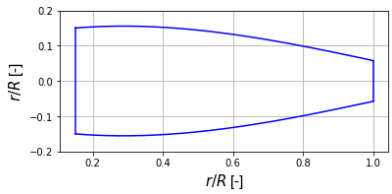

Figure A.3: CPVR Chord distribution for Descent Propeller, B = 2

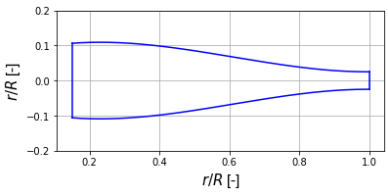

Figure A.4: CPVR Chord distribution for climb Propeller, B = 3

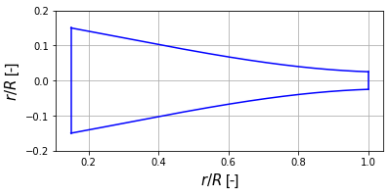

Figure A.5: CPVR Chord distribution for cruise Propeller, B = 3

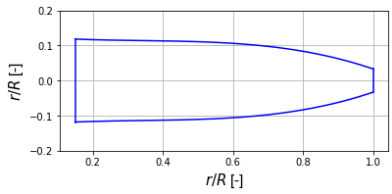

Figure A.6: CPVR Chord distribution for descent Propeller, B = 3

A.2. Variable Pitch, Constant RPM

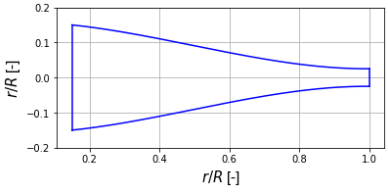

Figure A.7: VPCR Chord distribution for climb Propeller, B = 2

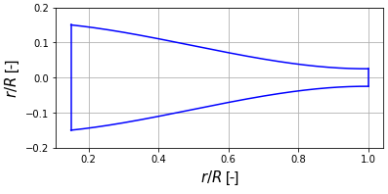

Figure A.8: VPCR Chord distribution for cruise Propeller, B = 2

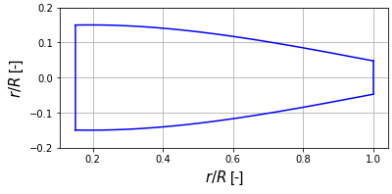

Figure A.9: VPCR Chord distribution for descent Propeller, B = 2

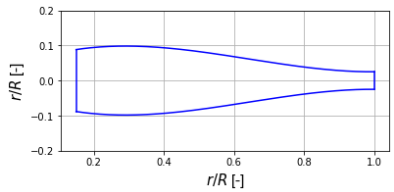

Figure A.10: VPCR Chord distribution for climb Propeller, B = 3

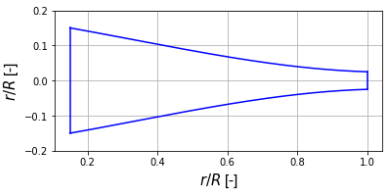

Figure A.11: VPCR Chord distribution for cruise Propeller, B = 3

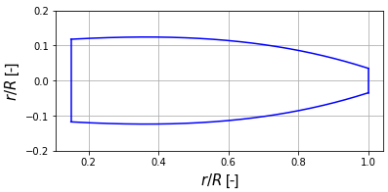

Figure A.12: VPCR Chord distribution for descent Propeller, B = 3

A.3. VARIABLE PITCH, VARIABLE RPM

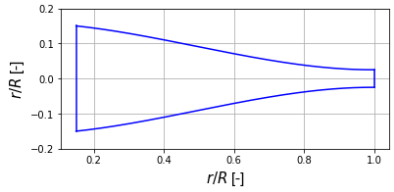

Figure A.13: VPVR Chord distribution for climb Propeller, B = 2

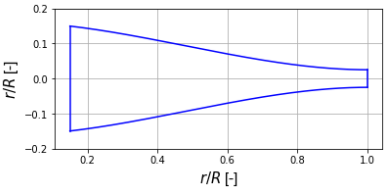

Figure A.14: VPVR Chord distribution for cruise Propeller, B = 2

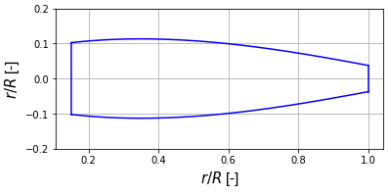

Figure A.15: VPVR Chord distribution for descent Propeller, B = 2

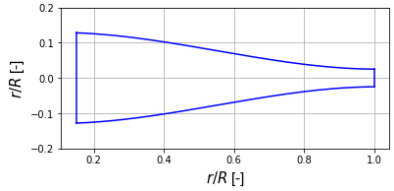

Figure A.16: VPVR Chord distribution for climb Propeller, B = 3

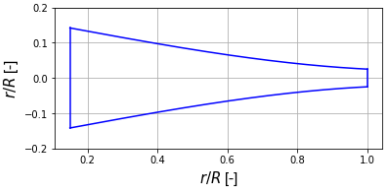

Figure A.17: VPVR Chord distribution for cruise Propeller, B = 3

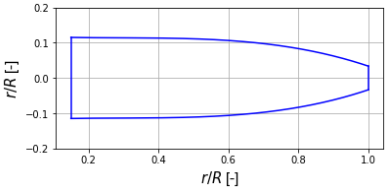

Figure A.18: VPVR Chord distribution for descent Propeller, B = 3

B

Single-Point Optimisation Results

Table B.1: Single-Point propeller optimisation results for climb

	CPVR		VPCR		VPVR	
Climb Propeller Results	2 blades	3 blades	2 blades	3 blades	2 blades	3 blades
Propeller radius [m]	0.9	0.9	0.9	0.88	0.9	0.9
Propeller RPM in climb [-]	2284	2185	2250	2250	2263	1910
Propeller RPM in cruise [-]	1909	1909	2250	2250	1909	1909
Propeller RPM in descent [-]	954	961	1250	1398	1244	1194
Descent velocity [m/s]	36.0	36.0	36.0	36.0	36.0	36.0
Rate of descent [m/s]	3.47	4.19	4.41	5.0	4.21	4.93
Climb efficiency [-]	0.851	0.85	0.851	0.848	0.851	0.856
Cruise efficiency [-]	0.909	0.881	0.879	0.847	0.909	0.881
Descent efficiency [-]	0.074	0.112	0.119	0.158	0.110	0.147
Climb energy [kWh]	4.103	4.105	4.104	4.116	4.102	4.08
Cruise energy [kWh]	24.24	25.037	25.047	26.043	24.193	25.024
Energy recuperated [kWh]	0.642	0.809	0.819	0.923	0.794	0.902
Fraction of energy recuperated [%]	2.32	2.86	2.89	3.16	2.89	3.2

Table B.2: Single-Point propeller optimisation results for cruise

	CPVR		VPCR		VPVR	
Cruise Propeller Results	2 blades	3 blades	2 blades	3 blades	2 blades	3 blades
Propeller radius [m]	0.83	0.75	0.77	0.7	0.78	0.71
Propeller RPM in climb [-]	2387	2387	2250	2250	2387	2387
Propeller RPM in cruise [-]	1909	1909	2250	2250	1909	1910
Propeller RPM in descent [-]	954	954	1432	1432	1203	1390
Descent velocity [m/s]	36.0	36.0	36.0	36.0	36.0	34.42
Rate of descent [m/s]	3.0	3.03	3.57	3.55	3.28	3.41
Climb efficiency [-]	0.835	0.827	0.783	0.782	0.811	0.804
Cruise efficiency [-]	0.925	0.923	0.92	0.919	0.93	0.928
Descent efficiency [-]	0.054	0.063	0.095	0.108	0.065	0.059
Climb energy [kWh]	4.182	4.222	4.457	4.464	4.302	4.339
Cruise energy [kWh]	23.796	23.829	23.918	23.942	23.665	23.717
Energy recuperated [kWh]	0.46	0.441	0.594	0.565	0.445	0.287
Fraction of energy recuperated [%]	1.67	1.6	2.14	2.03	1.62	1.03

Table B.3: Single-Point propeller optimisation results for descent

Descent Propeller Results	**CPVR**		**VPCR**		**VPVR**	
	2 blades	3 blades	2 blades	3 blades	2 blades	3 blades
Propeller radius [m]	0.9	0.9	0.9	0.9	0.9	0.9
Propeller RPM in climb [-]	2387	2123	2250	2250	2200	1909
Propeller RPM in cruise [-]	2178	1944	2250	2250	1909	1909
Propeller RPM in descent [-]	1119	1036	1196	1012	1254	1035
Descent velocity [m/s]	36.0	36.0	36.0	36.0	36.0	36.0
Rate of descent [m/s]	5.0	5.0	5.0	5.0	5.0	5.0
Climb efficiency [-]	0.814	0.828	0.824	0.816	0.832	0.835
Cruise efficiency [-]	0.809	0.826	0.813	0.748	0.874	0.831
Descent efficiency [-]	0.163	0.164	0.163	0.164	0.161	0.164
Climb energy [kWh]	4.291	4.216	4.239	4.277	4.195	4.182
Cruise energy [kWh]	27.19	26.65	27.046	29.394	25.235	26.465
Energy recuperated [kWh]	0.985	0.996	0.986	0.996	0.973	0.996
Fraction of energy recuperated [%]	3.23	3.33	3.25	3.05	3.42	3.36

BIBLIOGRAPHY

[1] D. Erzen, M. Andrejasic, and T. Kosel, *An optimal propeller design for in-flight power recuperation on an electric aircraft,* in *2018 Aviation Technology, Integration, and Operations Conference* (2018) p. 3206.

[2] J. P. Barnes, *Flight without fuel–regenerative soaring feasibility study*, Tech. Rep. (SAE Technical Paper, 2006).

[3] J. P. Barnes, *Regenerative electric flight synergy and integration of dual role machines,* in *53rd AIAA Aerospace Sciences Meeting* (2015) p. 1302.

[4] Q. R. Wald, *The aerodynamics of propellers,* Progress in Aerospace Sciences **42**, 85 (2006).

[5] C. Epstein, *Pipistrel Shows Electric Aircraft Options at Oshkosh,* https://www.ainonline.com/aviation-news/general-aviation/2018-07-23/pipistrel-shows-electric-aircraft-options-oshkosh (2018).

[6] H. Glauert, *The elements of aerofoil and airscrew theory* (Cambridge University Press, 1983).

[7] P. MacCready, *Regenerative battery-augmented soaring,* Technical Soaring **23**, 28 (1999).

[8] W. J. M. Rankine, *On the mechanical principles of the action of propellers,* Transactions of the Institution of Naval Architects **6** (1865).

[9] R. E. Froude, Trans. Inst. Naval Architects **30**, 390 (1889).

[10] Q. Wald, *The wright brothers propeller theory and design,* in *37th Joint Propulsion Conference and Exhibit* (2001) p. 3386.

[11] A. Betz, *Schraubenpropeller mit geringstem energieverlust,* Gottinger Nachrichten , 193 (1919).

[12] S. Goldstein, *On the vortex theory of screw propellers,* Proceedings of the Royal Society of London. Series A, Containing Papers of a Mathematical and Physical Character **123**, 440 (1929).

[13] T. Theodorsen, *Theory of propellers* (McGraw-Hill Book Company, 1948).

[14] J. Thauvin, G. Barraud, X. Roboam, B. Sareni, M. Budinger, and D. Leray, *Hybrid propulsion for regional aircraft: A comparative analysis based on energy efficiency,* in *2016 International Conference on Electrical Systems for Aircraft, Railway, Ship Propulsion and Road Vehicles & International Transportation Electrification Conference (ESARS-ITEC)* (IEEE, 2016) pp. 1–6.

[15] J. Olsen and J. R. Page, *Hybrid powertrain for light aircraft,* International Journal of Sustainable Aviation 15 **1**, 85 (2014).

[16] J. P. Barnes, *Principles of high-efficiency electric flight,* in *52nd AIAA/SAE/ASEE Joint Propulsion Conference* (2016) p. 4711.

[17] E. L. Houghton and P. W. Carpenter, *Aerodynamics for engineering students* (Elsevier, 2003).

[18] Pipistrel, *Aircraft information pipistrel alpha electro,* https://www.pipistrel-usa.com/alpha-electro/#manuals (2018).

[19] M. Niţă and D. Scholz, *Estimating the oswald factor from basic aircraft geometrical parameters* (Deutsche Gesellschaft für Luft-und Raumfahrt-Lilienthal-Oberth eV, 2012).

[20] J. P. Barnes, *Regenerative electric flight synergy and integration of dual role machines,* in *53rd AIAA Aerospace Sciences Meeting* (2015) p. 1302.

[21] Pipistrel, *Pilot's operating handbook,* https://www.pipistrel-usa.com/alpha-electro/#manuals (2018).

[22] J. Dorfling and K. Rokhsaz, *Integration of airfoil stall and compressibility models into a propeller blade element model,* Journal of Aerospace Engineering **29**, 04016014 (2016).

[23] O. Gur and A. Rosen, *Optimization of propeller based propulsion system,* Journal of Aircraft **46**, 95 (2009).

[24] M. Drela and H. Youngren, *Xfoil 6.94 user guide,* (2001).

[25] F. Taverna, *Advanced airfoil design for general aviation propellers,* Journal of Aircraft **21**, 649 (1984).

[26] B. D. Rutkay, *A process for the design and manufacture of propellers for small unmanned aerial vehicles,* Ph.D. thesis, Carleton University (2014).

[27] S. Gudmundsson, *General aviation aircraft design: Applied Methods and Procedures* (Butterworth-Heinemann, 2013).

[28] S. S. Rao, *Engineering optimization: theory and practice* (John Wiley & Sons, 2019).

[29] I. Sadrehaghighi, *Aerodynamic design & optimization,* ResearchGate: Berlin, Germany (2019).

[30] J. Dorfling and K. Rokhsaz, *Constrained and unconstrained propeller blade optimization,* in *52nd Aerospace Sciences Meeting* (2014) p. 0563.

[31] S. M. Islam, S. Das, S. Ghosh, S. Roy, and P. N. Suganthan, *An adaptive differential evolution algorithm with novel mutation and crossover strategies for global numerical optimization,* IEEE Transactions on Systems, Man, and Cybernetics, Part B (Cybernetics) **42**, 482 (2011).

[32] G. Jeyakumar and C. S. Velayutham, *A comparative performance analysis of differential evolution and dynamic differential evolution variants,* in *2009 World Congress on Nature & Biologically Inspired Computing (NaBIC)* (IEEE, 2009) pp. 463–468.

[33] L. Wang and L.-p. Li, *An effective differential evolution with level comparison for constrained engineering design,* Structural and Multidisciplinary Optimization **41**, 947 (2010).

[34] J. Lampinen, *A constraint handling approach for the differential evolution algorithm,* in *Proceedings of the 2002 Congress on Evolutionary Computation. CEC'02 (Cat. No. 02TH8600)*, Vol. 2 (IEEE, 2002) pp. 1468–1473.

[35] F. Hitchens, *Propeller aerodynamics: the history, aerodynamics & operation of aircraft propellers* (Andrews UK Limited, 2015).